
Electronic Theses and Dissertations, 2004-2019

2011

Density Functional Theory Study Of Molecules And Crystals Containing D And F Metals

Shruba Gangopadhyay
University of Central Florida

 Part of the [Chemistry Commons](#)

Find similar works at: <https://stars.library.ucf.edu/etd>

University of Central Florida Libraries <http://library.ucf.edu>

This Doctoral Dissertation (Open Access) is brought to you for free and open access by STARS. It has been accepted for inclusion in Electronic Theses and Dissertations, 2004-2019 by an authorized administrator of STARS. For more information, please contact STARS@ucf.edu.

STARS Citation

Gangopadhyay, Shruba, "Density Functional Theory Study Of Molecules And Crystals Containing D And F Metals" (2011). *Electronic Theses and Dissertations, 2004-2019*. 2037.

<https://stars.library.ucf.edu/etd/2037>

DENSITY FUNCTIONAL THEORY STUDY OF MOLECULES AND CRYSTALS
CONTAINING *d* AND *f* METALS

by

SHRUBA GANGOPADHYAY

M.S. Case Western Reserve University, U.S.A. 2005

A dissertation submitted in partial fulfillment of the requirements
for the degree of Doctor of Philosophy
in the Department of Chemistry
in the College of Sciences
at the University of Central Florida
Orlando, Florida

Spring Term

2011

Major Professor: Artëm E. Masunov

© 2010 Shruba Gangopadhyay

ABSTRACT

Density Functional Theory (DFT) method is applied to study the crystal structure of transition metal and lanthanide oxides, as well as molecular magnetic complexes. DFT is a widely popular computational approach because it recasts a many-body problem of interacting electrons into an equivalent problem of non-interacting electrons, greatly reducing computational cost. We show that for certain structural properties like phase stability, lattice parameter and oxygen migration energetics pure DFT can give good agreement with experiments. But moving to more sensitive properties like spin state energetic certain modifications of standard DFT are needed.

First we investigated mixed ionic-electronic conducting perovskite type oxides with a general formula ABO_3 (where A =Ba, Sr, Ca and B = Co, Fe, Mn). These oxides often have high mobility of the oxygen vacancies and exhibit strong ionic conductivity. They are key materials that find use in several energy related applications, including solid oxide fuel cell (SOFC), sensors, oxygen separation membranes, and catalysts. Different cations and oxygen vacancies ordering are examined using plane wave pseudopotential density functional theory. We find that cations are completely disordered, whereas oxygen vacancies exhibit a strong trend for aggregation in L-shaped trimer and square tetramer structure. On the basis of our results, we suggest a new explanation for BSCF phase stability. Instead of linear vacancy ordering, which must take place before the phase transition into brownmillerite structure, the oxygen vacancies in BSCF prefer to form the finite clusters and preserve the disordered cubic structure. This structural feature could be found only in the first-principles simulations and cannot be explained by the effect of the ionic radii alone. In order to understand vacancy clustering and phase

stability in oxygen-deficient barium strontium cobalt iron oxide (BSCF), we predict stability and activation energies for oxygen vacancy migration. Using symmetry constrained search and Nudged Elastic Band method, we characterize the transition states for an oxygen anion moving into a nearby oxygen vacancy site that is surrounded by different cations and find the activation energies to vary in the range 30-50 kJ/mol in good agreement with experimental data.

Next we study spin alignments of single molecule magnets (SMM). SMMs are a class of polynuclear transition metal complexes, which characterized by a large spin ground state and considerable negative anisotropy. These properties lead to a barrier for the reversal of magnetization. For these reasons SMM are expected to be promising materials for molecular spintronics and quantum computing applications. To design SMM for quantum computation, we need to accurately predict their magnetic properties. The most important property is, Heisenberg exchange coupling constant (J). This constant appears in model Heisenberg Hamiltonian that can be written in general form as

$$H = -\sum J_{ij} S_i \cdot S_j$$

here J_{ij} represents the coupling between the two magnetic centers i and j with the spin states S_i and S_j . The positive J values indicate the ferromagnetic ground state and the negative ones indicate the antiferromagnetic ground state. We found pure DFT is not accurate enough to predict J values. We employ density functionals with a Hubbard U term that helps to counteract the unphysical delocalization of electrons due to errors in pure exchange-correlation functionals. Unlike most previous DFT+U studies, we calibrate U parameters for both metal and ligand atoms using five binuclear manganese complexes as the benchmarks. We note delocalization of the spin density onto acetate ligands due to π -back bonding, inverting spin-polarization of the

acetate oxygen atoms relative to that predicted from superexchange mechanism. This inversion may affect performance of the models assuming strict localization of the spins on magnetic centers for the complexes with bridging acetate ligands. Next, we apply DFT+U methodology for $\text{Mn}_{12}(\text{mda})$ and $\text{Mn}_{12}(\text{ada})$ complexes to calculate all six nearest neighbor J_{ij} value. Our result shows both qualitative and quantitative agreement with experiments unlike other DFT studies. Using the optimized geometry of the ground spin state instead of less accurate experimental geometry was found to be crucial for this good agreement. The protocol tested in this study can be applied for the rational design of single-molecule magnets for molecular spintronics and quantum computing applications.

Finally we apply hybrid DFT methodology to calculate geometrical parameters for cerium oxides. We review the experimental and computational studies on the cerium oxide nanoparticles, as well as stoichiometric phases of bulk ceria. Electroneutral and nonpolar pentalayers are identified as building blocks of type A sesquioxide structure. The idealized structure of the nanoparticles is described as dioxide covered by a single pentalayer of sesquioxide, which explains the exceptional stability of subsurface vacancies in nanoceria. The density functional theory (DFT) predictions of the lattice parameters and bulk moduli for the Ce(IV) and Ce(III) oxides at the hybrid DFT level are also presented. The calculated values for both compounds agree with experiment and allow to predict changes in the lattice parameter with decreasing size of the nanoparticles. The results validate hybrid DFT as a promising method for future study the structure of oxygen vacancies and catalytic properties of ceria nanoparticles.

To Almighty

ACKNOWLEDGMENTS

First, my greatest regards to the Almighty for bestowing upon me the courage to face the complexities of life and complete my dissertation successfully. I am dedicating my dissertation to the super power who teaches us to do duties without getting attached to the results.

I owe my gratitude to all those people who have made this dissertation possible and because of whom my graduate experience has been one that I will cherish forever.

My sincere and the deepest gratitude goes to my loving parents for their love and sacrifice. I especially thank my father for being my role model, he teaches me never to give up until reaching the destination. His constant encouragement for instilling the importance of hard work make this day possible.

I would like to express my cordial thanks to my dissertation advisor Professor Artem E. Masunov for his encouragement, thoughtful guidance, and critical comments. I am thankful to him for giving me the opportunity to work with diverse research projects, which helped me enormously gain confidence in my research work.

My next thank goes to Department of Chemistry for accepting my application for doctoral study and NanoScience Technology Center for proving me collaborative and wonderful research environment.

I am grateful to my dissertation committee members Professor Ratan Guha, Professor Andre Gesquiere, Professor Steven Kuebler, Professor Robert Igarashi for their constructive reviews, a special thanks to Professor Enrique del Barco for his encouragement to move my future research direction towards magnetism. I am sincerely thanking all my past and present group members for providing me friendly and convivial work environments.

I express my sincere thanks to my collaborators, Professor Nina Orlovskaya, Professor Ratan Guha, Professor Jayanta Kapat, Professor Ahmet Sleiti for solid oxide fuel cell project, for my molecular magnet project Professor Michael Leuenberger, Professor George Christou, Professor Enrique del Barco, Professor Eduardo Mucciolo. for cerium oxide project Professor Sudipta Seal, Dr. Konstantin Kudin. Not to forget the student members in the collaboration team, Arpita, Deanna, Ajay, Jaruwan, Simranjeet, Eliza, Richard, Oleg.

All the computational work won't be possible without NERSC and I2lab support team. My deepest thanks to Zhengji Zhao, Steve Dick, and Sampyo Hong for compilation help in Quantum ESPRESSO. I would like to thank Professor Sergey Stolbov for first introducing me with Quantum ESPRESSO. Comments from unknown referees, helps us to make our papers more meaningful, all the Quantum ESPRESSO forum members for their insightful discussions and the research awards for appreciating our efforts. It is too short place to name but I don't want to skip mentioning the researchers for their constructive criticism during my conference presentations.

Not to forget all office staff members in NanoScience Technology Center and Department of Chemistry. I would like to mention my teaching lab instructor Dr. Donavon Dixon for his special support, especially during conference travel time.

To my teachers, Dr Rathin Mitra, Suman Bhattacharya, Basana Bagchi, Professor Rajkumar Roychoudhury, Professor Swapan Mukherjee, Professor Asoke Prasun Chattopadhyay, Ms Lily De. Dr Arunava Sen and Professor Fred L. Urbach for making me interested in inorganic chemistry.

I want to dedicate separate place to some of my very dear friends. I can refer them as AAA, they are Anindarupa, Arunima, Angel. I convey my sincere thanks to them for supporting me in the worst days of life.

Another earnest thanks to my wonderful roommates, Jyoti and Simranjeet for providing wonderful ambience and support me in every possible ways. Without them I don't think I will be able to complete my degree.

Thanks to my brother Samidh Gangopadhyay, my cousin Ranita, and sweet little cousin Anannya (Jaya), my aunt Krishna Gangopadhyay for their love and support.

I would like to thank Tapasda and Dr. Jes Seller for his constant support and motivation for doing good work. I should not forget another person, Souvik for making me smile in my gloomiest days.

Some of my closest people not in this earth I am missing them today, Ms. Rama Majumdar, Maternal Grandmother Bijaya Devi, Paternal Grandaunt Shantilata Chattopadhyay, Granduncle Shailashekhar Chattopadhyay. A special gratitude to my Granduncle Dr. Rabindranarayan Gangopadhyay, without mentioning him this acknowledgment will be incomplete. He was legendary example in our family for academic excellence, and my inspiration for my higher education.

Now it's time to write about my friends in Orlando, who made my doctoral days enjoyable, Anindarupa, Debasis, Tanusri, Surajit, Satarupa, Soumitra, Ranita, Sourangsu, Sriparna, Indra, Jaya, Subhash, Tandra, Subhajit, Atreye, Sudip, Chaitali, Pansy, Annu, Satyender, Mona, Saptarshi, Tanmay and many others. I acknowledge all of them for wonderful get-togethers. Thanks to my school and college friends Jayeeta, Saswati, Tuhin, Ayesha, Mithun,

Siddhartha, my net friends Malini, Anuradha, Soiti. Last but not the least members of feluscinations for supplying fuels for magajastra (intellectual acumen) want to especially mention Soumitda, Soumendu, Jedida, and many others.

I certainly overlooked the help and encouragement of many others, please forgive me for unconditional oversight. On finale many many thanks to Google, Wikipedia and YouTube.

TABLE OF CONTENTS

| | |
|--|--------------|
| <u>LIST OF FIGURES</u> | <u>xiv</u> |
| <u>LIST OF TABLES</u> | <u>xviii</u> |
| <u>CHAPTER 1 INTRODUCTION</u> | <u>1</u> |
| <u>1.1 Transition metals and Crystal field splitting in octahedral field.....</u> | <u>11</u> |
| <u>1.2 Computational studies on oxygen migration of perovskites.....</u> | <u>13</u> |
| <u>1.3 Molecular magnet and antiferromagnetic wheel and application in spintronics</u> | <u>15</u> |
| <u>1.4 Cerium oxides and its property</u> | <u>18</u> |
| <u>CHAPTER 2 THEORY</u> | <u>25</u> |
| <u>2.1 Density Functional formalism and Exchange Correlation Functional.....</u> | <u>25</u> |
| <u>2.2 Density Functional Theory + Hubbard U approach.....</u> | <u>28</u> |
| <u>2.3 Hybrid Density functional Theory</u> | <u>29</u> |
| <u>CHAPTER 3 TRANSITION METAL OXIDES</u> | <u>31</u> |
| <u>3.1 Solid Oxide Fuel Cell and Properties of Cathode material.....</u> | <u>31</u> |
| <u>3.2 Mixed Perovskite and BSCF as cathode material.....</u> | <u>32</u> |
| <u>3.3 Computational Details</u> | <u>35</u> |
| <u>3.4 Electronic structure of BSCF</u> | <u>37</u> |
| <u>3.5 Oxygen vacancy and cubic phase stability of BSCF</u> | <u>48</u> |

| | | |
|--|---|----|
| 3.6 | <u>Transition State and activation energy search for oxygen vacancy migration in BSCF ...</u> | 54 |
| 3.7 | <u>Conclusions.....</u> | 60 |
| | | |
| <u>CHAPTER 4 PREDICTION OF HEISENBERG EXCHANGE CONSTANTS IN</u> | | |
| <u>ORGANOMETALLIC COMPLEXES</u> | | |
| 4.1 | <u>Magnetic Hamiltonian and Heisenberg exchange constant.....</u> | 61 |
| 4.2 | <u>Theoretical approaches to calculate Heisenberg exchange constants.....</u> | 62 |
| 4.2.1 | <u>Different hybrid DFT approaches.....</u> | 62 |
| 4.2.2 | <u>DFT+U methodology.....</u> | 63 |
| 4.3 | <u>Computational Details</u> | 64 |
| 4.4 | <u>Prediction of Heisenberg exchange constants using DFT+U for binuclear manganese complexes.....</u> | 65 |
| 4.5 | <u>Antiferromagnetic wheel and Heisenberg exchange constant.....</u> | 74 |
| 4.6 | <u>All inner Heisenberg exchange constants for Mn₁₂ based magnetic wheels.....</u> | 76 |
| 4.7 | <u>Density Functional Theory study of Mn₉ based single molecule magnet.....</u> | 89 |
| 4.7.1 | <u>Determination of Ground Spin state of Mn₉</u> | 90 |
| 4.7.2 | <u>Heisenberg exchange constant in Mn₉ system.</u> | 91 |
| | | |
| <u>CHAPTER 5 HYBRID DENSITY FUNCTIONAL THEORY STUDIES OF STRUCTURE AND</u> | | |
| <u>PROPERTIES OF CERIA NANOPARTICLES.I. LATTICE PARAMETERS AND BULK</u> | | |
| <u>MODULI.....</u> | | |
| | | 96 |

| | | |
|------------|---|------------|
| <u>5.1</u> | <u>Cerium oxides and its property</u> | <u>96</u> |
| <u>5.2</u> | <u>Structural relations between cerium oxides.</u> | <u>99</u> |
| <u>5.3</u> | <u>First Principles studies of Ceria published to date.....</u> | <u>102</u> |
| <u>5.4</u> | <u>Computational Details</u> | <u>105</u> |
| <u>5.5</u> | <u>Results and Discussions.....</u> | <u>107</u> |
| <u>5.6</u> | <u>Conclusions.....</u> | <u>115</u> |
| | <u>BIBLIOGRAPHY.....</u> | <u>116</u> |
| | <u>REFERENCES</u> | <u>117</u> |

LIST OF FIGURES

| | |
|---|----|
| Figure 1-1: Number of published DFT papers in different decades (Source http://apps.isiknowledge.com) | 2 |
| Figure 1-2: Different density functionals..... | 3 |
| Figure 1-3: Electronic configuration of first row transition metal compounds | 5 |
| Figure 1-4: Applications of <i>d</i> and <i>f</i> based materials | 7 |
| Figure 1-5: Landmark for computational DFT | 8 |
| Figure 1-6: Available DFT based codes ²² | 10 |
| Figure 1-7: Crystal field splitting of five degenerate <i>d</i> orbitals in tetrahedral and octahedral field... | 11 |
| Figure 1-8 http://science.nasa.gov/headlines/y2003/18mar_fuelcell.htm Anode - Ceria/Nickel cermet , Electrolyte - Gadolinia doped Ceria (CGO), Cathode - LSCF (a four component oxide based on La, Sr, Co, and Fe oxides)..... | 14 |
| Figure 1-9 Oxygen migration pathway in cubic perovskite..... | 15 |
| Figure 1-10 Magnetic wheel complex $[\text{Mn}_{12}(\text{O}_2\text{CMe})_{14}(\text{mda})_8]$: pink balls denote Mn(III), and green ones denote Mn(II)..... | 17 |
| Figure 3-1: Different possible spin states of Fe^{+4} and Co^{+4} in octahedral crystal field. | 44 |
| Figure 3-2: ABO_3 perovskite supercell used for calculation. Here A is barium or strontium (marked by indexes 9-16), B is iron or cobalt (marked by indexes 1-8), and the rest are oxygen atoms (marked by indexes 17-40). | 45 |

Figure 3-3: Jahn-Teller distortion of the coordination octahedron around the Co^{4+} cation is the consequence of the intermediate spin state in the BSCF supercell. Calculated equilibrium distances between Co^{4+} and nearest oxygen ions are shown. 46

Figure 3-4: Raman spectra of BSCF indicates intensity decrease and broadening of $\sim 675 \text{ cm}^{-1}$ peak with elevated temperature 47

Figure 3-5: TEM micrograph showing a particle size and morphology of BSCF perovskite powder 47

Figure 3-6: ABO_3 perovskite supercell used for calculation. Sites B (Iron or Cobalt cations) represented using indexes 1-8, sites A (Barium or Strontium cations) represented using indexes 9-16, while indexes 17-40 represent Oxygen ions..... 50

Figure 3-7: $\text{Ba}_{0.5}\text{Sr}_{0.5}\text{Co}_{0.8}\text{Fe}_{0.2}\text{O}_{2.5}$ supercell ground state structure. Four oxygen vacancies are denoted as V_o . The positions of oxygen atoms in the initial vacancy free lattice are labeled as O_x to demonstrate oxygen atoms displacement accompanying the oxygen vacancies formation 51

Figure 3-8: Elementary step of oxygen vacancy diffusion in a cubic perovskites 54

Figure 3-9: Oxygen migration energetics for (a) symmetric ionic arrangements (corresponds to line 8 in Table 3-5), and (b) non-symmetric environment (line 9 in Table 3-5), (c) special case of tetra-vacancy square formation (line 13 in Table 3-5); the MMO angle in marked next to each image point. 55

Figure 3-10: The NEB images along the oxygen vacancy migration pathway in square tetra-vacancy case..... 56

Figure 4-1 Molecular structures of the binuclear complexes of the benchmark set and Löwdin spin densities in their low-spin (LS) and high-spin (HS) states. 73

| | |
|---|-----|
| Figure 4-2: Schematic diagram of magnetic coupling in Mn12 wheels, number in italics (1-6 and 1'-6') and other numbers are for individual spin. Mn ⁺³ (S=2) green and Mn ⁺² (S=5/2) orange-yellow | 83 |
| | |
| Figure 4-3: Schematic for antiferromagnetic Mn12 wheels | 83 |
| Figure 4-4: Density of states plotted for Mn ₁₂ (Mdea) in S=7 ground state. Positive values present spin up, and negative values present spin down densities. | 85 |
| Figure 4-5: Density of states plotted for Mn ₁₂ (Adea) in S=7 ground state | 86 |
| Figure 4-6: PDOS diagram for d orbitals localized Mn(1) and Mn(3) for Mn12 wheels, the upper row is showing PDOS result for Mn ₁₂ (Mdea) and down row showing Mn ₁₂ (Adea) wheel results | 87 |
| | |
| Figure 4-7: PDOS diagram for d orbitals localized on Mn(2,6) and Mn(4) for Mn ₁₂ wheels, the up row is showing PDOS result for Mn ₁₂ (Mdea) and down row is showing Mn ₁₂ (Adea) wheel results. | 88 |
| | |
| Figure 4-8: [Mn ^{III} ₈ Mn ^{II} O ₃ (OMe) (O ₂ CCMe ₃) ₇ (edte)(edteH) ₂ (N ₃) ₂] | 90 |
| Figure 4-9: Schematic diagram of magnetic coupling in Mn9 in ground state, the green ball is Mn ⁺³ and pink is for Mn ⁺² . Atom 4, 5, 6 is forming an isosceles triangle. | 95 |
| Figure 5-1: a) crystal structure of CeO ₂ fluorite-type cubic structure; b) crystal structure of hexagonal Ce ₂ O ₃ (A type). Ce and O atoms are shown here in black and grey circles respectively | 111 |
| 245 | |
| | |
| Figure 5-2: Side view of MX ₂ sandwich bilayer | 111 |

Figure 5-3: Schematic representation of a) Fluorite type CeO_2 ; b) C type body centered cubic; (c) A type hexagonal sesquioxide. Here solid dots represent metal ions and circles are oxygen ions

216 112

Figure 5-4: Formation of CaF_2 -type structure as ABC stacking of MX_2 sandwich bilayers..... 112

Figure 5-5: Formation of PbCl_2 type structure as stacking and distortion of MX_2 sandwich bilayers.
..... 113

Figure 5-6: Layer structure for Type A..... 114

Figure 5-7: Surface oxygen vacancy by Esch *et. al*⁵⁶ 114

LIST OF TABLES

| | |
|--|----|
| <p>Table 3-1: Lattice parameters a (Å) and bulk moduli B (GPa) calculated for some pure and mixed perovskites. Two different spin states of Co^{+4}, and oxygen vacancy in BSCF are also reported. BSCF calculations are preformed for $2 \times 2 \times 2$ supercell, then divided by 2. The experimental unit cell parameters and bulk moduli are shown for comparison.</p> | 42 |
| <p>Table 3-2: Spin densities on transition metal cations, set up as initial guess and obtained with Lowdin population analysis at SCF convergence for BSCF $2 \times 2 \times 2$ supercell, their relative energies and Boltzmann factors.</p> | 43 |
| <p>Table 3-3: Relative ground state energies of BSCF supercell with respect to different cation positions. The index for cations indicates the positions according to Figure 3-6, and spin states are $s=2$ (Fe), $s=3/2$ (Co). ΔE is the relative ground state energy measured in kcal/mol, C indicates the Boltzmann factors at 1150C.</p> | 52 |
| <p>Table 3-4. Relative ground state energies ΔE (kcal/mol) of 1, 2, 3, and 4-oxygen deficient $\text{Ba}_{0.5}\text{Sr}_{0.5}\text{Co}_{0.8}\text{Fe}_{0.2}\text{O}_{3-\delta}$ supercells with respect to different vacancy positions (denoted according to Figure 3-6). The positions of cations are: Fe=1,5; Co=2,3,4,6,7,8; Ba=10,12,14,16; Sr=9,11,13,15 (see Figure 3-6).</p> | 53 |
| <p>Table 3-5: Transition states and activation energies of the oxygen vacancy hopping between crystallographic sites, calculated for different local cation arrangements in the BSCF supercell.</p> | 59 |
| <p>Table 4-1: Heisenberg exchange constant J for the binuclear complexes, calculated using DFT+U on Mn and ligands ($U(\text{Mn})=2.1$ eV, $U(\text{O})=1.0$ eV, $U(\text{N})=0.2$ eV), DFT+U on Mn only, and pure DFT, compared to BS-DFT predictions and to the experimental data.</p> | 67 |

Table 4-2: Dependence of Heisenberg Exchange Constant (J) on atomic Hubbard U parameters for complex II 68

Table 4-3 Calculated Heisenberg Exchange constants of Mn₁₂(Mdea) using DFT+U and previous first principle calculations. The first column is labeled according to Figure 4-2. Second and third columns are showing the Mn-Mn bond distance from X-ray data and optimized structure respectively. Fourth and fifth column is showing the DFT result reported by Cano *et al.*²⁰⁷ The sixth column is the BSDFT value obtained by fragmenting Mn₁₂(mdea) wheel²⁰⁵. The seventh and eighth columns are J values calculated by DFT+U^{p+d} for X ray and optimized geometry. The last column is representing the Heisenberg Exchange constants for Mn₁₂(Adea)..... 82

Table 4-4: Löwdin Population analysis for Mn₁₂(Mdea) and Mn₁₂(Adea) 84

Table 4-5: Energy differences between different spin orientations in Mn₉, first nine columns are presenting the spin of Mn atoms in different spin orientations labeled according to Figure 4-9, 10th column is multiplicity; the 11th column is energy difference in kcal/mol, from stable most spin state. The HS is designated where we have maximum possible multiplicity and all orientations are ferromagnetic, the multiplicity 28,22,20,12 are designated as IS, LS is describing the multiplicity 6, and suffix(s) are indicating the index of Mn according to Figure 4-9 94

Table 4-6: Heisenberg exchange constant for two adjacent metal centers, first column is the Heisenberg exchange constant labeled according to Figure 4-9, next column is distance between Mni and Mnj, the third one is Heisenberg exchange constant, and fourth and fifth column is calculated and ideal spin coupling according to eq (4-7) 95

Table 5-1: Lattice parameter and bulk modulus of CeO₂ using different methods 109

Table 5-2: Lattice parameter and bulk modulus of Ce₂O₃ obtained with different methods. Val and Core indicate *4f*-electron treated explicitly or with the Effective Core Potential respectively.

Antiferromagnetic (AF) ,Ferromagnetic (FM) 110

CHAPTER 1 INTRODUCTION

Investigations of electronic structures of different functional materials using quantum mechanical simulation become an almost obligatory tool in present day science. This understanding is a key feature behind the tailoring new materials for specific applications like spins based electronics, energy applications, drug design, catalysis are to name few. In addition to physical and life science contributions in this field its worthwhile to mention present advancement of computer hardware and softwares also a reason to the tremendous growth in this field. To deal with a larger molecular system one needs to make a compromise between the computational cost and the accuracy of results. In that purpose Density functional theory (DFT) has now become the preferred method for electronic structure theory, its cost scales favorably with system size than does the cost of other expensive quantum mechanical method based on wave function theory. In addition to reasonable computational cost it can yet competes well in terms of accuracy. Figure 1-1, shows a graph according to web of science is presenting the number of paper published by using DFT calculations in last four decades. In 1970-1980 the number was **53**, increased by **thousand times**. This tremendous growth in terms of publication is a proof of popularity of this method in scientific community.

A breakthrough in these computational efforts was realized in 1964 when Walter Kohn and coworkers developed the density functional theory (DFT), a theory based on electron density, which is a function of only three spatial coordinates.^{1,2} The Kohn–Sham equations of DFT cast the intractable complexity of the electron–electron interactions into an effective single-particle potential determined by the exchange-correlation functional. This functional (i.e., a

function whose argument is another function) describes the complex kinetic and energetic interactions of an electron with other electrons. In 1992 John Pople, of Northwestern University in Evanston, IL, added DFT--including the latest functional to his widely-used chemistry computer program GAUSSIAN. Kohn and Pople received the Nobel Prize in chemistry for their contributions to computational chemistry in 1998.

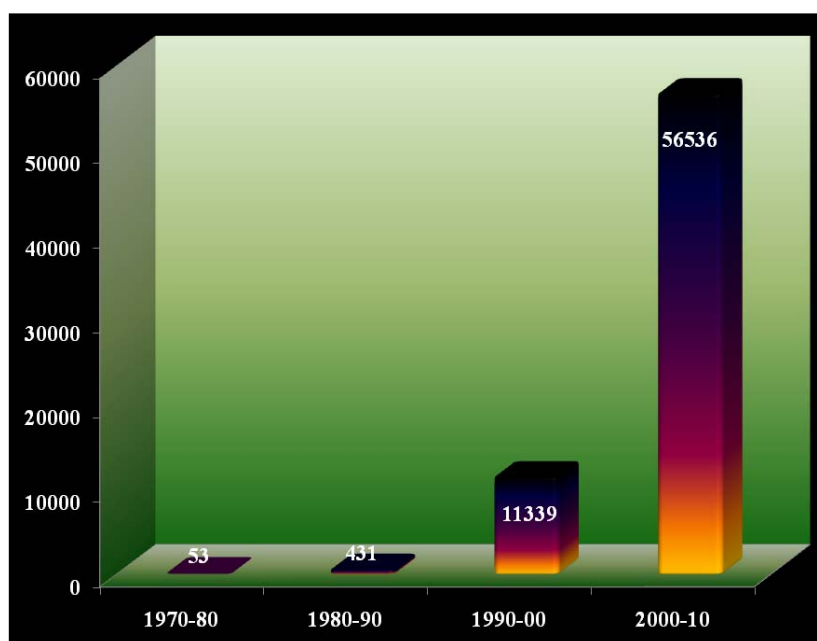


Figure1-1: Number of published DFT papers in different decades (Source <http://apps.isiknowledge.com>)

In this introduction now we are giving a brief tour of evaluation of DFT protocol. The oldest approximation to a density functional is the Dirac–Slater approximation depends only on spin densities^{3,4} or local spin density approximation (LSDA). It can be derived from the exact exchange energy of a uniform electron gas (UEG). Modern forms of the LDA are based on the total energy of the homogeneous electron gas derived from quantum Monte Carlo calculations. The generalized gradient approximation (GGA) introduces a dependence of exchange energy on the local gradient of the electron density. Meta-GGA functionals use the kinetic energy density

(or the Laplacian of the electron density) as an additional variable.⁵ Hyper-GGA uses Kohn–Sham one electron wavefunctions (instead of the many-body wavefunctions) to evaluate the Hartree–Fock exchange formula; this is commonly called “exact” exchange. Hybrid functional^{6,7} mix exact (i.e., Hartree–Fock) and DFT exchange. We have listed the following functional types and functionals:

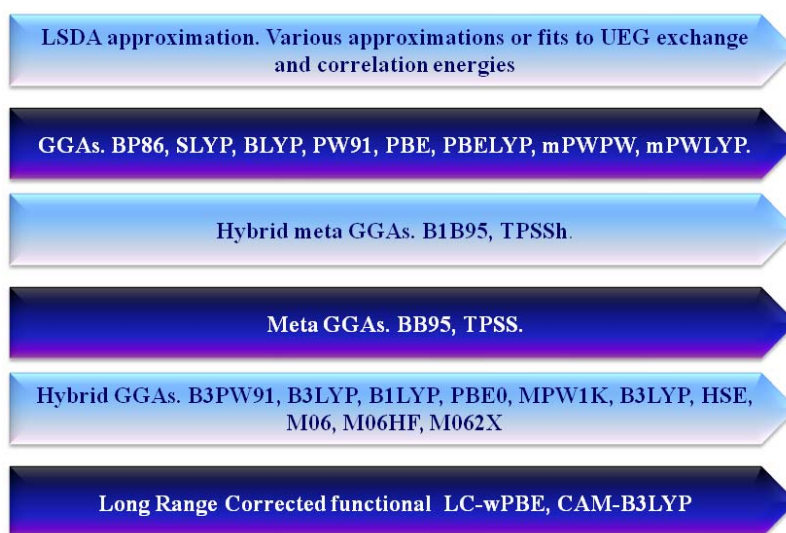


Figure 1-2: Different density functionals

Another approach to reducing these inaccuracies is DFT + U approximation,⁸⁻¹⁰ which becomes LSDA + U or GGA + U, depending on the type of density functional employed. The +U modifications amend self-interaction by using system-dependent parameters (for solids, the parameters should probably also depend on pressure or molar volume and on phase, and for molecules on geometry). The +U modification takes one out of the realm of DFT and into a less rigorous model Hamiltonian approach, but it is instructive in the way it corrects DFT. The method is approximate and not uniquely defined¹¹ and is employed in a variety of nonequivalent ways by different researchers, but the various versions attempt to enforce the same physical

corrections by adding a Hubbard-like¹² term to the DFT energy. A key issue in essentially all implementations is the inclusion of the Hubbard-like term only in a basis of localized *d* electrons (or *f* electrons). The Hubbard-like term adds a penalty for non-idempotent density matrices in this subspace and therefore it favors filling *d* orbitals that are localized on one particular atom¹³ (a “correlation” effect), which sometimes also favors high-spin states on each atom and therefore less covalent, bonding in molecules or antiferromagnetic coupling in solids. The +U correction would be expected to be smaller for a GGA than for LSDA, and smaller yet or not needed for a well balanced hybrid functional; for accurate results, the +U correction should depend on the structure.¹⁴ In some cases, for example solid MnO,¹⁵⁻¹⁷ FeO,^{15,16,18} and Co,^{15,16,18} the +U approach and the inclusion of partial Hartree–Fock exchange lead to similar results, which are much better than GGA, and one anticipates that the methods would be even more similar if the Hubbard like term were included for the entire electronic space rather than just the metal *d* space.¹⁷

In broad aspect materials can be divided into two basic classes a) Carbon based materials or organic materials and b) inorganic materials. Inorganic materials can have metal or not. For metal based systems we mostly see open shell *d* and *f* based compounds. This open shell nature in *d* shell is capable of multiple valence states (e.g. Mn can have +2, +3, and +4). For *f* based systems though it is not very common still we can see Ce (+3 and +4) states. This multiple valence property of *d* and *f* metal leads to different applications including insulators, semiconductors, conductors, or superconductors, and they may have interesting magnetic, ferroelectric, antiferroelectric, and piezoelectric properties. These important modern technological applications lead scientific community to investigate in deep of these materials.¹⁹

| The electronic structures of the First row d block elements | | | |
|---|------|--|-----------------|
| Sc | [Ar] | | 4s ² |
| Ti | [Ar] | | 4s ² |
| V | [Ar] | | 4s ² |
| Cr | [Ar] | | 4s ² |
| Mn | [Ar] | | 4s ² |
| Fe | [Ar] | | 4s ² |
| Co | [Ar] | | 4s ² |
| Ni | [Ar] | | 4s ² |
| Cu | [Ar] | | 4s ² |
| Zn | [Ar] | | 4s ² |

Figure 1-3: Electronic configuration of first row transition metal compounds

We listed in Figure 1-3 here first row transition metals showing general tendency of having d^n configuration ($n=1-10$). We normally exclude Zn because Zn^{+2} has closed 3d shell. The Mn, Fe, Ni are highlighted because, we used this three transition metal based complexes and solids for our study. It is obvious that with increasing number of electrons computational costs also increases by significant amount. To reduce this cost most of the time the only valence electrons in the elements are treated explicitly. The rest of the core electron is replaced by a potential called effective core potential or pseudopotential. In next part we are elaborating four different key applications (Figure 1-4) which are studied in details in later parts of this thesis.

Magnetism and Magnetic Materials: The amplification in the recording density of hard disk drives by a magnitude of eight orders during the past 50 years (see the May 2006 issue of *MRS Bulletin* on “Materials for Magnetic Data Storage”) has been obtained by slimming down

the bits size in the magnetic storage layer. Recently, based on DFT calculations, tetragonal iron cobalt alloys were proposed as promising materials with the desired high uniaxial magnetic anisotropy and high saturation magnetization.²⁰ Molecular magnets (a special class of organometallics) are also suggested a special class of compound having potential application to be a part for quantum computer. To design a tailored molecular magnet needs prior knowledge of its magnetic properties. DFT calculation is enormously using to investigate magnetic properties in these materials.

Oxides and Minerals: Applications of DFT have predicted such fundamental properties as the properties of iron and (Mg,Fe)SiO₃ under the extreme pressures and temperatures of the Earth's interior. The metal oxides shows its wide range of application starting form catalysis, electrolyte, cathode, anode, semiconductor, superconductor to name a few. The application of DFT in transition-metal oxides is a difficult task, as the spurious self-interaction error in DFT overly delocalizes electrons, leading to excess metallic behavior and the wiping out of mixed-valence states in doped oxides, affecting local spin magnetism, conductivity, and even phase stability.

Semiconductors and Nanotechnology: All the device industry now days are based on semiconductor. The key property in these materials is the energy gap between valence and conduction bands. To design new materials one needs to suggest an appropriate band gap. This is one of the most important challenges for DFT community. Pure DFT is well known for not to calculate band gap due to self-interaction error. This error leads to artificial stabilization of delocalized states. The effect is the most evident in systems with an odd number of electrons. Hybrid DFT and DFT+U extensively used to calculate band gap.

Biomaterials: DFT calculations play an increasingly important role for understanding complex processes in biological materials. The charge transfer inside the complexes, solvation kinetics, protein folding, binding site are couple of examples. The excited state dynamics of this complexes (especially complexes taking part in photosystem) are one of the key interest in solar system researchers.

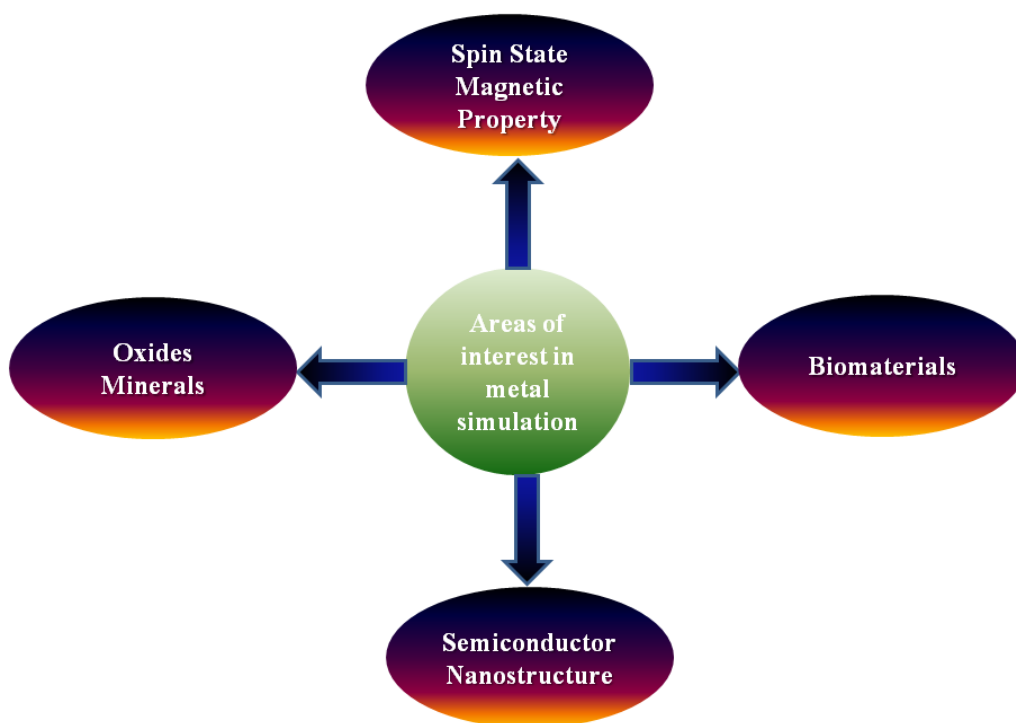


Figure 1-4: Applications of *d* and *f* based materials

With modern computational hardware and software, nowadays we can perform DFT calculation for large systems, in using QBOX software Gygi F, Galli G²¹ performed a calculation for 1000 molybdenum atoms. The other large scale calculation landmarks are also shown in the Figure 1-5.

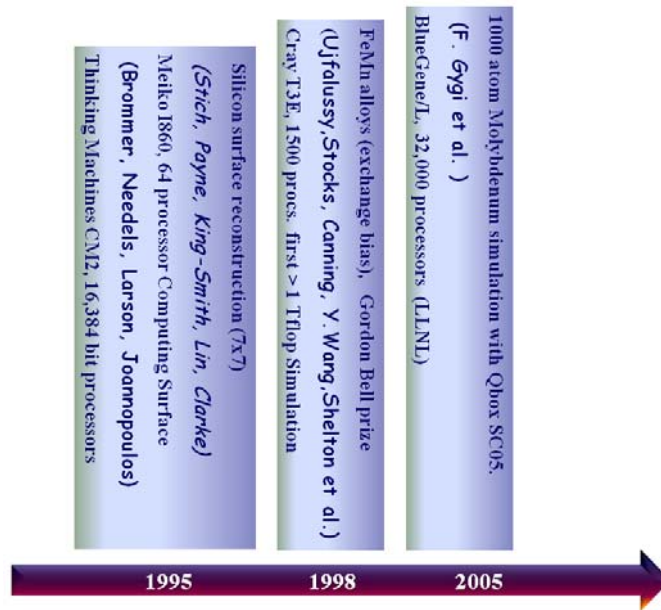


Figure 1-5: Landmark for computational DFT

Moving from system of interest and large scale computation benchmarking study now we can discuss the how DFT can be use for successful material design, the steps are as follows

- (1) Formulating an experimental problem to a computable model.
- (2) Calculations of the required electronic as well as physicochemical properties,
- (3) Validation of the simulation results by confrontation with laboratory experiments.
- (4) After validation of a certain protocol use it to predict properties of new materials.

DFT calculation is popular because of available codes for materials scientific community. Some codes are accessible thorough general public licenses, others are for paid users. The codes have diverse range of basis sets, potentials, exchange-correlation functionals, as well as different algorithms for solving the Schrödinger equation. A summary of existing DFT codes is given in Figure 1-6 obtained from an editorial article by Hafner, Ceder and Wolverton.²² In VASP and ABINIT all-electron PAW method is implemented. VASP aand CPMD both have exact exchange and hybrid functionals. To use use pseudopotential based codes one needs to be careful

about choosing well validated pseudopotentials . In some codes we can see external library of pseudopotentials developed by the code developer. All-electron codes use either local or augmented plane-wave basis sets. DFT, exact exchange, and hybrid calculations all together is implemented in both Gaussian 03 and CRYSTAL codes. FPLO is useful especially for second row and third row transition metals along with lanthanides because it solves Dirac equation. DMol3 is a numerical basis set based code, this code can be employed either in an all-electron mode or through semilocal pseudopotentials. For full-potential LAPW methods one can use WIEN2K, FLAIR, and QMD-FLAPW(all of them are all electron codes). For benchmarking pseudopotential codes we can use all electron codes. Unit cells with a few hundred atoms with pseudopotential and PAW codes, are not even that difficult due to highly parallel implementation of codes.

| Code Name | Basis Set | Potentials |
|---|-----------------------|------------|
| Plane Wave Pseudopotential Codes | | |
| ABINIT | Plane Wave | Pseudo |
| CASTEP | Plane Wave | Pseudo |
| CPMD | Plane Wave | Pseudo |
| DACAPO | Plane Wave | Pseudo |
| FHIld | Plane Wave | Pseudo |
| PWscf | Plane Wave | Pseudo |
| VASP | Plane Wave | Pseudo,PAW |
| Pseudopotential Codes with Other Basis Sets | | |
| Quickstep | Gaussian + plane wave | Pseudo |
| SIESTA | Local/numerical | Pseudo |
| All-Electron Codes | | |
| CRYSTAL | Local | Pseudo |
| FPLO | Local | Pseudo |
| Gaussian 09 | Local | Pseudo |
| ADF | Local | Pseudo |
| DMOL3 | Local/Numarical | Pseudo |
| FLAIR | LAPW | Pseudo |
| QMD-FLAPW | LAPW | Pseudo |
| WIEN2k | LAPW | Pseudo |

Figure 1-6: Available DFT based codes²²

In this work we used two DFT based codes ESPRESSO and Gaussian. Since we investigate the materials having strongly correlated electrons we used two different self interaction correction scheme a) Hybrid DFT and ii) DFT+U. The thesis is organized in the following way. In the first chapter we described the motivation behind our work. Explaining crystal field theory of transition metals in octahedral field, which is essential to illustrate electronic structure of transition metal oxides as well as molecular magnetic complexes. Later sections of this chapter are detailing the applications of the systems we investigated. In chapter 2

we described the DFT formalism and then the modification we used over DFT. Chapter 3 is the prediction of electronic structures and activation energy of oxygen migration of mixed transition metal oxides. Next chapter is showing the prediction of spin state orientation of molecular magnetic complexes. For this sensitive property pure DFT was not sufficient, we used certain modifications over pure DFT by adding onsite coulomb repulsion on both metals and ligand in the molecules. We validate our protocol by using a benchmark set for five bimetallic complexes and applied it on two molecular magnetic complexes. The correct qualitative and quantitative prediction shows our theoretical protocol can be use to suggest a rational design of molecular magnetic complexes. The final chapter is about prediction of lattice parameter of cerium (III and IV) oxides by considering explicit f electron on the metals. In this chapter first we described previous theoretical approaches applied to study these oxides and why the lattice parameter validation is challenging. In the next section in that chapter we wrote the detail methodology of our calculation. The key part of this calculation is generation of initial guess. Our result shows good agreement with experimental findings.

1.1 Transition metals and Crystal field splitting in octahedral field

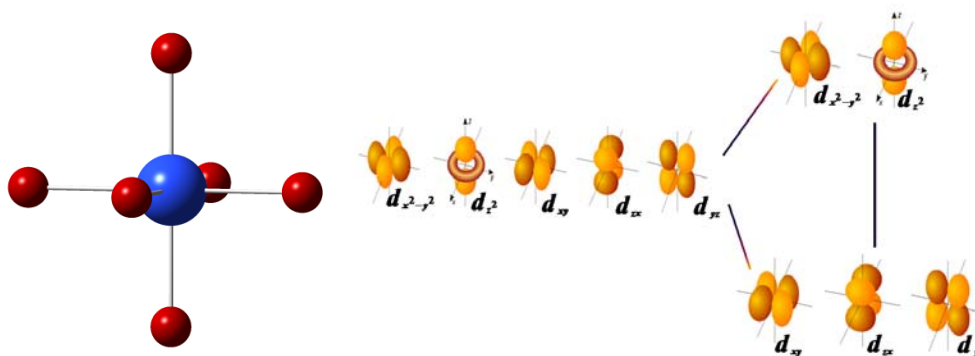


Figure 1-7: Crystal field splitting of five degenerate d orbitals in tetrahedral and octahedral field

First principle study of the transition metals are challenging because of the presence of open shell d electrons. To investigate electronic structure of metals having open shell d electrons one needs to analyze it using crystal field theory. The five d orbitals in an isolated, gaseous metal ion are degenerate. If a spherically symmetric field of negative charges is placed around the metal, the orbitals will remain degenerate, but all of them will be raised in energy as a result of the repulsion between the negative electrons in the orbitals. If the field results from the influence of real ligands (either anions or the negative ends of dipolar ligands such as NH_3 or H_2O), the symmetry of the field will be less than spherical one. As a result the degeneracy of the d orbitals will be removed.

Since we mostly studied complexes having octahedral or near octahedral coordinations, we are discussing the crystal field splitting of a metal ion in only octahedral field. From Figure 1-7 we can see the orbitals along the axis (i.e. $d_{x^2-y^2}$ and d_z^2) will be more strongly repelled than the orbitals with lobes directed between the axes (the d_{xy} , d_{zx} , and d_{yz}).

In octahedral crystal field Co^{4+} can have three possible spin states, $t_{2g}^5 e_g^0$ ($s = 1/2$), $t_{2g}^4 e_g^1$ ($s = 3/2$), and $t_{2g}^3 e_g^2$ ($s = 5/2$) with one, three and five unpaired electrons, respectively. Fe^{4+} can have two possible spin states in the octahedral splitting with two and four unpaired electrons. These states have configurations as $t_{2g}^4 e_g^0$ ($s = 1$) and $t_{2g}^3 e_g^1$ ($s = 2$). We can refer these states as low spin (LS) with one unpaired electron, intermediate spin (IS) with three unpaired electrons, and high spin (HS) states with five unpaired electrons for Co^{4+} , and as LS and HS states for Fe^{4+} cation according to their multiplicity. This is an example that same numbers of d electrons in a metal ion can show different possible spin states. To predict the electronic structure of

molecules and crystals having “*d*” and “*f*” metals we need to investigate correct crystal field configurations. In section 3-4 we discussed more details about it.

1.2 Computational studies on oxygen migration of perovskites

To suggest better cathode material in solid oxide fuel cell, one needs to estimate the ease of oxygen diffusion. To calculate this property we need to predict the activation energy of oxygen migration in atomic environment. Computational studies of ionic transport were reviewed by Islam.²³ He emphasized the importance of three factors: dopant/defect association, ion migration mechanism, and surface structures. Several theoretical studies have focused on vacancy mobilities.²⁴⁻²⁶ Based on their Monte Carlo (MC) simulations, Meyer *et al.*²⁵ concluded that the mobility of vacancies is reduced in the neighborhood of dopant ions. This is in agreement with other experimental results and with molecular dynamics (MD) simulations by Shimojo and Okazaki.²⁴ More detailed investigation requires evaluation of the activation energies of the elementary steps for vacancy diffusion and the atomic mechanism for each elementary step. Eichler²⁷ studied diffusion barriers for oxygen ions at several locations in a supercell of tetragonal yttrium-stabilized zirconia with a distorted fluorite structure. The energy for oxygen diffusion was assumed to be the difference between the highest and lowest energies along a linear path connecting occupation sites. Recent research by Ramanarayanan *et al.*²⁶ suggested that such an approach can serve as an approximation only because the path is assumed to be linear instead of being optimized. The mechanism of oxygen ion migration in perovskite oxides was studied with atomistic simulations by several authors.^{28,29} They reported that ion migration involves a curved pathway. Indeed, a recent neutron scattering study of pure and doped LaGaO₃³⁰ provides evidence in favor of this prediction. Several *ab initio* studies of oxygen vacancy

diffusion in perovskites appeared in the literature only recently. Karki *et al.*³¹ studied the orthorhombic perovskites and post-perovskite phases of MgSiO_3 . In order to calculate the migration enthalpy, they have chosen the saddle point at which a migrating ion is placed exactly halfway between the initial and destination sites from where the ions are removed to create vacancy sites. A more advanced approach was taken by Ammann *et al.*³² for the same system. They searched for the minimum energy position of the ion constrained to the saddle plane. While this search resulted in fairly complex Si migration pathway, the midway position was found to be close to the true saddle-point in case of oxygen migration. Both straight line and curved pathways for oxygen diffusion in LaAlO_3 perovskite were investigated by Hernandez *et al.*³³ using the climbing image nudged elastic band approach. They found straight line to be less favorable than the curved pathway showed in Figure 1-9.

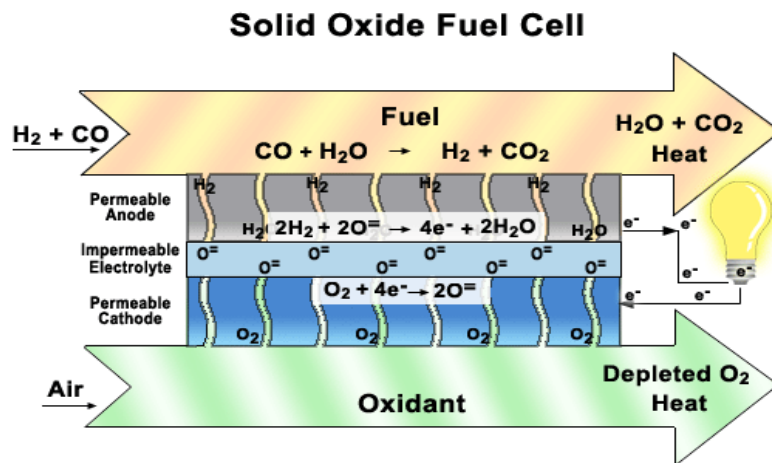


Figure 1-8 http://science.nasa.gov/headlines/y2003/18mar_fuelcell.htm Anode - Ceria/Nickel cermet, Electrolyte - Gadolinia doped Ceria (CGO), Cathode - LSCF (a four component oxide based on La, Sr, Co, and Fe oxides)

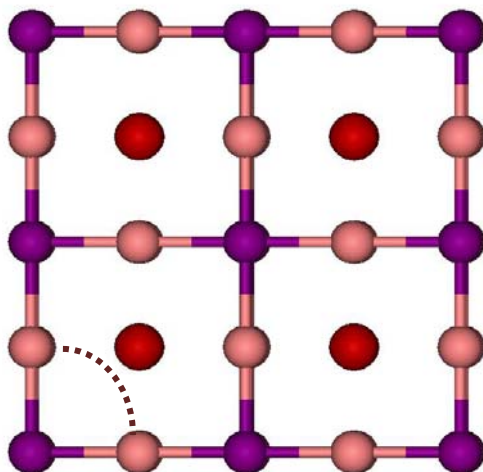


Figure 1-9 Oxygen migration pathway in cubic perovskite

1.3 Molecular magnet and antiferromagnetic wheel and application in spintronics

In chapter 4 we moved from crystal to molecule. This chapter is focused on the spin state alignment energetic of single molecule magnets (SMM). SMMs attracted interest physicists and chemists since their initial discovery in 1993.^{34,35} Typical SMMs belong to the class of polynuclear transition metal complexes. They are characterized by a large spin ground state and considerable negative anisotropy leading to a barrier for the reversal of magnetization. SMMs are also characterized by slow magnetization relaxation and can be magnetized below their blocking temperature.^{34,35} For these reasons, SMMs hold a great promise as potential elements of molecular spintronics and quantum computers.³⁶⁻³⁸ Spintronics is a rapidly developing area of nanotechnology, where device operation requires active manipulation of the spin degrees of freedom (in addition to the electric charge, used in traditional semiconductor electronics devices). Use of molecular elements in spintronics can take advantage of the chemical, structural and electronic versatility provided by the molecular structures. In molecular systems electron spins can be preserved for longer time periods and distances than in conventional inorganic

materials. The low density, flexibility, transparency, processability and novel added functionalities (magnetic switching at the molecular level, emission of light, etc.) can also be advantageous for the design of spintronic devices.

Single molecules, similar to the ones considered in this study have the size c.a. 20Å and can be used as the smallest “bits” for magnetic storage and processing of information.³⁹ Presently accessible magnetic domains have 20 nm in size, and their further miniaturization is complicated by approaching the superparamagnetic limit.⁴⁰ However, this limit does not apply to magnetic molecules, because the magnetic order is determined by the electronic structure of a molecule and not by a certain critical size. In order to become practical, the intramolecular magnetic interaction have to be strong enough to prevent decoupling of the spins within the molecule by thermal fluctuations, so that the single molecule effectively behaves as an atom with a large spin S .³⁹ Moreover, a high magnetic anisotropy is required to prevent spontaneous reorientation of the magnetization of the molecular unit, i.e. to increase its blocking temperature.³⁹ The interaction between molecular magnetic properties and charge transport is another important issue to be considered. The combination of different properties to accomplish desirable functionality makes the rational design of the molecular magnets with optimized properties increasingly important for the spintronic applications.

The idea of using SMMs to implement the idea of quantum computer was proposed by Leuenberger and Loss.³⁷ Instead of the classical bits, which can take only one value (1 *or* 0), quantum computers operate with quantum bits (qubits, prepared in quantum superposition state of 1 *and* 0) and carry out multiple operations at the same time. The electron spin is a natural candidate for a qubit, as its interaction with environment is weaker than for the charge state. The

spin can be controlled by electron spin resonance impulse in order to write, transform, and read out the information on a quantum state of the multilevel system.

Long decoherence time is critically important for the successful realization of the quantum computer.^{37,41,42,43,44} A specific type of molecular magnets, called antiferromagnetic molecular wheels attracted especial attention for this reason.^{45,46,47,48} Unlike other types of molecular magnets, magnetic wheel has only one single loop of the fused transition metals polyhedra. Mn₁₂ based wheel was first reported by Rumberger *et al.*⁴⁹ The smallest molecule of this type is the recently reported tetranuclear manganese complex, [Mn₄(anca)₄(Htea)₂(dbm)₂] · 2.5Et₂O, reported by Beedle *et al.*⁵⁰ The larger wheels include the [Mn₂₄] wheel,⁵¹ the [Mn₂₂] wheels,⁵² and the [Mn₈₄] wheel.⁵³ The largest reported spin ground state for a wheel-shaped SMM is S=14 for the [Mn₁₆O₂(OCH₃)₁₂(tmp)₈(CH₃COO)₁₀] · 3Et₂O wheel reported by Manoli *et al.* in 2007.⁵⁴

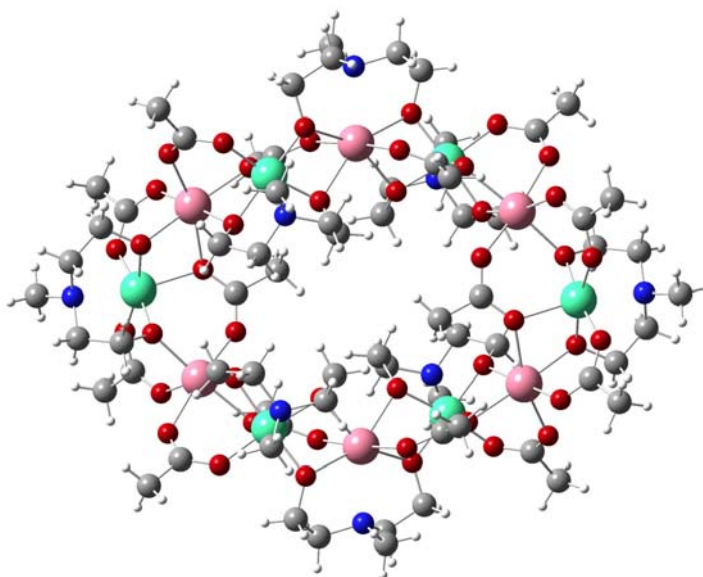


Figure 1-10 Magnetic wheel complex [Mn₁₂(O₂CMe)₁₄(mda)₈]: pink balls denote Mn(III), and green ones denote Mn(II).

1.4 Cerium oxides and its property

Surface structure of metal oxides holds the key to understanding their catalytic properties.⁵⁵ The surface oxygen vacancies are suspected to participate in various chemical reactions catalyzed by metal oxides. Vacancies are also bind adsorbents more strongly than normal oxide sites and assist in their dissociation.⁵⁶ Oxygen vacancies are also involved in photo catalysis on oxides, and their changed nature may control band bending thus electron-hole pair separation.

Since the most of ceria properties are determined by its surface, films and nanoparticles (NP) make the most efficient use of this material. Resulting surface structure depends both on nanoparticle size, and on fabrication method. Films can be produced by several growth technique, electron beam evaporation (EBE)⁵⁷⁻⁵⁹ pulsed laser deposition⁶⁰⁻⁶², metalloorganic chemical vapor deposition⁶³, ion beam assisted deposition (IBAD)⁶⁴, reactive magnetic sputtering.⁶⁵ Ceria thin films are used to fabricate anode material for intermediate temperature solid oxide fuel cell (IT-SOFC). Replacement of yttrium-stabilized zirconia with doped ceria as anode material in IT-SOFC allows to the lower the operating temperature 500⁰C.⁶⁶ Thin film of CeO₂ exhibits a high refractive index, and high dielectric constant, so it is a very promising material to use for optoelectrical, microelectronic, electro-optical devices.⁵⁷ The doped ceria films are transparent for the wave lengths of or above 500nm and show no optical loss around 600⁰C. Ceria thin films made by pulse laser ablation and having thickness about 1000 Å are used in optoelectronic devices.

Ceria NPs (nanoceria) had been extensively studied since early 1970s, but for inadequate characterization facility those cannot be properly characterized, in recent years with the development of experimental techniques as well as the help of theoretical studies this area is

much widely explored. In a review article it is told that from June 1993 to end of 1998, there was 560 papers had been published.⁶⁷ Basically in theoretical field from mid 1990 simulated annealing and interionic potentials are used to investigate the structure and reductability of intermediate valance ceria nanoparticle.⁶⁸ The most applications of nanocrystalline ceria are based on its oxygen storage capacity and electronic properties. Although CeO₂ has a wide band gap of 6 eV⁶⁹ and acts as an insulator, in the higher temperature region (300⁰C-400⁰C) and in reduced oxidation state it demonstrates an enhancement of the electric conductivity,⁶⁰ which is a disadvantage for some applications. Adachi in his review referred that composite contained nano particle 4.1nm having band gap 3.42 eV and with 5.37nm nanoparticle it is 3.37eV.⁷⁰

Like bulk ceria nano cerium dioxide also exhibit phase transition from fluorite phase to orthorhombic phase , the lattice pappmeter of the orthorhombic phase is a=5.641 b=6.647 c=3.481 , but the difference is nano cerium dioxide shows bulk modulus 328 ±12 GPa⁷¹ in contrast with bulk cerium dioxide 230 GPa. The phase transition pressure (22.3 GPa) is also very low compared with bulk one (31 GPa),⁷² this observation is quite anomolas with other nano oxide and sulfides , the author suggested that larger volume collapse and exsistance of unstable high pressure phase is responsible for the decrease of transition pressure of nano cerium dioxide compared with bulk.⁷¹

Nanoceria used in design a three way catalyst for automobile exhaust,⁷³ since ceria catalytically oxidizes hydrocarbons to water, carbon monoxide to dioxide and nitrogen oxides to nitrogen. Ceria NPs are also used for promotion of water gas shift, steam reforming reaction, and carbon monoxide removal,⁷³ The oxygen vacancies play an important role for the catalytic

activity of ceria. Zirconia doped ceria ($\text{CeO}_2/\text{ZrO}_2$ solid solution) can operate at lower temperature around 600°C than pure ceria catalyst.⁷⁴

I) There are different methods of preparing cerium oxide nanoparticle

a) In colloidal medium cerium (III) forms crystalline oxydicarbonate solid particle, this oxydicarbonates were readily converted to the corresponding oxides of ellipsoidal shape by calcination at 600°C , while the other rare earth elements yields sols of amorphous spherical particle.⁷⁵

b) Fine particle by gas condensation -, in this method cerium oxide form by using inert gas condensation of a metallic cerium precursor, followed by oxidation using a magnetic sputtering.⁷⁶

c) Fine particle by solgel method - In this method submicron size of cerium dioxide nanoparticles are prepared, the sol is made by using cerium nitrate, and the precipitation of cerium (+3) hydroxide uses basic medium.⁷⁷

d) Combustion method it is based on the solid state combustion process based on the principle of explosive decomposition of nitrate urea mixture in a low temperature s in a low temperature such as 500°C , using this method cerium oxide particle size obtained is $1\ \mu\text{m}$.⁷⁸

There are some other methods such as aging cerium(III) nitrate solution with hexamethyl tetraamine . Oxidation from +3 to +4 state occurs in precipitate and then the wet precipitate is crystallizes to dioxide.⁷⁹

There is another method which used calcination , For this synthesis, in cerium chloride $\text{CeCl}_3 \cdot 7\text{H}_2\text{O}$ solution is used, ammonia was added dropwise and that changes the pH of the solution from 2.5 to a final value 11.4. This addition causes the precipitation of yellow

gelateneous $\text{Ce}(\text{OH})_3$, after filter and wash the mixture with water and acetone, then the resultant mixture is calcinated.

Depending on size of ceria nanoparticle different models are used to describe the particle size and lattice parameter relationship, Baranchikov *et al.*⁸⁰ showed that a value changes from 5.47 Å to 5.41 Å (the latter value corresponds to bulk CeO_{2-x}) within the particle size range of 2.2–34 nm. They synthesized by the following methods. Solutions of $\text{Ce}(\text{NO}_3)_3 \cdot 6\text{H}_2\text{O}$, $\text{CeCl}_3 \cdot 7\text{H}_2\text{O}$, $\text{Ce}(\text{SO}_4)_2 \cdot 4\text{H}_2\text{O}$ and $(\text{NH}_4)_2\text{Ce}(\text{NO}_3)_6$ (0.02, 0.08, 0.3, 0.8 mol L⁻¹) in water/isopropanol mixtures (1 : 1 to 1 : 19, v/v) were rapidly added under vigorous stirring to aqueous ammonia (3 mol L⁻¹). Noticeable deviation of unit cell parameter value from that one for the bulk state can be observed for particles less than 5 nm. Particle size is the only decisive factor determining ceria unit cell parameter.

Data obtained can be adequately fitted using power-law relation:

$$\Delta a = a - 0.5409 = 0.025 \times D^{-2.1} \quad (1-1)$$

In another model proposed by Wu *et al.*⁷⁴ the lattice parameter can be illustrated as a function of particle diameter for CeO_{2-x} particles which are assumed to consist of a layer of $\text{CeO}_{1.5}$ on a core of CeO_2 . The lattice parameters for fluorite structure CeO_2 and average fluorite structure $\text{CeO}_{1.5}$ were taken to be 0.541 and 0.561 nm, respectively. The lattice parameter for $\text{CeO}_{1.5}$ was approximated to be one half of that of the C-type sesquioxide Ce_2O_3 proposed by Tsunekawa *et al.*⁸¹ Results were published by Wu *et al.*⁷⁴ relatively close to the data reported by Tsunekawa *et al.*⁸¹ On the other hand, the increases in the lattice parameters with decreasing particle size for those reported by Zhang *et al.*⁸² were significantly smaller than and that of Tsunekawa *et al.*⁸¹ This implies that the surfaces of their particles were barely reduced to $\text{CeO}_{1.5}$ and the small

increase in their lattice parameters with decreasing particle size could be due primarily to vacancies in bulk of the particles according to Raman spectra.

According to Baranchikov *et al.*⁸⁰ they estimated size of ceria nanoparticles which corresponds to complete transition of cerium atoms into +3 oxidation state. Within the framework of Tsunekawa *et al.*'s⁸¹ model, this critical size appeared to be approximately 1.1 nm. In turn, according to model proposed by Wu *et al.*⁷⁴ reduction of Ce(IV) with the decrease of particle size results in formation of Ce₂O₃ with fluorite structure having disordered oxygen vacancy sublattice. Unit cell parameter of fluorite Ce₂O₃ was estimated to be 5.56 Å.⁷⁴ Critical particle size of ceria calculated using this model and relation appeared to be approximately 1.2 nm. It should be noted that thus estimated critical size values are nearly equal to double unit cell parameter of cerium dioxide. In other words complete reduction of Ce(IV) takes place when all CeO_{2-x} unit cells are on the surface of a particle.

Different synthetic methods have significant impact in ceria nanoparticle size and the corresponding lattice parameter.

The cerium dioxide nanoparticle obtained from microemulsion method.⁸³ This micro emulsion system consist of surfactant sodium bis (2 –ethyl hexyl) sulphosuccinate (AOT), toluene, and water. Cerium dioxide deposited in non agglomerated form in organic medium and in agglomerated form in aqueous phase , this nanoparticle size and lattice parameter shows the following relation,⁸⁴

$$\Delta a = 0.031D^{-0.4763} \quad (1-2)$$

Here the Δa is $(a - a_0)$ where “a” is lattice parameter of nano particle and the a_0 is lattice parameter of bulk cerium dioxide i.e 5.411 Å, D is particle size.

Another work had shown that particle synthesized by sol-gel method and hydrothermal process obtained a different relation⁸⁵

$$\Delta a = 0.0324D^{-1.04} \quad (1-3)$$

Wu and co worker used Vapor phase condensation for the synthesis and they showed the following relation⁷⁴

$$\Delta a = 0.0600D^{-1.05} \quad (1-4)$$

The crystal structure is studied by HRTEM. HRTEM method is useful for atomic level imaging, HREM is required to determine the purity of the crystal combination with real-time video recording and image processing tool for crystal defect study, so for cerium oxide, it is extremely important to investigate the defects inside the crystal.⁷⁰ Despite having an ordered crystalline structure,⁸⁴ nanoceria was shown to be extremely sensitive to perturbation in pH, ionic strength, and concentrations,⁸⁴ which can dramatically modify thermodynamic stability of ceria NPs. Destabilization may occur from a high surface to volume ratio for the NP and from the strong reactivity of the surface chemical sites to the physicochemical changes. X-ray diffraction found the lattice parameter to increase by 0.45% as the particle size decreased to 6 nm.⁸⁴ This lattice expansion was attributed to the increasing concentration of oxygen vacancy defects with decreasing particle size and increasing surface to volume ratio.

In order to understand the catalytic activity of nanoceria, experimental investigation must be complemented with the first principles calculations of electronic structure. In this series of papers we intend to conduct such an investigation. Atomistic structure of ceria surfaces, including oxygen defects is critically important first step the set goal. In this first paper of the series we intend to establish an accurate yet computationally inexpensive level of theory, suitable

to describe ceria, and its mixed-valence nature. Our short-term goal is to find optimal lattice parameters and bulk moduli for the ideal bulk crystal structure in CeO_2 and Ce_2O_3 , then use them to find dependence of lattice parameter for the partially reduced phases CeO_{2-x} on the composition x and compare it with the experiment. In Section 5.2 we establish structural relations between ceria oxides, in Section 5.3 we review the first principles studies of ceria published to date, Section 5.4 describes the details of our approach. We present the results of our calculations and build an ideal model of nanoceria in Section 5.5. Major results are summarized in the 5.6.

CHAPTER 2 THEORY

2.1 Density Functional formalism and Exchange Correlation Functional

Density Functional Theory (DFT) is one of the most widely used quantum chemical method for electronic structure calculations in solid-state physics. It is a well known approach to study ground state properties of many-body systems such as atoms, molecules, crystals and surfaces. Its applicability extends to the fields like biology and mineralogy. It is a versatile methodology to calculate energetics of complex systems due to the generality and flexibility of implemented fundamental concepts. DFT's framework is primarily build on Hohenberg-Kohn theorem¹ and Kohn-Sham equations.^{2,86} Although DFT is a first principle approach to solve Schrödinger wave equation. To describe DFT approach in general, we start with Born-Oppenheimer approximation where atomic nuclei are treated classically as fixed and the electrons are moving in their electric potential v . Thus a many electron Schrödinger equation can be written as:

$$\hat{H}\Psi = [\hat{T} + \hat{V} + \hat{U}]\Psi = \left[\sum_i^N -\frac{\hbar^2}{2m} \nabla_i^2 + \sum_i^N V(\vec{r}_i) + \sum_{i<j}^N U(\vec{r}_i, \vec{r}_j) \right] \Psi = E\Psi \quad (2-1)$$

Where \hat{H} is the Hamiltonian, \hat{U} is the electron-electron interaction energy, N is the number of electrons, \hat{T} is the kinetic energy, \hat{V} is the potential energy from the nucleian field, E is the total energy and Ψ represents the wave function of the system.

Density Functional Theory is mapping many body problem with \hat{U} onto a single body problem without \hat{U} , where key variable remaining is the particle density $n(\mathbf{r})$. According to Hohnberg-Kohn (HK) theorem, electronic density $n(\mathbf{r})$ determines all ground state properties of multi-electron system, where energy of the ground state is a functional of electronic density. The

HK equation describing ground state properties of many electron systems in terms of electron density is:

$$E[n(r)] = T[n] + V_{ext}[n] + V_{e-e}[n] = \int n(r)v_{ext}(r)dr + F_{HK}[n] \quad (2-2)$$

where Hohnberg-Kohn functional $F_{HK}[n] = T[n] + V_{e-e}[n]$. Although HK approach is in principle exact, the form of $F_{HK}[n]$ is unknown. The approximate form of kinetic energy functionial $T[n]$ is usually given by Kohn-Sham (KS) equations. KS equations mapped the real system into an auxiliary non-interacting reference system with the same density, where each electron moves in an effective 1-particle potential due to surrounding electrons. Kohn and Sham introduced the way to solve Schrödinger wave equation by giving relation between particle density and corresponding potential to finally calculate the kinetic energy of non-interacting N particle system. The Kohn-Sham equation:

$$\left[-\frac{1}{2}\nabla^2 + V_{eff}(r) \right] \phi_i = \epsilon_i \phi_i \quad (2-3)$$

where ϕ_i are KS orbitals, is the system of N effective one-particle equations, making up the total density $n(r) = \sum_i |\phi_i(r)|^2$.

There are several approximations for exchange-correlation functionals⁸⁷ in equation (2-2). In this form, Density functional theory (DFT)^{2,86} has become a method of choice for the calculation of numerous properties of molecules and solids. Unlike modern semiempirical methods such as MSINDO⁸⁸ and DFTB,⁸⁹ it does not require tedious empirical parameter fitting to produce acceptable results. Unlike WFT methods,⁹⁰ DFT accounts for electron-correlation not through increasing complexity of the wavefunction, but via approximate exchange-correlation functional.

The need to improve exchange–correlation functionals arises from known deficiencies of DFT describing so called strongly correlated systems where vacant and occupied electronic levels are approaching degeneracy (this effect is also known as static or non-dynamic electron correlation). This situation is observed in *d* and *f* electron systems or when chemical bonds are being stretched. Despite these limitations different exchange–correlation functionals are widely used for modeling of various systems. Early exchange–correlation functionals were dependent only on electron spin density (Local Spin Density Approximation, LSDA). Next generation of exchange–correlation functionals also included energy dependence on the gradient of the density (Generalized Gradient Approximation, GGA). Among the later developments are kinetic energy density dependent functionals which are also known as meta-GGA, including TPSS and BB95.^{91,92} GGA and meta-GGA functionals are called semilocal functionals to distinguish them from LDA on one hand, and non-local functionals including orbital dependence on the other hand. One of the meta-GGA functional we used in our study, TPSS⁹³ was designed to correct the too-large atomization energies and increase the too-small jellium surface energies obtained with LSD (Jellium is the term for model system of interacting electrons and a uniform background of positive charge). It had been shown to accurately predict bond energies and bond lengths in molecules, hydrogen-bonded complexes, and ionic solids.⁹⁴ Performance of TPSS approaches that of the hybrid PBE0 functional with a practical advantage of not including Hartree-Fock exchange.⁹³

2.2 Density Functional Theory + Hubbard U approach

The description and understanding of electronic properties of strongly correlated materials is a very important and long standing problem for ab initio calculations. Pure LDA and GGA is not always accurate enough for calculating sensitive property like spin state energetic and band gap of *d* and *f* metals. Anisimov and co-workers^{8,9,95} correct the standard functional adding an onsite Hubbard-like interaction to treat metal oxides. The method represents one of the simplest orbital dependent functionals in which a generalized Hubbard model is used to enforce localization of the electrons. Number of the first-principle approaches to estimate the U parameter had been proposed^{96,97} However, in many cases quantitatively better results can be obtained with the value of U determined empirically as a fitting parameter to experimental results^{98,99,100}. Anisimov described Hubbard-like interaction E_{Hub} .

$$E_{LDA+U}[\mathbf{n}(\mathbf{r})] = E_{LDA}[\mathbf{n}(\mathbf{r})] + E_{Hub}[\{\mathbf{n}_m^{l\sigma}\}] - E_{DC}[\{\mathbf{n}^{l\sigma}\}] \quad (2-4)$$

Where $\mathbf{n}(\mathbf{r})$ is the electron density and $\mathbf{n}_m^{l\sigma}$ are the atomic orbital occupations for the atom *I* experiencing the Hubbard term. The last term in the above equation is then subtracted in order to avoid double counting of the interactions contained both in E_{Hub} and, in some average way, in E_{LDA} . In this term the total, spin projected, occupation of the localized manifold is used

$$\mathbf{n}^{l\sigma} = \sum_m \mathbf{n}_m^{l\sigma} . \text{In}$$

2.3 Hybrid Density functional Theory

All LSDA, GGA and meta-GGA are known to underestimate band gaps in solids. On the other hand, Hartree Fock (HF) method yields an overestimated band gap. The electron correlation in DFT is introduced in terms of exchange-correlation functional E_{XC} , replacing exact exchange E_{HFX} in HF theory without increase in computational expense. Some empirical parameter fitting is typically involved in the design of the exchange-correlation functional in this formalism; it is largely system-independent. Although exact exchange is non-local and orbital-dependent, in DFT the functional E_{XC} is expressed in terms of the total electron density and its gradients (respectively local and semi-local approximation). Unlike exact exchange, E_{XC} includes repulsion of electron from its own density and does not vanish for one-electron systems. This property is known as self-interaction error, and it has both negative and positive effects. As negative result, in DFT bonds are too weak, while electrons are over-delocalized and do not interact with Coulomb asymptotic $\sim 1/r$ at large separations. On a positive side, self interaction is mimicking non-local part of electron correlation and should be retained to some degree. Practically useful step in balancing self-interaction error was made by Becke,¹⁰¹ who suggested to include a fraction of HF exchange energy in E_{XC} functional:

$$E_{XC} = aE_{HFX} + (1-a)E_{DFX} + E_C \quad (2-5)$$

where $a=0.2$ is an empirical parameter, E_{DFX} and E_C are exchange and correlation functionals including local and semi-local terms. The original (B3LYP)¹⁰¹ as well as more recent hybrid functionals often achieve chemical accuracy in properties predictions.^{102,103,104} We used BMK

(Boese-Martin for kinetics) a hybrid meta-GGA functional with 42% of HF exchange, and PBE1PBE functional with 25% exchange functional for calculation of cerium oxides.

CHAPTER 3 TRANSITION METAL OXIDES

3.1 Solid Oxide Fuel Cell and Properties of Cathode material

Recent worldwide interest in cleaner energy technology has refocused attention to the solid oxide fuel cells (SOFC) as a potential source of efficient, environmentally friendly, and fuel versatile electric power. Because of high operating temperatures, the SOFCs offer several potential advantages over proton exchange membranes fuel cells including low internal resistance, high tolerance to catalyst poisons, production of high-quality waste heat for reformation of hydrocarbon fuels, as well as the possibility of oxidation of hydrocarbon fuels directly. SOFC's efficiency ranges from 50 to 65% and they can be used as environmentally acceptable source of electric energy.^{105,106}

Continuous effort in the design of SOFC multicell stacks and systems requires deeper understanding of the structure/property-performance relationships. Numerous attempts had been made to explore new electrode materials and microstructures, and establish how and why electrode performance changes with time, temperature, thermal cycling, operating conditions, impurities, and other factors.^{105,106} Despite the advances in electrochemical measurement and modeling, understanding of SOFC cathode oxygen reduction and transport mechanisms remains largely circumstantial today. The elucidation of the cathode mechanisms often relies on having limited understanding for an observed phenomenon (e.g. chemical capacitance as evidence for bulk transport) rather than direct independent measurements.¹⁰⁶ Therefore, direct experimental observations (such as spectroscopic evidence of oxidation/reduction of the electrode material) are critically important to achieve further progress in SOFC design. Experimental

characterization techniques may not, however, always be available to determine certain properties and atomistic structure of the materials. In those cases, the computational investigation of the representative supercells from the first principles can greatly assist in completing the picture and achieve deeper understanding of the relevant processes. Such combined experimental and theoretical investigation has an added value and contributes to the design of more efficient and cost-effective devices.

The SOFC is built using porous solid ceramic cathode, anode, and dense electrolyte. The cathode is required to be stable in an oxidizing atmosphere, be electronically conductive, and maintain a porous structure at high operating temperatures. It is also beneficial for the cathode material to exhibit oxygen ion conductivity. To be a good oxygen ion conductor, a ceramic cathode should satisfy two fundamental requirements: (i) it has to contain a significant amount of vacancies in the oxygen sublattice, and (ii) the energy barriers for site to site oxygen migration need to be fairly small (3). Mixed ionic-electronic conducting transition metal perovskite type oxides are considered materials of choice for SOFC cathodes because of their porosity and good electrical conductivity.

3.2 Mixed Perovskite and BSCF as cathode material

Mixed oxides with the general formula ABO_3 crystallize in perovskite structure, where A cations are either lanthanides or alkaline earth metals, and B cations are transition metals such as Mn, Fe, or Co. These perovskites often have large mobility of the oxygen vacancies, exhibit strong ionic conductivity, and are often used as cathode materials in SOFC.¹⁰⁵ The first studies of the mixed perovskite compounds were focused on lanthanum strontium cobaltite (LSC) with the formula $La_{1-x}Sr_xCoO_{3-\delta}$.¹⁰⁷ The high oxygen permeation flux in LSC was attributed to the

high concentration of vacancy in the anion sublattice due to the substitution of La^{3+} by Sr^{2+} at the A-site of the perovskite.¹⁰⁸ Unfortunately, at oxygen partial pressures <10 kPa and temperatures below 790 °C, LSC is unstable and phase transition to vacancy-ordered brownmillerite structure takes place. Burggraaf *et al.* examined oxygen permeability of perovskite-type oxides $\text{SrCo}_{0.8}\text{B}_{0.2}\text{O}_{3-\delta}$ ($\text{B} = \text{Cr}, \text{Fe}, \text{Co}, \text{and Cu}$) and $\text{La}_{0.6}\text{Sr}_{0.4}\text{CoO}_{3-\delta}$.¹⁰⁹ They found a 5 orders of magnitude increase in oxygen permeability (up to $0.3\text{--}3 \times 10^{-7} \text{ mol cm}^{-2}\text{s}^{-1}$) at the onset of the transition from a low-temperature vacancy-ordered state to defective perovskite for all compounds except $\text{SrCo}_{0.8}\text{Fe}_{0.2}\text{O}_{3-\delta}$. In the latter case, only a slight anomaly was found for the oxygen permeability. The comparatively high oxygen flux through $\text{SrCo}_{0.8}\text{Fe}_{0.2}\text{O}_{3-\delta}$ observed at intermediate temperatures was interpreted in terms of a two-phase mixture of a vacancy-ordered state and disordered perovskite, whereas above 790 °C, the sample is single-phase of defective perovskite structure.¹⁰⁹ Kharton *et al.* measured oxygen permeation fluxes in $\text{SrCo}_{0.8}\text{M}_{0.2}\text{O}_3$ ($\text{M} = \text{Cr}, \text{Mn}, \text{Ni}, \text{Cu}, \text{Ti}$) materials using the electrochemical method.^{110,111} The highest permeation flux was found for the strontium cobaltite-ferrite (SCF) perovskite with composition of $\text{SrCo}_{0.8}\text{Fe}_{0.2}\text{O}_3$. The substitution of Sr^{2+} ions in SCF by ions with higher charge such as La^{3+} usually increases phase stability, whereas the oxygen permeability is simultaneously decreasing.^{112,113} Recently, a new solution to this permeability decrease was suggested. It consists of partial substitution of Sr^{2+} with Ba^{2+} in SCF. The resulting material, called barium–strontium cobaltite–ferrate (BSCF) has improved phase stability, whereas the oxygen permeation flux remains unchanged. Initially, BSCF was developed as a high-temperature oxygen permeation membrane material.^{108,114} Recently Shao *et al.* proposed BSCF as an intermediate temperature cathode material.¹¹⁵ The reason of phase stability of BSCF is suggested

by McIntosh *et al.*¹¹⁶ According to their explanation, the Ba²⁺ ion is too large to sustain the transition-metal brownmillerite structure.

The size and charge of the B-site cations are found to be even more important parameters for the conductivity in perovskites. The B–O octahedra constitute the framework of the perovskite structure, and the oxide anion interacts with the B cation by a much stronger partially covalent bond, unlike the purely ionic bond to the large A cation. Lybye⁶⁷ compared four perovskites, La_{0.9}Sr_{0.1}B_{0.9}Mg_{0.1}O_{2.9} (B = Al³⁺, Ga³⁺, Sc³⁺, or In³⁺) where only the B ion is changed, and found the maximum ionic conductivity for B = Ga³⁺. This trend which could not be rationalized using the lattice free volume and the critical ionic radius point (proposed by Sammells *et al.*¹¹⁷) or by Goldschmidt factor points. Mogensen¹¹⁸ rationalized the observed trend using the concept of the lattice stresses: a stress-free lattice will give the maximum oxide ion conductivity. The importance of the nature of the B-site ion is further evidenced by the results published on the rare earth gallates. Ishihara *et al.*¹¹⁹ reported that substituting half of the Mg²⁺ in La_{0.8}Sr_{0.2}Ga_{0.8}Mg_{0.2}O_{2.8} with Co or Ni ions improves the oxide ionic conductivity significantly. Another reason for improving ionic conductivity by different B-site cations is the change in concentration of the oxygen defects, tuned by substituting B-site cations with more or less reducible ones, or by substituting A-site cations with cations of a different charge.¹²⁰ In this paper, we report results of X-ray diffraction analysis, transmission electron microscopy, micro-Raman spectroscopy study, and density functional theory (DFT) calculations of structural and electronic properties of BSCF, including the spin states of B cations. Special attention is paid to the oxygen vacancies and cation ordering to clarify the stability of this material. Theoretical results are compared with experimental data.

3.3 Computational Details

Our calculations are based on Density Functional Theory (DFT) with the Perdew-Burke-Ernzerhof (PBE) exchange-correlation functional, Vanderbilt ultrasoft pseudopotentials¹²¹ and the plane wave basis set implemented in the Quantum-ESPRESSO program package.¹²² The Brillouin-zone integrations are performed using Monkhorst-Pack grids with a $2 \times 2 \times 2$ mesh for supercell calculations. Spin polarized DFT with Marzari-Vanderbilt smearing¹²³ is used throughout. Geometry optimizations used the Broyden-Fletcher-Goldfarb-Shanno algorithm. The wave function and electron density representation are limited by kinetic energies of 40 and 360 Rydberg respectively. We treated the Ba($5s, 5p, 6s$), Sr($4s, 4p, 5s$), Co($4s, 3d$), Fe($3d, 4s$) and O($2s, 2p$) electrons as valence states, while the remaining electrons were represented by pseudopotentials. These pseudopotentials were validated by computing the equilibrium lattice parameters (a) and bulk moduli (B) and comparing their values with the experimental ones (see Results and Discussion section). For Co^{4+} we found an intermediate spin state to be the most stable among three possible spin states: low spin (LS), intermediate spin (IS), and high spin (HS) states (spin of $S=1/2$, $S=3/2$, and $S=5/2$ respectively).¹²⁴ For Fe^{4+} cations HS is the more stable of LS and HS states ($S=1$ and $S=2$).¹²⁴

For the mixed perovskite material $\text{Ba}_{0.5}\text{Sr}_{0.5}\text{Fe}_{0.2}\text{Co}_{0.8}\text{O}_3$ we used a $2 \times 2 \times 2$ supercell, containing 4 Ba atoms, 4 Sr atoms, 2 Fe atoms and 6 Co atoms, along with 24 oxygen atoms (Figure 3-6). This amounts to a $\text{Ba}_{0.5}\text{Sr}_{0.5}\text{Fe}_{0.25}\text{Co}_{0.75}\text{O}_3$ formula unit, which is fairly close to the experimentally observed stoichiometry. Figure 3-2 shows the ion numbering scheme used in the following discussion.

Activation energies for oxygen migration were obtained starting from different ion distributions in the supercell. For each ion distribution we performed three structural relaxation calculations: two for the stable supercell with one vacancy before and after migration, and one transition state with an oxygen ion in the middle of the XYX plane with OYZ angle of 45° . In the transition states found, the oxygen ion was located away from the straight line connecting the oxygen positions before and after the migration. That means the migration pathway is curved shows in Figure 1-3, in agreement with previously published results obtained using the empirical force fields.^{28,29} While geometry relaxation of the symmetric transition barriers can be accomplished by simply constraining the angle at 45° , the asymmetric transition barrier search requires use of special algorithms. The Nudged Elastic Band (NEB)¹²⁵ method is one of them. It enables one to find the optimal transition state and minimal energy reaction pathway when both the initial and final states are known. Seven replicas are chosen including the initial and final ones to construct the elastic band in this method. Here we used NEB method¹²⁵ with 7 images. This type of calculations increased CPU time by the factor of 20 compared to the regular relaxation, but allows one to obtain complete trajectory of the oxygen migration.

For all investigated stable ionic configurations Boltzmann factors were calculated to estimate the probability to observe this local structure at a sample preparation temperature of 1150°C . Boltzmann factors correspond to the probability for each local structure occurring in the sample, assuming it was cooled down fast after the preparation. Annealing at lower temperatures is expected to increase the frequency for the more stable configurations and decrease the frequency for the less stable ones, whereas the relative energy order of the configurations will

remain the same. In order to identify the spin state of each cation in the supercell containing different types of ions, we used Löwdin population analysis of the spin density.

3.4 Electronic structure of BSCF

In octahedral crystal field Co^{4+} can have three possible spin states, $t_{2g}^5 e_g^0$ ($S = 1/2$), $t_{2g}^4 e_g^1$ ($S = 3/2$), and $t_{2g}^3 e_g^2$ ($S = 5/2$) with one, three and five unpaired electrons, respectively. Fe^{4+} can have two possible spin states in the octahedral splitting with two and four unpaired electrons. These states have configurations as $t_{2g}^4 e_g^0$ ($S = 1$) and $t_{2g}^3 e_g^1$ ($S = 2$). We denote these states as low spin (LS) with one unpaired electron, intermediate spin (IS) with three unpaired electrons, and high spin (HS) states with five unpaired electrons for Co^{4+} , and as LS and HS states for Fe^{4+} cation according to their multiplicity. The spin-state configurations of Co^{4+} and Fe^{4+} in octahedral crystal field are schematically shown in Figure 3-1.

The accuracy of used pseudopotentials was validated by computing the equilibrium lattice parameter (a) for pure perovskites SrCoO_3 , SrFeO_3 , BaTiO_3 , and SrTiO_3 . For last two perovskites bulk moduli (B) were also calculated and compared with experimental values in Table 3-1. The bulk moduli were obtained by fitting the energy-volume curves using the Birch–Murnaghan equation of states.¹²⁶ All calculations for the pure perovskites were performed using a unit cell containing a single formula unit. For modeling the mixed perovskite $\text{Ba}_{0.5}\text{Sr}_{0.5}\text{Fe}_{0.2}\text{Co}_{0.8}\text{O}_3$, we used a $2 \times 2 \times 2$ supercell. One supercell has 4 Ba atoms, 4 Sr atoms, 2 Fe atoms, and 6 Co atoms, which results in a $\text{Ba}_{0.5}\text{Sr}_{0.5}\text{Fe}_{0.25}\text{Co}_{0.75}\text{O}_3$ formula unit, fairly close to the experimentally observed stoichiometry. For all investigated configurations, we calculated the Boltzmann factors at the temperature of sample preparation (1150 °C). These factors correspond to the frequency for each local structure occurring in the sample, assuming it was cooled down

fast after the preparation. Annealing at lower temperatures is expected to increase the frequency for the more stable configurations and decrease the frequency for the less stable ones, whereas the relative order will remain the same.

The single phase BSCF perovskite was refined in cubic $Pm3m$ space group symmetry with a lattice constant $a = 4.00013(8)$ Å. No secondary phases have been detected. The morphology and particle size of the BSCF are presented in Figure 3-5. As one can see, the powder particles have an irregular shape with a particle size of $d_{50} = 0.35$ μm. The chemical analysis using energy-dispersive spectrometer has shown the presence of Ba, Sr, Co, and Fe as well as oxygen atoms in the appropriate stoichiometry. Our observations are in agreement with the literature data. In a recent study on BSCF, the cubic phase was found to reversibly transform to a hexagonal polymorph upon long-term annealing at 900 °C.¹²⁷ The phase stability of the cubic BSCF at higher temperature is confirmed by Yang *et al.*¹²⁸ According to their study, at 1000 °C, most of the compositions maintain the cubic phase.

In the ideal cubic perovskite structure, all lattice sites have inversion symmetry. Therefore, first-order Raman scattering is forbidden and no Raman active band is expected to be found in cubic BSCF perovskite.¹²⁹ However, the broad band is detected at ~ 675 cm⁻¹, as is shown in Figure 3-4. This broad peak consists of the two overlapping bands which parameters, such as peak positions and intensities could be detected using the full width at half-maximum (FWHM) approach. The appearance of these vibration bands, forbidden in cubic structure, could be explained by the Jahn–Teller distortion in BSCF perovskite at room temperature. We associate this dynamic, local site distortion around the Co⁴⁺ cation with its intermediate spin state $t_{2g}^5 e_g^1$. The presence of a single electron on the degenerate energy level results in distortion of

the octahedral coordination of this cation by the first-order Jahn–Teller mechanism. The rising temperature will result in dynamic disorder, and average out the Jahn–Teller distortion. Thus, the intensities of the bands are expected to decrease, and the peaks become indistinguishable from the background. Therefore, the experimentally observed decrease in the intensities of two broad peaks at 600 °C reflects the transition to a dynamically less distorted local structure of BSCF.

In the case of the ordering of two different B-site cations in cubic perovskites a face-centered cubic superstructure with $Fm3m$ symmetry is created (called elpasolite-type structure). This leads to several normal modes active in Raman spectra. Their wavenumbers were shown to change with temperature, whereas their intensities do not depend on the temperature significantly.¹³⁰ Unlike the B-cation ordering, the Jahn–Teller distortion results in a strong temperature dependence of the Raman intensities, which was reported, for instance, in our previous study of LaCoO_3 ,¹³¹ as well as other studies of this perovskite.¹³²

The comparisons of calculated and experimental values of lattice parameters and bulk modulus of pure perovskites are presented in Table 3-1. In agreement with experimental data,¹³³ our calculations result in IS state of the cobalt ion for the ground state of SrCoO_3 . For this compound, our calculations also demonstrate a close agreement with the experimental value of the lattice parameter¹³⁴ (the deviation is +0.2% for LS state, and –0.6% for IS state, whereas the deviation is as large as 3.3% for HS state). The IS state of Co^{3+} was experimentally observed with photoemission spectra¹³⁵ and the ferromagnetic resonance measurements.¹³⁶ The experimental value for magnetic moment of strontium cobaltite SrCoO_3 is 2.1 μ_B . This value of magnetic moment is bracketed by idealized magnetic moments of HS and LS states.¹³⁷ Our

calculations give the total energies for LS and HS states to be 7.46 and 22.48 kcal/mol above the IS state.

In the case of SrFeO₃ compound, we found the HS state to be more stable by 9.60 kcal/mol compared to LS state, which is also consistent with experiment.¹³⁵ The calculated lattice parameter for both LS and HS states deviates from the experimental value¹³⁸ by -0.2 and -1.3%, respectively. From the Table 3-1, we can conclude that the ground electronic spin state of Co³⁺ in SrCoO₃ is IS, whereas Fe in SrFeO₃ has HS ground state.

For the model BSCF supercell, we performed optimization of the lattice parameter corresponding to the ambient zero pressure. Experiments show,¹⁰⁸ that the oxygen sublattice of BSCF in nonstoichiometric and molar fraction of the oxygen vacancies is $\delta = 0.38$ at 1150 °C. To address this fact, we studied the relative stability of the oxygen deficient supercells with respect to various vacancy positions. Structures with up to 4 oxygen vacancies per supercell were considered. They correspond to the formula Ba_{0.5}Sr_{0.5}Co_{0.8}Fe_{0.2}O_{3- δ} with $\delta = 0.125, 0.25, 0.375,$ and 0.5. The calculated lattice parameter was found to be within 0.3% from the experimental lattice parameter of BSCF for all concentrations of vacancies. This result is in agreement with the neutron diffraction study performed by McIntosh *et.al.*¹²⁰

To determine the spin state of the supercell, two spin states for Fe ($s = 1$ and $s = 2$) were combined with three spin states for Co⁴⁺ ($s = 1/2, s = 3/2,$ and $s = 5/2$). According to experimental data, the SrFe_{1-x}Co_xO₃ compound is antiferromagnetic for $x < 0.10-0.15$ and becomes ferromagnetic for $x \geq 0.2$.¹³⁹ The ferromagnetic state of SrFeO₃ was also found to be the most stable at LSDA+U level of theory.¹⁴⁰ On the basis of these data, we considered Fe and Co cations in BSCF supercell to be ferromagnetically coupled.

The spin state of the transition metal ions in BSFC was examined by Löwdin population analysis. The results of this analysis for SrCoO₃ and SrFeO₃ perovskite structures at different spin states reveal ferromagnetic coupling between transition metal cations. Herein we tested all the examined structures by Löwdin population analysis in order to verify the spin states of individual cations and their ferromagnetic ordering in structures under investigation.

To determine the most stable spin state of the stoichiometric BSCF, we combined one of the two possible spin states for Fe⁴⁺ cation with one of the three spin states for Co⁴⁺. Our calculated results are presented in Table 3-2 and demonstrate that the ground state of the BSCF supercell without defects is formed by IS state of Co⁴⁺ and HS state of Fe⁴⁺. This is the most stable state with Boltzmann factor of 98%. For this ground state, the structural relaxation of the supercell converges to the structure with tetragonal distortion around the Co⁴⁺ cation, shown in Figure 3-3. This result is in agreement with the experimentally observed Jahn–Teller lattice distortion of BSCF, discussed above. Because both elongation and contraction of Co–O interionic distances are observed in simultaneous fashion, overall symmetry of the structure remains cubic as shown in Figure 3-3. This theoretical conclusion is reinforced by experimental Raman spectroscopy data shown in Figure 3-4, where the decrease of the intensity of a broad peak ~675 cm⁻¹ occurs at elevated temperatures and complete disappearance of the peak is expected as temperature rises further. The existence of IS state of Co³⁺ ion is also observed experimentally in different lanthanum-based cobaltites.^{71,131,140}

Table 3-1: Lattice parameters a (Å) and bulk moduli B (GPa) calculated for some pure and mixed perovskites. Two different spin states of Co^{+4} , and oxygen vacancy in BSCF are also reported. BSCF calculations are preformed for 2x2x2 supercell, then devided by 2. The experimental unit cell parameters and bulk moduli are shown for comparison.

| Compound | Co Multiplicity | a , Å | | B , GPa | |
|---|-----------------|---------|--------------------|-----------|------------------|
| | | calc | exp | calc | Exp |
| SrCoO ₃ | 4 | 3.825 | 3.835 ^d | | |
| | 6 | 3.857 | | | |
| SrFeO ₃ | - | 3.889 | 3.835 ^c | | |
| BaTiO ₃ | - | 3.989 | 4.000 ^e | 148.34 | 135 ^a |
| SrTiO ₃ | - | 3.930 | 3.899 ^f | 181.57 | 179 ^b |
| Ba _{0.5} Sr _{0.5} Fe _{0.25} Co _{0.75} O ₃ | 4 | 3.900 | | | |
| Ba _{0.5} Sr _{0.5} Fe _{0.25} Co _{0.75} O _{3-δ} ($\delta = 0.125$) | 4 | 3.905 | | | |
| Ba _{0.5} Sr _{0.5} Fe _{0.25} Co _{0.75} O ₃ | 6 | 3.968 | | | |

a) Ref. ¹³⁴, b) Ref. ¹⁴¹, c) Ref. ¹⁴², d) Ref. ¹³⁷, e) Ref. ¹⁴³, f) Ref. ¹⁴⁴

Table 3-2: Spin densities on transition metal cations, set up as initial guess and obtained with Lowdin population analysis at SCF convergence for BSCF 2x2x2 supercell, their relative energies and Boltzmann factors.

| Unit cell Multiplicity | SCF solution spin-polarization | | ΔE kJ/mol | Boltzmann factor (%) |
|---------------------------|-----------------------------------|------|----------------------|-------------------------|
| | Fe | Co | | |
| 23 | 2.79 | 1.69 | 40.4 | 2 |
| 27 | 2.80 | 1.98 | 0.0 | 98 |
| 35 | 3.33 | 2.55 | 147.5 | 0 |
| 39 | 3.55 | 2.79 | 424.4 | 0 |

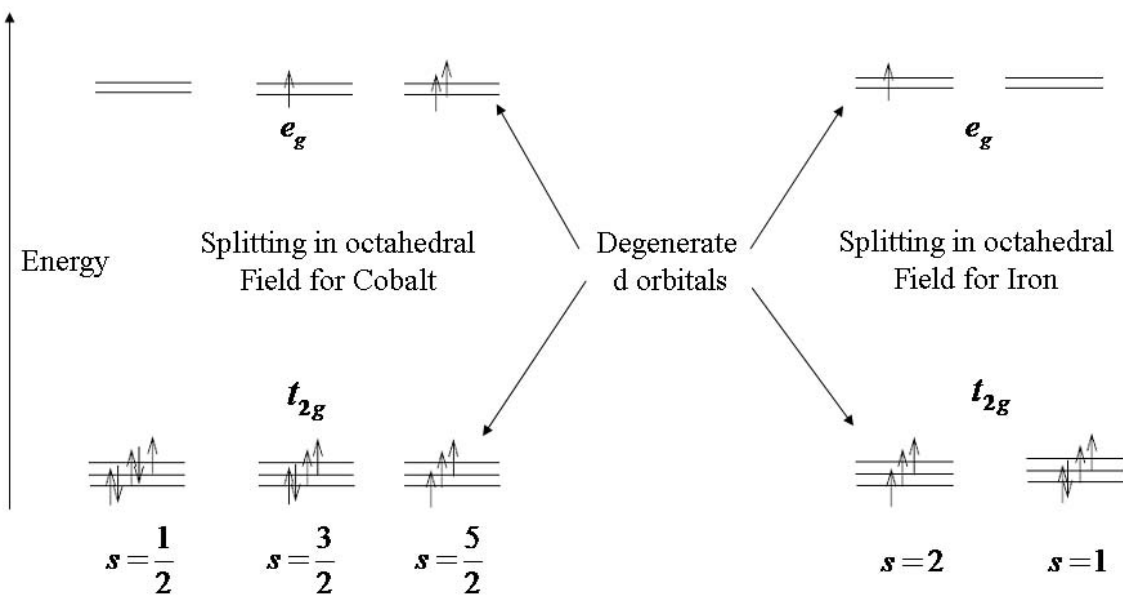


Figure 3-1: Different possible spin states of Fe^{+4} and Co^{+4} in octahedral crystal field.

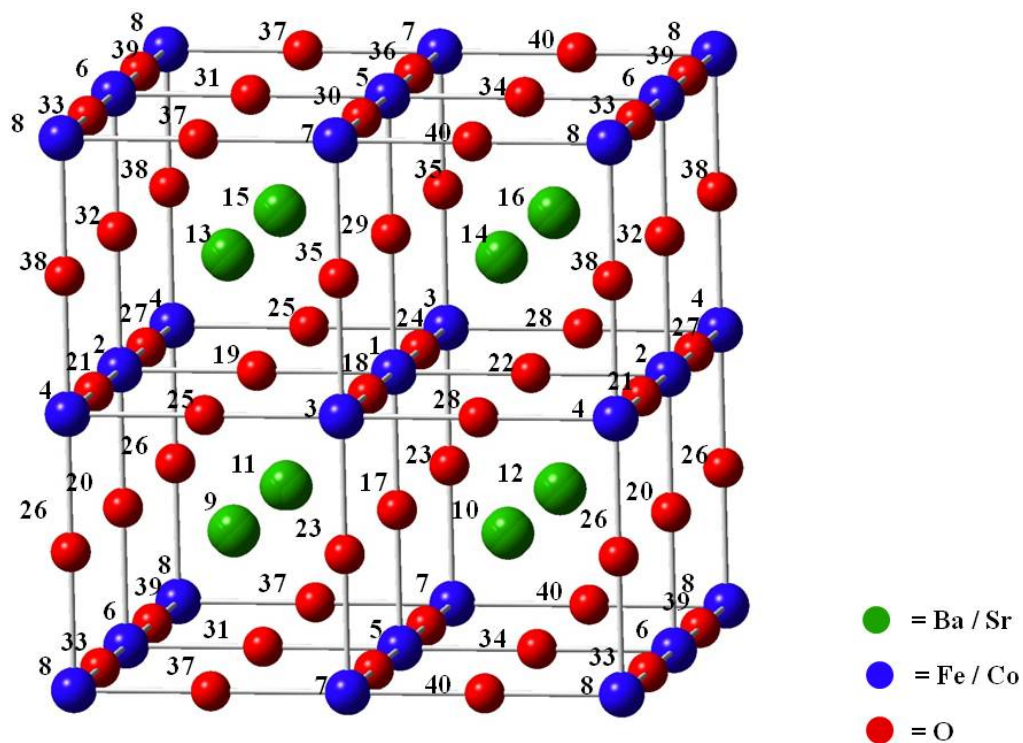


Figure 3-2: ABO₃ perovskite supercell used for calculation. Here A is barium or strontium (marked by indexes 9-16), B is iron or cobalt (marked by indexes 1-8), and the rest are oxygen atoms (marked by indexes 17-40).

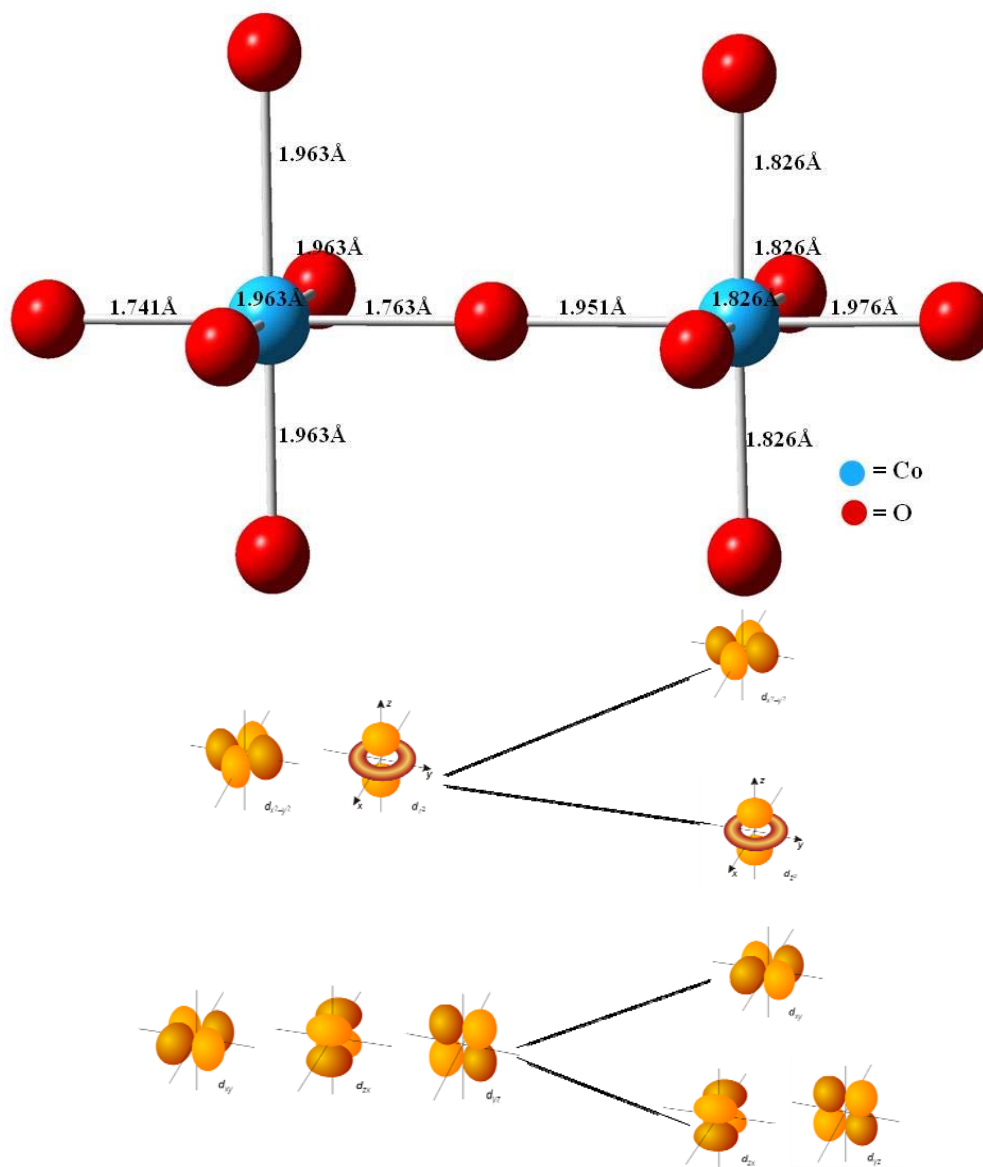


Figure 3-3: Jahn-Teller distortion of the coordination octahedron around the Co^{4+} cation is the consequence of the intermediate spin state in the BSCF supercell. Calculated equilibrium distances between Co^{4+} and nearest oxygen ions are shown.

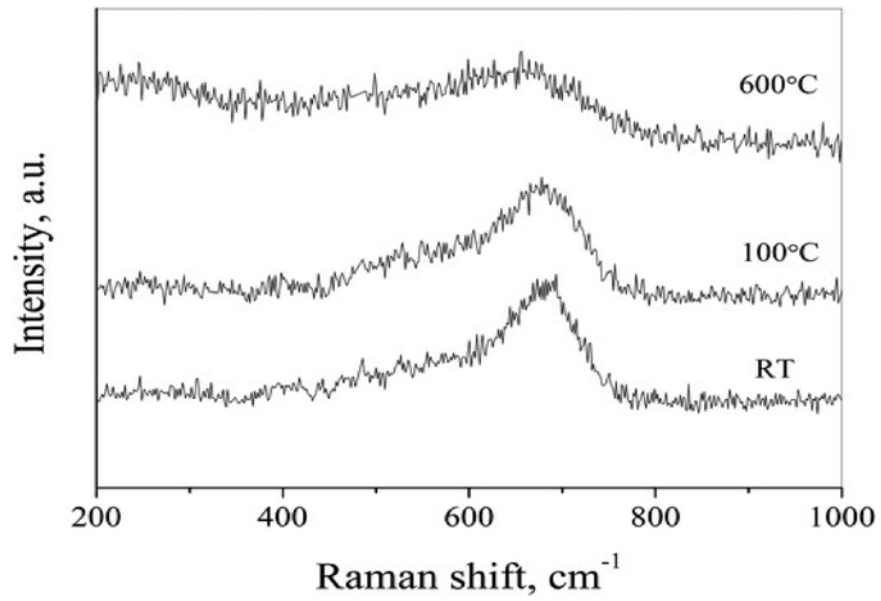


Figure 3-4: Raman spectra of BSCF indicates intensity decrease and broadening of $\sim 675 \text{ cm}^{-1}$ peak with elevated temperature

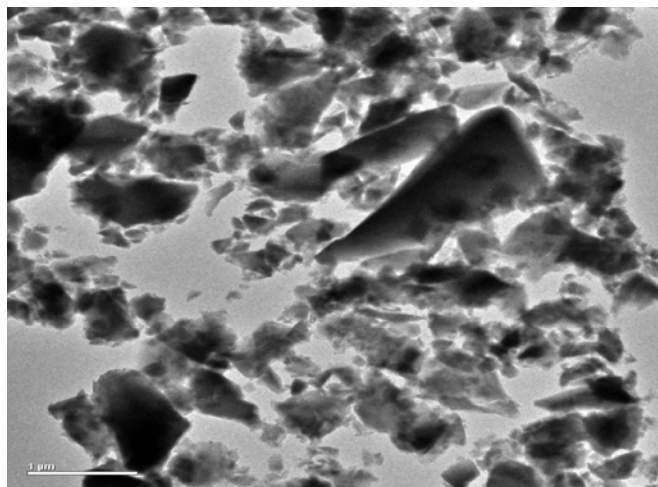


Figure 3-5: TEM micrograph showing a particle size and morphology of BSCF perovskite powder

3.5 Oxygen vacancy and cubic phase stability of BSCF

The model supercell without vacancies can have nine symmetrically inequivalent arrangements of Fe^{4+} and Co^{4+} cations at the B positions as well as Ba^{+2} and Sr^{+2} cations in A positions. The relative stability for all these structures are listed in Table 3-3, where the relative positions of cations are labeled according to Figure 3-4. From the Boltzmann factor in the last column in Table 3-3 one can clearly see that there is no preferred cation arrangement. Thus, we conclude that the transition metal cations fill their positions almost randomly.

The second step was repeated for configurations with two and more oxygen vacancies. We observe that in the most stable configuration two vacancies are located in cis-position to the same B cation, while the third vacancy is preferentially located in cis-position to the second one at the other B cation at an angle to the first vacancy (L-shape vacancy ordering). Similarly, four vacancies prefer to form a square (with Boltzman factor of 47%), rather than the linear arrangement (with Boltzman factor of 9%). We reported more details on the vacancy ordering in our previous paper.¹²⁴ These results are in agreement with the experimental fact that the BSCF structure remains cubic in the observed oxygen deficiency range. A similar compound, SCF, which contains Sr instead of Ba ions, demonstrates a linear vacancy ordering and undergoes a phase transition into a brownmillerite structure at lower temperatures.¹¹⁶ In the supercell with 2, 3, and 4 oxygen vacancies, the transition metal cations adjacent to the vacancy change their coordination from the ideal octahedron with two missing vertices into the distorted tetrahedron after the geometry is relaxed, as illustrated on Figure 3-7.

All three different oxygen vacancy concentrations mentioned above were examined. On the first step of the simulation we varied different ionic positions in the defect free supercell. On

the second step we randomly removed one oxygen atom from the most stable stoichiometric configuration and calculated relative energy of oxygen vacant supercells. The results are collected in the Table 3-4. As one can see, the first vacancy prefers to stay between Fe and Co (or two Co ions), while the second vacancy favors the coordination octahedron of the Co atom neighboring the first vacancy. The third vacancy favors the other coordination octahedron, involved in the first vacancy. There it has two preferred positions: in cis-position to the second vacancy (L-shaped vacancy trimer), or in trans-position to it (linear vacancy trimer). The vacancy ordering into the linear chains is observed during phase transition from disordered cubic perovskites to the Brownmillerite phases of $ABO_{2.5}$ stoichiometry. In our calculations, the L shaped vacancy trimer was found to be more stable than the linear vacancy with significantly higher Boltzmann factor, shown in the last column of Table 3-4. The four vacancy positions obtained after removing the fourth oxygen atoms are shown in Figure 3-5. The most stable vacancy tetramer configuration is a square. Thus, our calculations found the linear vacancy ordering to be unfavorable compared to the tetrameric islands of vacancies. This is in agreement with the experimental fact that the BSCF structure remains cubic in the observed oxygen deficiency range whereas the similar Ba-free compound forms brownmillerite structure with linear vacancy ordering.¹¹⁶ The formation 2, 3, and 4 oxygen vacancies in BSCF supercell changes the coordination of two, three, or four transition metal cations, adjacent to the vacancy. Formation of square vacancy tetramer changes the ideal octahedron coordination of four transition metal ions into the distorted tetrahedron. Its relaxed geometry is shown in Figure 3-7.

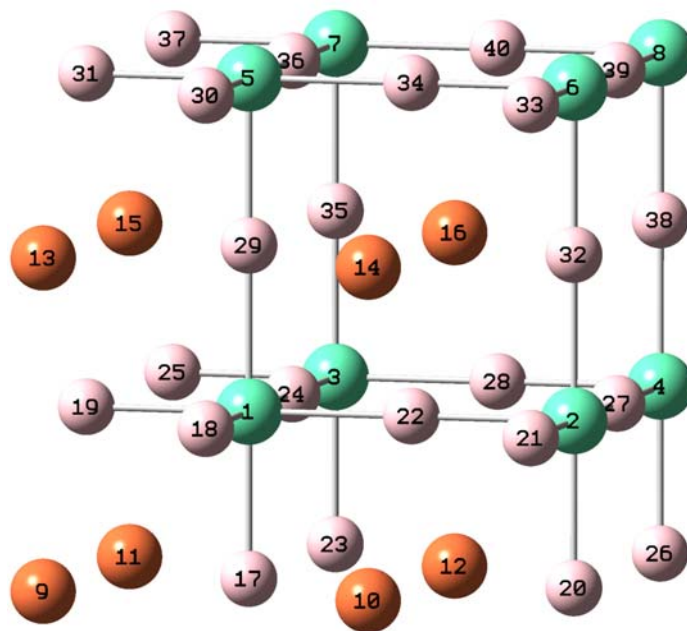


Figure 3-6: ABO_3 perovskite supercell used for calculation. Sites B (Iron or Cobalt cations) represented using indexes 1-8, sites A (Barium or Strontium cations) represented using indexes 9-16, while indexes 17-40 represent Oxygen ions.

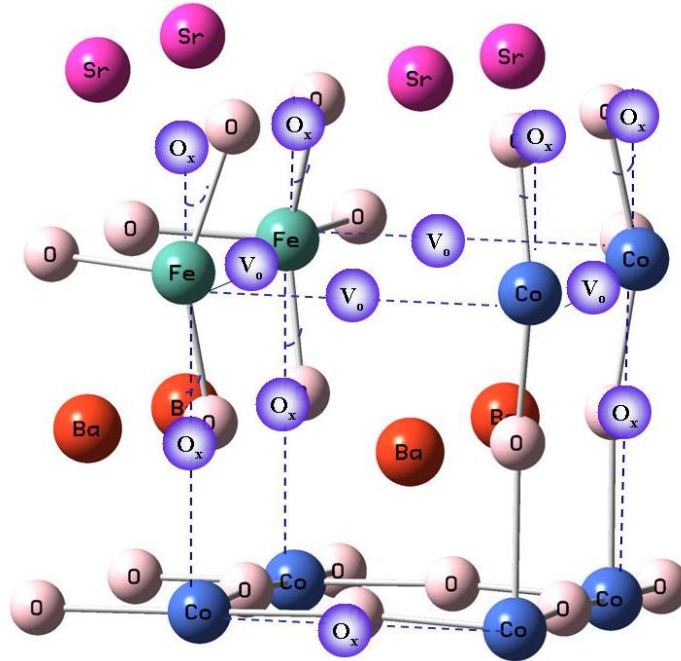


Figure 3-7: $\text{Ba}_{0.5}\text{Sr}_{0.5}\text{Co}_{0.8}\text{Fe}_{0.2}\text{O}_{2.5}$ supercell ground state structure. Four oxygen vacancies are denoted as V_o . The positions of oxygen atoms in the initial vacancy free lattice are labeled as O_x to demonstrate oxygen atoms displacement accompanying the oxygen vacancies formation

Table 3-3: Relative ground state energies of BSCF supercell with respect to different cation positions. The index for cations indicates the positions according to Figure 3-6, and spin states are $s=2$ (Fe), $s=3/2$ (Co). ΔE is the relative ground state energy measured in kcal/mol, C indicates the Boltzmann factors at 1150C.

| Fe1 | Fe2 | Co1 | Co2 | Co3 | Co4 | Co5 | Co6 | Ba1 | Ba2 | Ba3 | Ba4 | Sr1 | Sr2 | Sr3 | Sr4 | ΔE | C |
|-----|-----|-----|-----|-----|-----|-----|-----|-----|-----|-----|-----|-----|-----|-----|-----|------------|----|
| 1 | 5 | 2 | 3 | 4 | 6 | 7 | 8 | 10 | 11 | 13 | 16 | 9 | 12 | 14 | 15 | 2.03 | 8 |
| 1 | 6 | 2 | 3 | 4 | 5 | 7 | 8 | 10 | 11 | 13 | 16 | 9 | 12 | 14 | 15 | 2.01 | 8 |
| 1 | 8 | 2 | 3 | 4 | 5 | 6 | 7 | 10 | 11 | 13 | 16 | 9 | 12 | 14 | 15 | 2.54 | 6 |
| 1 | 5 | 2 | 3 | 4 | 6 | 7 | 8 | 10 | 12 | 14 | 16 | 9 | 11 | 13 | 15 | 0.00 | 18 |
| 1 | 6 | 2 | 3 | 4 | 5 | 7 | 8 | 10 | 12 | 14 | 16 | 9 | 11 | 13 | 15 | 0.10 | 18 |
| 1 | 8 | 2 | 3 | 4 | 5 | 6 | 7 | 10 | 12 | 14 | 16 | 9 | 11 | 13 | 15 | 0.76 | 13 |
| 1 | 5 | 2 | 3 | 4 | 6 | 7 | 8 | 11 | 12 | 13 | 14 | 9 | 10 | 15 | 16 | 1.42 | 10 |
| 1 | 6 | 2 | 3 | 4 | 5 | 7 | 8 | 11 | 12 | 13 | 14 | 9 | 10 | 15 | 16 | 1.41 | 10 |
| 1 | 8 | 2 | 3 | 4 | 5 | 6 | 7 | 11 | 12 | 13 | 14 | 9 | 10 | 15 | 16 | 1.95 | 8 |

Table 3-4. Relative ground state energies ΔE (kcal/mol) of 1, 2, 3, and 4-oxygen deficient $\text{Ba}_{0.5}\text{Sr}_{0.5}\text{Co}_{0.8}\text{Fe}_{0.2}\text{O}_{3-\delta}$ supercells with respect to different vacancy positions (denoted according to Figure 3-6). The positions of cations are: Fe=1,5; Co=2,3,4,6,7,8; Ba=10,12,14,16; Sr=9,11,13,15 (see Figure 3-6).

| V ₁ | V ₂ | V ₃ | V ₄ | ΔE (kcal/mol) | C (%) at 1150 ⁰ C |
|----------------|----------------|----------------|----------------|-----------------------|------------------------------|
| 29 | | | | 6.24 | 7 |
| 24 | | | | 0 | 67 |
| 35 | | | | 3.13 | 21 |
| 22 | | | | 11.06 | 1 |
| 27 | | | | 7.92 | 4 |
| 24 | 18 | | | 19.47 | 0 |
| 24 | 22 | | | 7.72 | 3 |
| 24 | 28 | | | 4.88 | 9 |
| 24 | 29 | | | 3.15 | 17 |
| 24 | 32 | | | 6.08 | 6 |
| 24 | 34 | | | 11.30 | 1 |
| 24 | 35 | | | 0.00 | 54 |
| 24 | 36 | | | 9.81 | 2 |
| 24 | 38 | | | 6.49 | 5 |
| 24 | 39 | | | 10.39 | 1 |
| 24 | 40 | | | 10.47 | 1 |
| 24 | 35 | 17 | | 10.07 | 2 |
| 24 | 35 | 23 | | 5.02 | 11 |
| 24 | 35 | 33 | | 11.16 | 1 |
| 23 | 24 | 29 | | 3.88 | 17 |
| 23 | 24 | 36 | | 0.00 | 69 |
| 23 | 24 | 29 | 30 | 4.59 | 9 |
| 23 | 24 | 35 | 26 | 10.87 | 1 |
| 24 | 29 | 35 | 36 | 0.00 | 47 |
| 24 | 29 | 18 | 17 | 0.23 | 43 |

3.6 Transition State and activation energy search for oxygen vacancy migration in BSCF

Since BSCF perovskite remains cubic throughout the fuel cell operation temperature range, we considered only cubic structures. According to Kilner,¹⁴⁵ the oxygen vacancy moves along the curved pathway illustrated in Figure. 3-8. As shown in this figure, the transition state (TS) is characterized by different symmetry compared to the initial and final configurations. The TS has a diagonal plane the other structures do not, while the initial and final structures have horizontal and vertical reflection planes not found in TS.

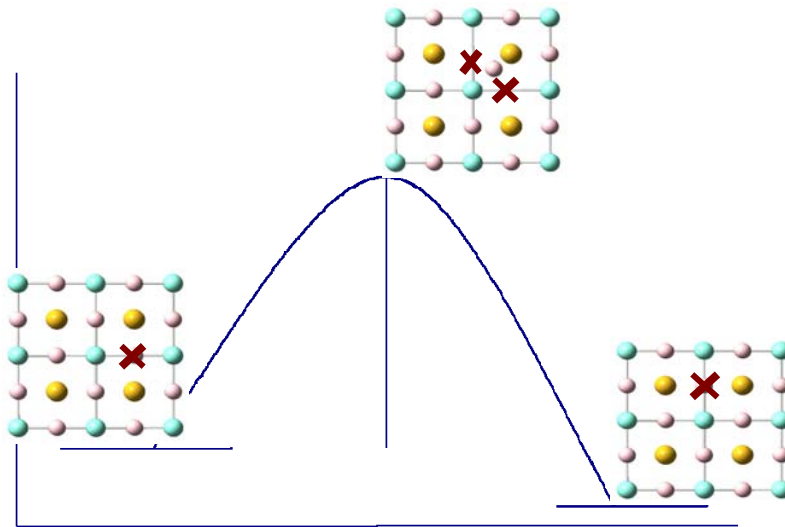


Figure 3-8: Elementary step of oxygen vacancy diffusion in a cubic perovskites

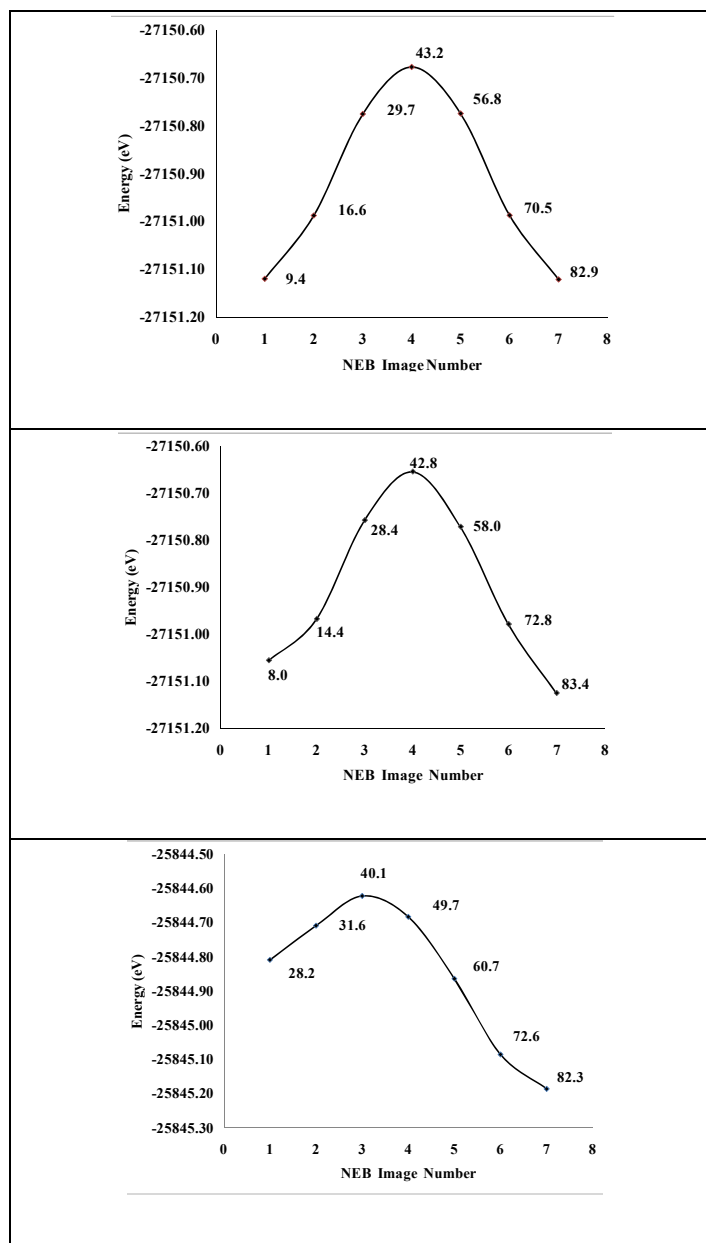


Figure 3-9: Oxygen migration energetics for (a) symmetric ionic arrangements (corresponds to line 8 in Table 3-5), and (b) non-symmetric environment (line 9 in Table 3-5), (c) special case of tetra-vacancy square formation (line 13 in Table 3-5); the MMO angle in marked next to each image point.

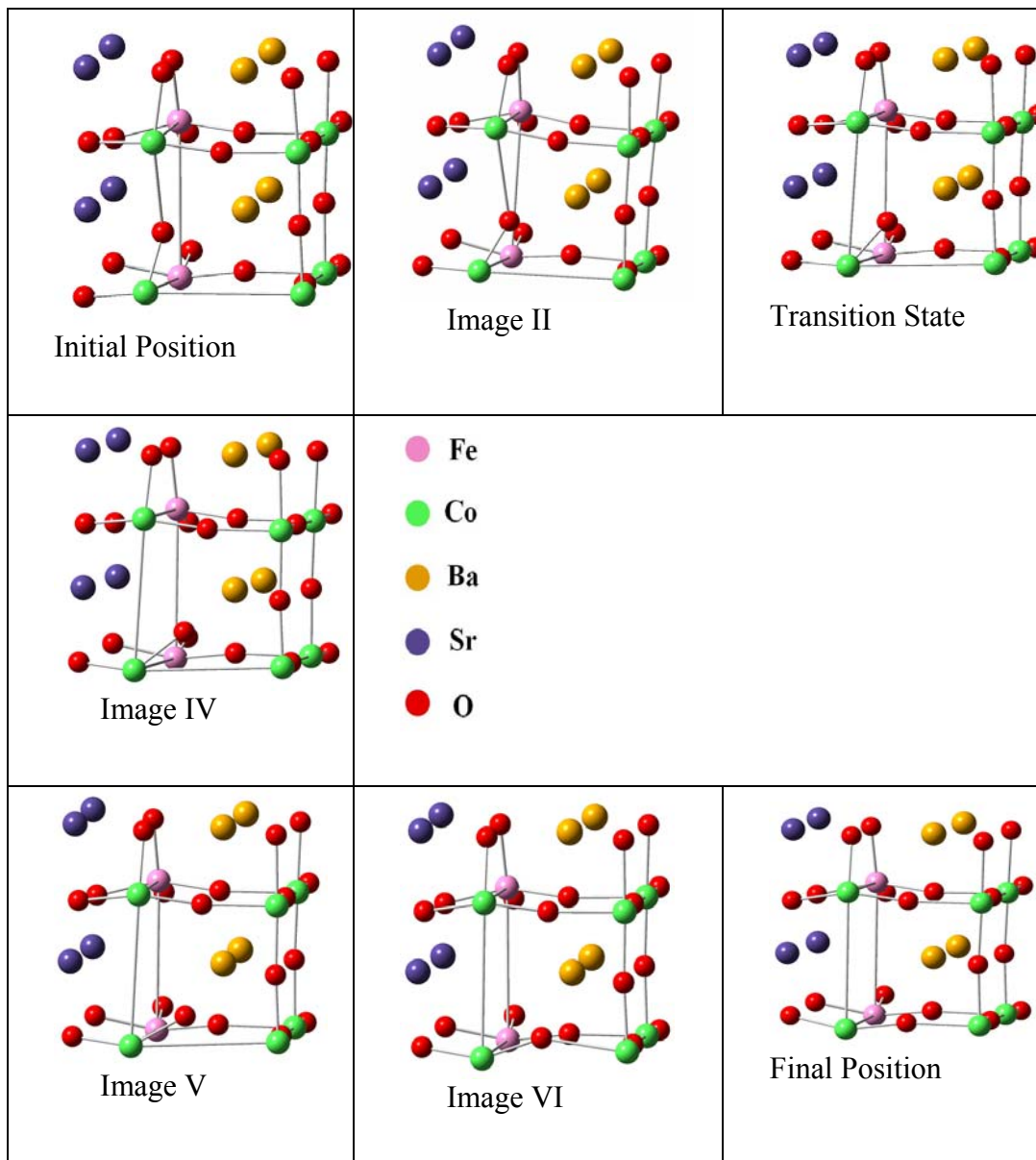


Figure 3-10: The NEB images along the oxygen vacancy migration pathway in square tetra-vacancy case.

Both straight line and curved pathways for oxygen diffusion in LaAlO_3 perovskite were investigated by Hernandez *et. al*³³ using the climbing image nudged elastic band approach. They found straight line to be unfavorable to the curved pathway. The transition state for the curved

pathway was also obtained in their study from DFT molecular dynamics simulations. the pathway described in Figure 3-8.

In the Section 3.3 of this paper we concluded that cation positions in BSCF are essentially random. Thus, we considered various cation distributions in the supercell to calculate the activation energy (also known as the barriers to oxygen hopping, and defined as the difference between the initial state and the transition state energies). They are expected to be dependent on the specific distribution of cations. For comparison, we use the same protocol for two undoped cubic perovskites: SrFeO_{3-δ} and SrCoO_{3-δ}. The calculated activation energies for SrFeO_{3-δ} and SrCoO_{3-δ} were 85.6 kJ/mol and 80.1 kJ/mol respectively. In both cases the ground spin state was considered: multiplicity 5 for iron, and multiplicity 4 for cobalt, according to our calculations.¹²⁴ For SrCoO_{3-δ} in less stable high spin state the activation energy was predicted to be 156.1 kJ/mol, nearly twice that for the intermediate spin state. This sharp increase is not due to the increased lattice parameter predicted for high-spin SrCoO_{3-δ}. The activation energy predicted for high-spin state at the intermediate spin state lattice parameter was found to be somewhat higher. This indicates that it is the presence of Co⁴⁺ in the intermediate spin state that lowers the activation energy in BSCF considerably.

The calculated activation energies for symmetric ion distributions in BSCF are presented in Table 3-5, lines 1-7. These values may be compared with the experimental vacancy diffusion activation energy of 46±2 kJ/mol reported by Shao *et al.*,¹⁰⁸ based on the oxygen permeation measurements conducted for the oxygen partial pressures of 0.025 and 0.21 atm on the opposite sides of the membrane. On average, our results are somewhat lower than this value. The calculated values, however, are more than twice smaller than the activation energies we

calculated for $\text{SrFeO}_{3-\delta}$, and $\text{SrCoO}_{3-\delta}$. This confirms that mobility of oxygen vacancies is significantly higher for BSCF compared to SCF (purely Sr based) perovskite. This reduction in activation energy is the result of the lattice parameter expansion upon increase in the concentration of the large Ba^{2+} ions, weakens cobalt-oxygen interactions in the ground state. The lowest activation energy was found for hopping between two sites located far away from the Fe^{4+} cations. Based on this finding, we suggest that an increased concentration of Co and Ba in BSCF will improve the vacancy mobility in this material. A more accurate atomistic description of the vacancy diffusion in BSCF would require to account for uneven (clustered) vacancy distributions and its effect on the activation barriers of diffusion. The research along these lines is ongoing.

The activation energies for asymmetric ion distributions in BSCF were calculated with NEB method and presented in Table 3-5, lines 8-13. From the comparison of the lines 7 and 8 in this table one can see that symmetry constrained search (line 7) agrees with the results of NEB method (line 8) to within 1.6 kJ/mol. Next two lines (9 and 10) illustrate that for two randomly picked asymmetric cases the predicted activation energy for oxygen migration falls in the same range as the symmetric barriers. Due to computational expense of NEB calculations we did not investigate all the possibilities. The NEB energy profiles for the reaction pathways reported in lines 9 and 10, are presented in Figure. 3-8. The last three lines in the Table 3-5 report the activation energies in the presence of two and three additional vacancies. In lines 11 and 12 we described the most stable cation arrangement (with Boltzmann factors of 9% and 47%) as found in our calculations,¹²⁴ while the edge jump is considered in the last line 13. The activation energies reported in lines 11 and 12 fall within the range of symmetric cases reported in Table 3-

5, the edge jump reported in line 13 is showing lower activation barrier 18.4 kJ/mol. This lower barrier also shows the ease of square vacancy formation.

Table 3-5: Transition states and activation energies of the oxygen vacancy hopping between crystallographic sites, calculated for different local cation arrangements in the BSCF supercell.

| Line Number | closest cations | | | | Ba | | | | Fe | | Migrating Vacancy | | Permanent Vacancy | | ΔH | E_a | |
|-------------|-----------------|---------|---------|---------|----|----|----|----|----|---|-------------------|----|-------------------|----|------------|-------|------|
| | initial | final | initial | Final | | | | | | | | | | | kJ/mol | | |
| 1 | 2Ba+2Sr | 2Ba+2Sr | Fe-O-Co | Fe-O-Co | 10 | 11 | 13 | 16 | 1 | 8 | 22 | 24 | | | 0.0 | 37.9 | |
| 2 | 2Ba+2Sr | 2Ba+2Sr | Co-O-Co | Co-O-Co | 10 | 11 | 13 | 16 | 1 | 8 | 35 | 36 | | | 0.0 | 32.8 | |
| 3 | 2Ba+2Sr | 2Ba+2Sr | Fe-O-Co | Fe-O-Co | 10 | 12 | 14 | 16 | 3 | 5 | 35 | 36 | | | 0.0 | 45.2 | |
| 4 | 2Ba+2Sr | 2Ba+2Sr | Fe-O-Co | Fe-O-Co | 10 | 12 | 14 | 16 | 1 | 8 | 35 | 36 | | | 0.0 | 52.3 | |
| 5 | 2Ba+2Sr | 2Ba+2Sr | Co-O-Co | Co-O-Co | 11 | 12 | 13 | 14 | 3 | 5 | 29 | 24 | | | 0.0 | 34.6 | |
| 6 | 4Ba+0Sr | 4Ba+0Sr | Co-O-Co | Co-O-Co | 11 | 12 | 13 | 14 | 3 | 5 | 38 | 39 | | | 0.0 | 20.2 | |
| 7 | 4Ba+0Sr | 4Ba+0Sr | Fe-O-Co | Fe-O-Co | 10 | 12 | 14 | 16 | 3 | 5 | 38 | 39 | | | 0.0 | 41.2 | |
| 8 | 4Ba+0Sr | 4Ba+0Sr | Fe-O-Co | Fe-O-Co | 10 | 12 | 14 | 16 | 3 | 5 | 38 | 39 | | | 0.0 | 42.6 | |
| 9 | 4Ba+0Sr | 4Ba+0Sr | Co-O-Co | Co-O-Co | 10 | 12 | 14 | 16 | 1 | 5 | 38 | 39 | | | 0.0 | 38.8 | |
| 10 | 4Ba+0Sr | 2Ba+2Sr | Co-O-Co | Co-O-Co | 10 | 12 | 14 | 16 | 1 | 5 | 38 | 40 | | | 21.9 | 46.3 | |
| 11 | 2Ba+2Sr | 2Ba+2Sr | Co-O-Co | Fe-O-Co | 10 | 12 | 14 | 16 | 1 | 5 | 36 | 35 | 23 | 24 | 20.2 | 49.2 | |
| 12 | 2Ba+2Sr | 0Ba+4Sr | Fe-O-Co | Fe-O-Co | 10 | 12 | 14 | 16 | 1 | 5 | 30 | 31 | 23 | 24 | 29 | 24.1 | 29.8 |
| 13 | 2Ba+2Sr | 2Ba+2Sr | Co-O-Co | Co-O-Co | 10 | 12 | 14 | 16 | 1 | 5 | 35 | 40 | 24 | 29 | 36 | 36.6 | 18.3 |

The first column represents case reference number, the next 4 columns list the number and type of the nearest number of the nearest neighbors for the oxygen anion before and after diffusion jump; the following 6 columns contain specific locations of Fe and Ba cations labeled according to the Figure 3-4 (the remaining sites are occupied by Co and Sr). Next 6 columns list the specific locations of the vacancies; the following column reports the migration enthalpy, and the final column reports the calculated activation energy. The activation energies reported in lines 1-7 were obtained via symmetry constrained search, the ones reported in lines 8-13 were obtained with NEB method. Lines 1-10 represent cases with one vacancy in the supercell, line 11 represents the most stable arrangements of three vacancies, and lines 12-13 represent two most stable arrangements for 4 vacancies (linear and square tetramers).

3.7 Conclusions

We applied plane wave DFT calculation to describe the atomic and electronic structure and oxygen transport properties of mixed perovskite BSCF. Our calculations predict an intermediate spin state and a Jahn–Teller distorted coordination for cobalt ions; both are in agreement with experiment. We also show that the cations are completely disordered, while oxygen vacancies exhibit a strong trend to form cluster arrangements. We demonstrated that the most preferable position for oxygen vacancy in the structure with $\delta=0.125$ is between Fe and Co cations. The second vacancy occurs at the most energetically favorable position next to a Co cation which already has a vacancy in its coordination sphere. The preferential vacancy arrangements are predicted to be L-shaped for three, and square for four vacancies. This is in contrast with linear vacancy arrangement and phase transition to brownmillerite type of structure for similar material containing no Ba ions. We predicted the activation energies for oxygen migration using two different methods: symmetry constrained search and Nudged Elastic Band (NEB) method. We also performed similar calculations for supercell, containing more than one vacancy. Lower activation barrier of square cluster of vacancies also suggest that squares of the vacancies form fast. The site-specific activation energies for oxygen migration for all other configurations found to be close to the experimental value. Our calculations found that Co and Ba cations decrease the activation energies for the oxygen vacancy migration. Therefore, we suggest increasing the concentration of these cations in order to improve the ionic conductivity of the cathode materials. It is expected that this will allow a reduction in the operating temperature for Solid Oxide Fuel Cells.

CHAPTER 4 PREDICTION OF HEISENBERG EXCHANGE CONSTANTS IN ORGANOMETALLIC COMPLEXES

Molecular nanomagnets have been proposed as a good candidate for qubits for quantum computation.³⁷ The flexibility in their synthesis represents a distinct advantage over other spin systems, enabling the systematic production of samples with desirable properties. The synthesis and study of magnetic properties of large polynuclear transition metal clusters is a field to which many research groups have devoted considerable effort during the past years. Some of those polynuclear complexes show a slow relaxation of the magnetization that could eventually lead to applications for information storage at the molecular level.¹⁴⁶ Electron spin in the solid state systems are currently considered as one of the promising candidate for storing and processing of quantum information processing. In this perspective both ferro and antiferromagnetic magnets caught interest for spintronic applications in quantum computer.

4.1 Magnetic Hamiltonian and Heisenberg exchange constant

Heisenberg exchange constant J . This constant appears in Heisenberg Hamiltonian that can be written in general form as

$$H = -\sum J_{ij} \cdot S_i \cdot S_j \quad (4-1)$$

here J_{ij} represents the coupling constant between the two magnetic centers i and j with spin states S_i and S_j . The positive J values indicate the ferromagnetic ground state and the negative ones indicate the antiferromagnetic ground state. For the system of two equivalent magnetic centers, the J value can be calculated from the first principles using total energies of the high spin state (where $S_i=S_j$) and the low spin state (where $S_i=-S_j$).

4.2 Theoretical approaches to calculate Heiseberg exchange constants

4.2.1 Different hybrid DFT approaches

The most common theoretical method for prediction of J is Broken Symmetry Density Functional Theory (BS-DFT). In this method the energy correction is made to account for the fact that the low spin state is described by the open shell single Slater determinant, which is not an eigenfunction of the spin operator (spin symmetry is “broken”). The first analytical form for the energy correction was proposed by Noodleman.^{147,148,149,150,151}

$$J_{ij} = \frac{E_{LS} - E_{HS}}{S_{\max}^2} \quad (4-2)$$

here E_{LS} and E_{HS} are the computed energies of the low and high spin states, and $S_{\max} = |S_i| + |S_j|$. This correction scheme is applicable for weakly bonded molecular fragments with small overlap between the magnetic orbitals.^{147,152, 153} An alternative correction scheme has been used by Ruiz and co-workers.¹⁵⁴ In this scheme, J value is computed as

$$J_{ij} = \frac{E_{LS} - E_{HS}}{S_{\max}(S_{\max} + 1)} \quad (4-3)$$

This scheme assumes strong bonding between molecular fragments with localized spins, and may be more appropriate for binuclear complexes than (4-2). The third way to compute J is independent of the bonding situation in the molecule. It had been proposed by Nishino *et al.*¹⁵⁵

$$J_{ij} = \frac{E_{LS} - E_{HS}}{\langle S^2 \rangle_{HS} - \langle S^2 \rangle_{LS}} \quad (4-4)$$

here $\langle S^2 \rangle_{HS}$ and $\langle S^2 \rangle_{BS}$ are the total spin angular momentum expectation values for high and low spin states. This correction scheme approximately accounts for the overlap between

magnetic orbitals. Less approximate schemes may also take into account differences in the overlap between different magnetic orbitals of the same system.^{156, 157} Since pure DFT usually overestimates J values, BS-DFT is making use of the hybrid exchange-correlation functionals, where fraction of the orbital-dependent Hartree-Fock exchange is replacing local and semi-local exchange. Unfortunately, BS-DFT was not sufficiently accurate in predictions of J for binuclear complexes with acetate bridges,^{151,158} presumably due to strong delocalization of the spin density from the metal centers to the ligands.

4.2.2 DFT+U methodology

The attractive alternative for BS-DFT method is DFT+U, introduced by Anisimov *et al.*⁹ and simplified by Cococcioni *et al.*¹⁵⁹ In this work we adopt the empirical approach and show that both metal centers and ligand atoms need to be assigned a specific U values in order to accurately describe the properties of molecular magnets.

Considering importance of superexchange interactions, Cao *et. al.*¹⁶⁰ performed DFT+U calculations for Ni(hmp)(MeOH)Cl₄ complex, where they both metal and ligand oxygen atoms were assigned their U parameters. Because of the strong correlation effects in this system, the pure DFT approach artificially results in the hybridization of orbitals, leading to AFM coupling. The inclusion of a Hubbard-U term for both the Ni 3*d* and O 2*p* electrons greatly enhances the localization, and is essential in order to obtain the correct ferromagnetic ground state and positive value for the exchange-coupling constant. The rationale for using the parameter U for both the *p* and *d* orbital is the following. Coulomb interactions between oxygen 2*p* electrons are comparable to those between *d* electrons,^{161,162} and should hence be taken into consideration. However, since oxygen usually bears a fully occupied *p*-shell, this correlation effect contributes

equally to the low- and high-spin states. Therefore, DFT+U^d already yield a satisfactory description of the ground state. However, when 2*p*-electrons of the ligand are involved in π -conjugated system, DFT+U^{*p+d*} has to be used for both the 3*d* and oxygen 2*p* electrons in order to obtain the correct ground state for the molecule.

4.3 Computational Details

All the reported calculations were done using the Quantum-ESPRESSO-4.0.1 package,¹²² using PBE exchange-correlation functional, Vanderbilt ultrasoft pseudopotentials¹²¹ and a plane-wave basis set. We employ the same protocol used in our previous studies.¹²⁴ Namely, the energy cutoffs for the wave functions and charge densities were set at 25 and 250 Ry to ensure total energy convergence, spin polarized approach, the Marzari-Vanderbilt¹²³ cold smearing (smearing factor 0.0008), and local Thomas-Fermi mixing mode to improve SCF convergence. To better describe the magnetic states for manganese, both valence and semicore shells (3*s*3*p*3*d*4*s*) were treated explicitly, while rest of the electrons was replaced by Vanderbilt Ultrasoft pseudopotential. For homovalent antiferromagnetic state we used equal and opposite “starting magnetization” on manganese to ensure correct antiferromagnetic state. For heterovalent compound we used different “starting magnetization” on manganese atoms with opposite signs. All molecular structures were optimized in their most stable (low spin, except for complex *III*) state starting from atomic coordinates, taken from X-Ray diffraction data with geometrically added hydrogen atoms. The optimization was found to be critically important for the accuracy of the final results, presumably due to inaccuracies introduced in some of X-Ray structures by partial disorder.

In application of DFT+U method, we followed the protocol described by Cao *et al.*¹⁶⁰ We used simplified rotational-invariant formulation, which was originally developed by Liechtenstein *et al.*¹⁰ as basis set independent generalization of DFT+U. The values of the U parameter for both the metal atom and the ligand atoms (O and N) were empirically adjusted to fit the experimental spin splitting energies for the benchmark set of five small binuclear manganese complexes with various oxidation states (+2, +3 and +4), as described in Section 4.4.

4.4 Prediction of Heisenberg exchange constants using DFT+U for binuclear manganese complexes

In order to calibrate DFT+U approach and validate it for predictions of the coupling constant values, we selected five binuclear manganese complexes presented in Figure 4-1. The manganese complexes of this type have been extensively studied. They have rich redox chemistry and play a functional role in a variety of biologically important metalloproteins.¹⁶³ In particular, oxo-manganese clusters are either known or have been implicated in the catalytic function of manganese catalase,^{163,164} manganese ribonucleotide reductase,¹⁶⁵⁻¹⁶⁷ and the oxygen-evolving complex of photosystem II.^{168,169,170}

For this work we select a representative set of five different classes, based on the oxidation number and type of bridging groups: (I) Mn(IV) di- μ -oxo; (II) Mn(IV) di- μ -oxo- μ -carboxylato; (III) Mn(III) μ -oxo-di- μ -carboxylato, and (IV) Mn(II) tri- μ -carboxylato, (V) Mn(III)Mn(IV) μ -oxo-di- μ -carboxylato bridged systems. Our molecule of interest [Mn₆III Mn₆II(O₂CMe)₁₄(mda)₈] (mda=N-methyl diethanolamine) is a mixed valence Mn complex, containing both acetate and oxo bridges. We choose our benchmark molecules so that they have the similar structural features with The complexes III and IV were selected for this

study to represent oxidation states, Mn (III) and Mn(II) bridged by two and three acetate ligands, respectively, and complex V represents the mixed valence Mn(III)-Mn(IV) complex, with the structure similar to the Mn(III)-Mn(III) complex.

The exchange coupling in most of these complexes were previously studied with BS-DFT, combined with spin contamination correction schemes (Eq. 2-4).^{171, 151} While BS-DFT gives reasonable agreement with experiment for the complex I, its prediction was 63% in error for complex II. Similar failures of hybrid DFT were reported for other molecules with acetate bridge,^{151,158} and were traced to the delocalization of magnetic orbitals from the manganese centers to the ligand atoms¹⁵¹ for complex III the BS-DFT not only fails to predict the quantitative value of exchange constant but also predicts the incorrect ground state. BS-DFT calculation¹⁵⁸ for complex V produced overestimated J values.

The Table 4-1 reports the J values for the benchmark complexes, obtained in this work, and compares them to the experimental J values. Predictions obtained in BS-DFT formalism using B3LYP exchange-correlation functional and spin-contamination correction scheme (Eq. 4-2) are also shown for comparison. Out of these five complexes the complex IV including Mn(II) magnetic center demonstrates the weakest magnetic coupling J , similar to that in the Mn12 wheel.¹⁷¹ The second weakest coupling is found in complex III with Mn(III) center; this complex has ferromagnetic ground state. The complex (V) is included to validate the method for Mn(III)-Mn(IV) center mixed-valence compound.

Table 4-1: Heisenberg exchange constant J for the binuclear complexes, calculated using DFT+U on Mn and ligands (U(Mn)=2.1 eV, U(O)=1.0 eV, U(N)=0.2 eV), DFT+U on Mn only, and pure DFT, compared to BS-DFT predictions and to the experimental data.

| | Chemical formula | J (cm ⁻¹) | | | | |
|-----|--|-------------------------|----------------------------------|--------|---------------------|---------------------|
| | | Plane Wave calculations | | | BS-DFT | Experiment |
| | | DFT+U metal+ligand | DFT+U ^h metal only | DFT | | |
| I | [Mn ₂ (IV)(μO) ₂ (phen) ₄] ⁴⁺ | -143.6 | -166.6 | -383.3 | -131.9 ^b | -147.0 ^a |
| II | [Mn ₂ (IV)(μO) ₂ ((ac))(Me ₄ dtne)] ³⁺ | -71.9 | -87.4 | -255.9 | -37.5 ^b | -100.0 ^c |
| III | [Mn ₂ (III)(μO)(ac) ₂ (tacn) ₂] ²⁺ | 5.6 | -3.64 | -96.3 | -40.0 ^c | 10.0 ^d |
| IV | [Mn ₂ (II)(ac) ₃ (bpea) ₂] ⁺ | -7.7 | -18.8 | -13.8 | - | -1.3 ^f |
| V | [Mn(III)Mn(IV)(μO) ₂ (ac)(tacn) ₂] ²⁺ | -234.0 | -247.6 | -479.3 | -405. ^c | -220. ^g |

^a Ref. ¹⁷²; ^b Ref. ¹⁵¹; ^c Ref. ¹⁷³; ^d Ref. ¹⁷⁴; ^e Ref. ¹⁵⁸; ^f Ref. ¹⁷⁵; ^g Ref. ¹⁷⁶

Our calculated data are in agreement with the experimental values to within 15%, for both molecules with and without acetate Bridge, compare to 65% deviation produced by broken symmetry DFT. As one can see from this table, pure DFT dramatically overestimates the antiferromagnetic interactions for all the complexes, including the complex *III* which is known to be ferromagnetic. DFT+U^d has good agreements with experimental results for all the complexes except the Complex *III*. DFT+U^{p+d} improves the agreement with experiment for the complex *IV*, and is the only method to reproduce the ferromagnetic ground state in complex *III*.

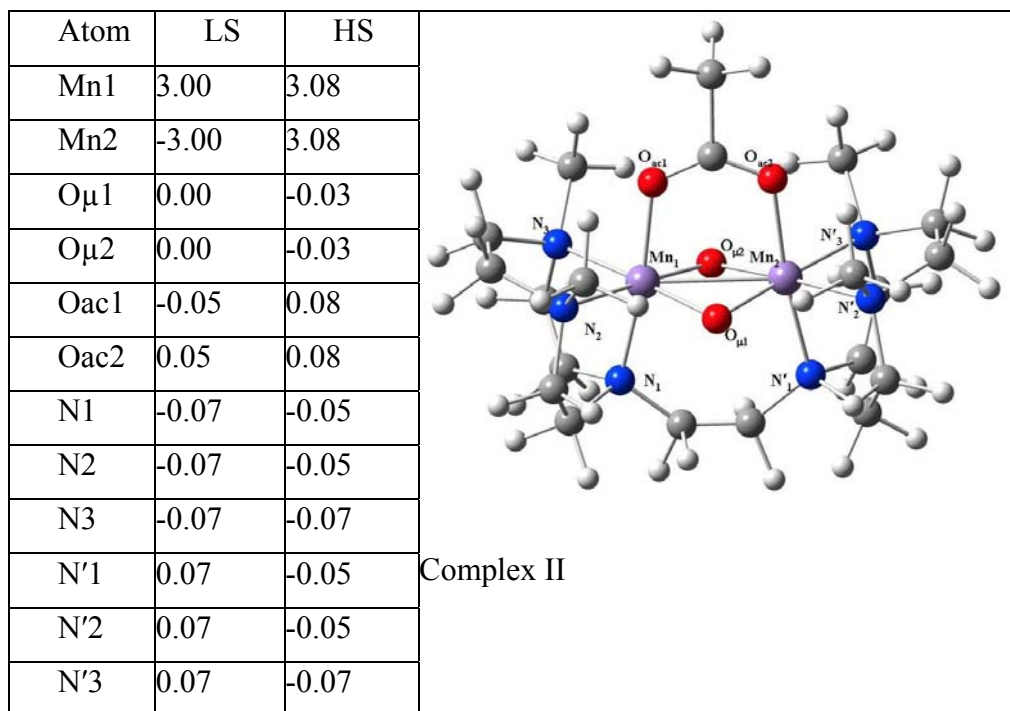
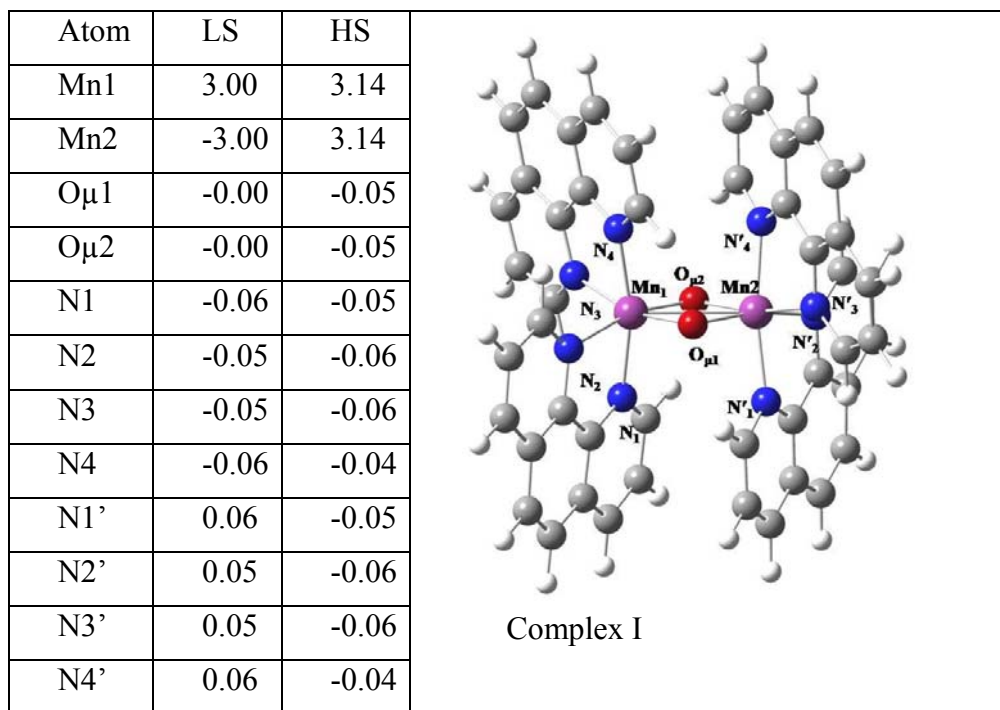
Table 4-2: Dependence of Heisenberg Exchange Constant (J) on atomic Hubbard U parameters for complex *II*.

| U (ev) | | | $J \text{ cm}^{-1}$ |
|--------|---|-----|---------------------|
| Mn | O | N | |
| 1 | 1 | 0.2 | -147.77 |
| 2.1 | 1 | 0.2 | -71.92 |
| 3 | 1 | 0.2 | -13.84 |
| 4 | 1 | 0.2 | 48.76 |
| 6 | 1 | 0.2 | 169.84 |
| 2.1 | 3 | 0.2 | -55.27 |
| 2.1 | 5 | 0.2 | -50.80 |
| 2.1 | 1 | 2.0 | -62.03 |

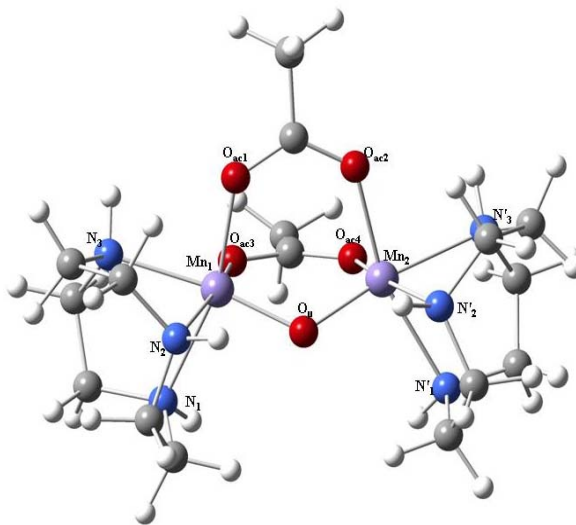
Next, we analyzed the sensitivity of the magnetic coupling to the variations of the Hubbard U parameter, and reported the results for the complex *II* in Table 4-2. As one can see, J value is the most sensitive to the choice of U on Mn atom, with larger values drastically stabilizing HS state. Increase of the Hubbard parameter on the ligands (both μ -oxo and μ -carboxylato) also helps to stabilize ferromagnetic state, to a smaller degree. This is in agreement with Table 4-1 where ferromagnetic state is stabilized in the order pure DFT < DFT+ U^d < DFT+ U^{p+d} .

Finally, we analyzed the electronic structure of the converged HS and LS states. The atomic spin densities obtained with Löwdin population analysis are presented in Figure 4-1. As one can see from these values, the oxide dianions ($O\mu$), and aliphatic N atoms that serve as pure σ -donors, have spin polarization opposite to that of the nearest Mn ion, in agreement with superexchange mechanism we described earlier. The aromatic N atoms have nearly zero spin-

polarization. On the other hand, the O atoms of the acetate cations have the same spin polarization as the nearest Mn cations. This observation contradicts simple superexchange picture and can be explained with dative (also known as π -back bonding) mechanism.¹⁷⁷ The acetate has vacant π -orbital extended over 3 atoms, and can serve as π -acceptor for the d -electrons of the Mn cation. As a result, Anderson's superexchange mechanism, developed for σ -bonding metal-ligand interactions, no longer holds. This π -delocalization may be the reason why BS-DFT approach yields large numerical errors for the complexes containing acetate. The DFT+U scheme, however, does not rely on this assumption and handles these acetate-containing complexes equally well.

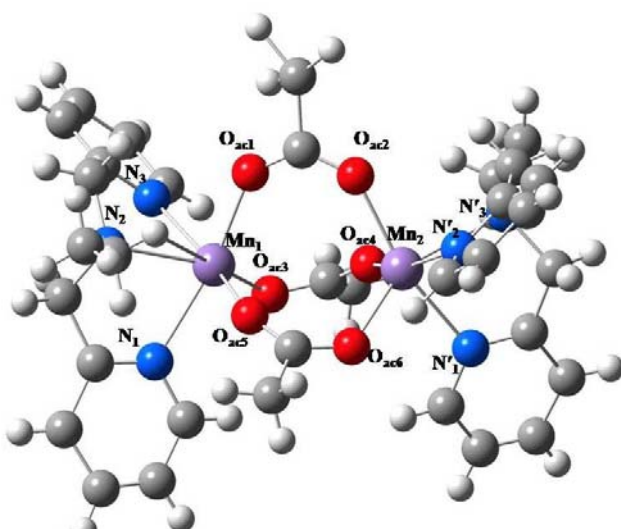


| Atom | LS | HS |
|---------|-------|-------|
| Mn1 | 3.74 | 3.86 |
| Mn2 | -3.94 | 3.97 |
| O μ | 0.00 | -0.02 |
| Oac1 | 0.02 | 0.02 |
| Oac2 | -0.03 | 0.03 |
| Oac3 | 0.00 | 0.01 |
| Oac4 | 0.00 | 0.01 |
| N1 | -0.01 | 0.00 |
| N2 | -0.05 | -0.03 |
| N3 | 0.00 | 0.00 |
| N1' | 0.04 | -0.02 |
| N2' | 0.03 | -0.03 |
| N3' | 0.01 | -0.01 |



Complex III

| Atom | LS | HS |
|--------|-------|------|
| Mn1 | 4.70 | 4.70 |
| Mn2 | -4.70 | 4.70 |
| Oac1 | 0.02 | 0.01 |
| Oac2 | -0.02 | 0.01 |
| Oac3 | 0.02 | 0.01 |
| Oac4 | -0.02 | 0.01 |
| Oac5 | 0.02 | 0.01 |
| Oac6 | -0.02 | 0.01 |
| N1=N1' | 0.00 | 0.00 |
| N2=N2' | 0.00 | 0.00 |
| N3=N3' | 0.00 | 0.00 |



Complex IV

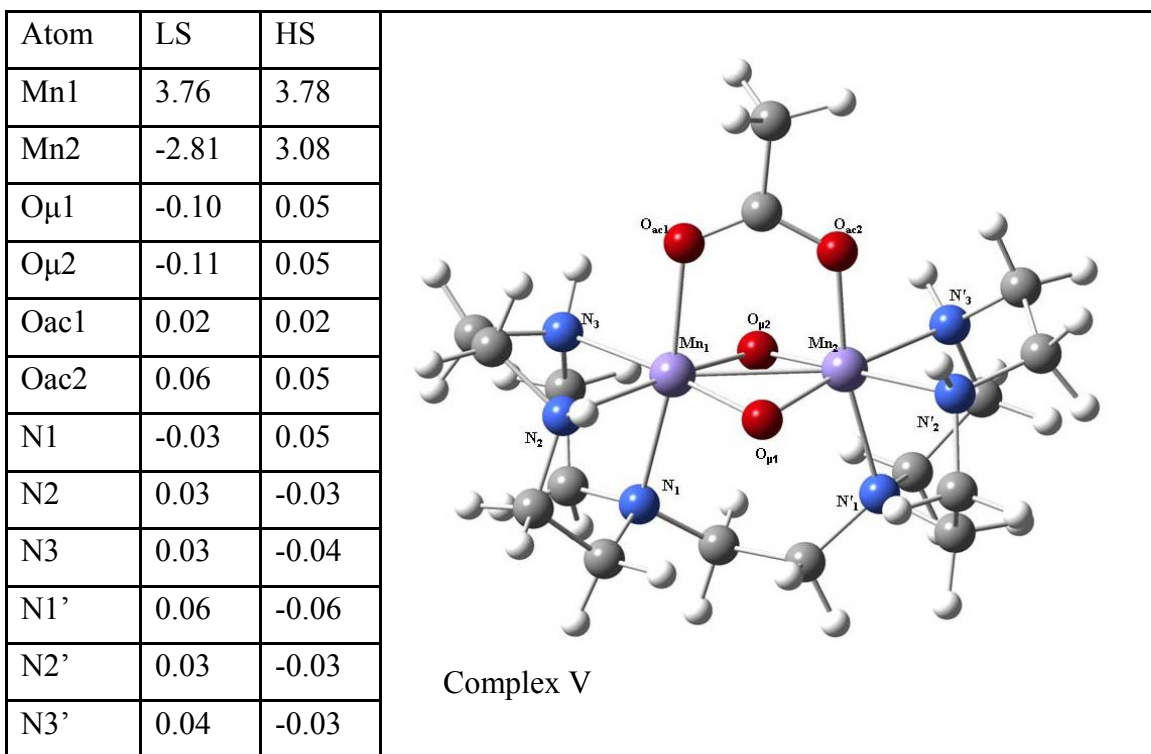


Figure 4-1 Molecular structures of the binuclear complexes of the benchmark set and Löwdin spin densities in their low-spin (LS) and high-spin (HS) states.

4.5 Antiferromagnetic wheel and Heisenberg exchange constant

Predictions of magnetic properties of molecular systems present a long standing problem, as they require a balanced description of static and dynamic electron correlation. Density Functional Theory (DFT) approaches is the only ab initio method capable to describe large molecules, such as Mn_{12}Ac , Fe_8 , and V_{15} classical molecular magnets¹⁷⁸⁻¹⁸⁴. Two variations of DFT are commonly used for prediction of J values. One is broken symmetry DFT proposed by Noodleman^{147,149,150,185,186} and Yamaguchi¹⁸⁷⁻¹⁹³. The other versions of BSDFT formalism are proposed by Ruiz¹⁵⁴ and Nishino.¹⁵⁵ Less approximate schemes may also take into account differences in the overlap between different magnetic orbitals of the same systems.^{156,157} BSDFT is known to have its limitations in at least three different cases i) acetate bridged manganese complexes.¹⁵¹ ii) mix valence¹⁵⁸ and iii) ferromagnetic coupling¹⁵⁸. The alternative variation of DFT is known as DFT+U approach (U stands for onsite coulomb repulsion). It was used for J value calculations are applied on molecular magnets¹⁹⁴⁻¹⁹⁷ and organometallics.¹⁹⁸⁻²⁰² The general approach in DFT+U is to add Hubbard U on d orbitals in metal atoms, but Cao *et al.*²⁰³ showed adding Hubbard U not only on metal but also on ligand atoms p orbital is needed to predict correct ferromagnetic order. We are referring this methodology as DFT+U ^{$p+d$} .

In our previous paper we successfully applied DFT+U ^{$p+d$} approach for different valence Mn (+2, +3, +4, including mix valence) complexes having various ligands.²⁰⁴ We applied DFT+U ^{$p+d$} approach using same U values to predict antiferromagnetic exchange Mn1-Mn6' center in $\text{Mn}_{12}(\text{mdea})$ wheel in the same paper.²⁰⁴ In this paper we applied similar approach to predict six Heisenberg exchange constants in two different Mn_{12} wheels. The general chemical formula for the wheels is $[\text{Mn}_{12}\text{Rdea}_8(\text{CH}_3\text{COO})_{14}].n(\text{CH}_3\text{CN})$, in which the Rdea^{2-} are dianions

of N-R diethanolamine, with R = a(allyl) and m(methyl). Both the wheels reported to have S=7 spin ground state^{205,206} and weak antiferromagnetic coupling between two identical halves having six manganese atoms.

Predictions of magnetic properties of molecular systems present a long standing problem, as they require a balanced description of static and dynamic electron correlation. Density Functional Theory (DFT) approach is the only ab initio method capable to describe large molecules, such as Mn₁₂Ac, Fe₈, and V₁₅ classical molecular magnets¹⁷⁸⁻¹⁸⁴. Two variations of DFT are commonly used for prediction of *J* values. One is broken symmetry DFT proposed by Noodleman^{147,149,150,185,186} and Yamaguchi.¹⁸⁷⁻¹⁹³ The other versions of BSDFT formalism are proposed by Ruiz¹⁵⁴ and Nishino.¹⁵⁵ Less approximate schemes may also take into account differences in the overlap between different magnetic orbitals of the same systems.^{156,157} BSDFT is known to have its limitations in at least three different cases i) acetate bridged manganese complexes,¹⁵¹ ii) mix valence¹⁵⁸ and iii) ferromagnetic coupling,¹⁵⁸ The alternative variation of DFT is known as DFT+U approach (U stands for onsite coulomb repulsion). It was used for *J* value calculations are applied on molecular magnets¹⁹⁴⁻¹⁹⁷ and organometallics.¹⁹⁸⁻²⁰² The general approach in DFT+U is to add Hubbard U on d orbitals in metal atoms, but Cao *et al.*²⁰³ showed adding Hubbard U not only on metal but also on ligand atoms p orbital is needed to predict correct ferromagnetic order. We are referring this methodology as DFT+U^{*p+d*}.

In our previous paper we successfully applied DFT+U^{*p+d*} approach for different valence Mn (+2, +3, +4, including mix valence) complexes having various ligands.²⁰⁴ We applied DFT+U^{*p+d*} approach using same U values to predict antiferromagnetic exchange Mn1-Mn6' center in Mn₁₂(mdea) wheel in the same paper.²⁰⁴ In this paper we applied similar approach to

predict six Heisenberg exchange constants in two different Mn_{12} wheels. The general chemical formula for the wheels is $[Mn_{12}Rdea_8(CH_3COO)_{14}].n(CH_3CN)$, in which the $Rdea^{2-}$ are dianions of N-R diethanolamine, with R = a(allyl) and m(methyl). Both the wheels reported to have $S=7$ spin ground state^{205,206} and weak antiferromagnetic coupling between two identical halves having six manganese atoms.

4.6 All inner Heisenberg exchange constants for Mn12 based magnetic wheels

In application of DFT+U method, we followed the protocol used in our previous work.²⁰⁴ We employed simplified rotationally-invariant DFT+U formulation, implemented by Cococcioni in Quantum-ESPRESSO-4.0.1 package¹⁵⁹. The values of the U parameter for both the metal atom and the ligand atoms (O and N) were empirically adjusted to the optimum values 2.10 eV for Mn, 1.00 eV for O and 0.20 eV for N that fit the experimental spin splitting energies for the benchmark set of five small dinuclear manganese complexes in variety of oxidation states (+2, +3 and +4).²⁰⁴

Both the molecules $Mn_{12}(Rdea)$ include alternating Mn^{+2} and Mn^{+3} ions arranged in a single stranded wheel (Figure 4-2), symmetrical under inversion. The ion Mn^{+3} has d^4 high spin electron configuration and Jahn-Teller distorted octahedral coordination. The Mn^{+2} ions are found in two different coordination environments: one octahedral, and another one is pentagonal bipyramidal. Experiments performed for both the wheels yields $S=7$ spin ground state^{205,206} which is consistent with the atomic spin alignments presented in Figure 4-2. To date there are no quantitative measurements of the exchange coupling parameters reported for these molecules. The qualitative predictions suggest the weakest magnetic coupling should be present between $Mn(1)-Mn(6')$ ^{205,206}.

Next, we constructed six hypothetical low-spin states, by partitioning the wheel into two equal sets of 6 atoms each and inverting the spins for one of these sets. Assuming the second-neighbor magnetic interactions to be negligible, the energy for each low spin state ($S=0$)_{nm} allows to calculate the magnetic coupling parameters as

$$J_{nm} = \frac{E_{(S=0)nm} - E_{(S=7)}}{2 \times S_n \times S_m} \quad (4-5)$$

$E_{(S=0)nm}$ is energy of ($S=0$)_{nm} alignments shown in column 3 of scheme 1, $E_{(S=7)}$ is energy of the spin configuration shown in third column of scheme 4-1. $E_{(S=7)}$ is the energy of experimental spin ground state of the wheel. $S_n = \frac{5}{2}$ and $S_m = 2$ ($n = 2, 4, 6$ and $m = 1, 3, 5$ according to the Scheme 4-1). Since molecules are symmetric $J_{nm} = J_{mn}$.

From Figure 4-2 one can see that out of six magnetic interactions present in the wheel, two are ferromagnetic and four are antiferromagnetic. The antiferromagnetic interactions are confirmed to be between Mn(1)-Mn(2), Mn(2)-Mn(3), Mn(3)-Mn(4), and Mn(5)-Mn(6) ferromagnetic interactions are between Mn(3)-Mn(4) and Mn(4)-Mn(5). In Scheme 4-1 we summarize our calculation procedure. Our method is different from the one used by Cano *et al.*²⁰⁷ In their work²⁰⁷ the energies for 32 different high, low and intermediate total spin states were calculated and quantum Monte Carlo to solve the large system of equations and find J values for both first and second-neighbor interactions. The later ones were found to be rather small, confirming our assumption.

Several DFT studies predicting J values for Mn₁₂(Mdea) wheel^{205,207} had been published. We summarized the previous and current DFT results in Table 4-3. The first BSDFT calculations on Mn₁₂ wheel was performed by Foguet-Albiol²⁰⁵ *et al.* (presented in sixth column of Table 4-

3). In order to reduce the computational expense, the wheel was fragmented into several tri- and bi-nuclear clusters. This study predicted Mn(1)-Mn(6') centers to couple ferromagnetically, resulting in S=0 ground state, in disagreement with experiment²⁰⁵. Cano *et al.*²⁰⁷ calculated the Heisenberg exchange parameters for the whole magnetic wheel using variety of spin states and fitting the J values using their Monte Carlo technique. Their results for the pure and hybrid DFT functionals are compared in Columns 4 and 5 of the Table 4-3. The weakest magnetic interaction Mn(1)-Mn(6') corresponds to the ferromagnetic (incorrect) spin coupling when pure functional PBE is used, and antiferromagnetic one when hybrid functional B3LYP is used. However, the hybrid functional predicts all the J values to be roughly the same order of magnitude. This contradicts the conclusion of much stronger coupling between the remaining magnetic centers, based on experimental observations.²⁰⁵

Our own results with pure PBE (column 7) reproduce the previously published²⁰⁷ coupling parameters rather well despite the difference in and the formalism used for J extraction and the basis (plane waves vs. Gaussian). The geometry optimization changes the coupling of the Mn(1)-Mn(6') centers from incorrect ferromagnetic to correct antiferromagnetic. Its absolute value, however, appears to be close to four other magnetic interactions in the ring. From comparison of the columns 2 and 3 one can see that optimizing the molecular structure changes the interatomic distances by c.a. 0.01 Å. However, because of this small change the Mn(1)-Mn(6') coupling becomes antiferromagnetic, in agreement with experiment. One can hypothesize that inaccuracies in experimental atomic coordinates are due to static disorder brought about by the partial escape of the solvent molecules from the lattice. The use of Hubbard parameter U (column 9) reduces antiferromagnetic coupling Mn(1)-Mn(6') by an order of

magnitude, and increases the ferromagnetic couplings Mn(3)-Mn(4) and Mn(4)-Mn(5) five to ten times, thus improving the agreement with experiment. Indeed, the magnetic study on a similar wheel by Ramsey *et al.* ²⁰⁶ suggested it is a dimer of two strongly coupled six-atom sets, connected with a very weak antiferromagnetic interaction ²⁰⁶. Ramsey *et al.* also inferred that the weakest coupling is observed between Mn(1)-Mn(6') centers.

Next we applied a similar computational protocol (optimization, followed by DFT+U) to another Mn₁₂(Adea) wheel. ²⁰⁸ This wheel is reported to have the same ground spin state (S=7) as Mn₁₂(Mdea) wheel ²⁰⁶ and similar spin alignment. The calculated exchange parameters are reported in the last column Table 4-3. Our calculation predicts the weakest *J* is an order of magnitude smaller than the next weak coupling between Mn(1)-Mn(2) for Mn₁₂(Adea) (Figure 4-3).

Another noticeable feature in *J* couplings reported in Table 4-3 is the relatively high magnitude of ferromagnetic coupling between Mn(3)-Mn(4) and Mn(4)-Mn(5) centers, which was not predicted by other DFT studies ^{205,207}. The recent inelastic neutron scattering measurements ²⁰⁹ also point toward significantly higher magnitude of ferromagnetic coupling in Mn(3)-Mn(4)-Mn(5) fragment of Mn₁₂(Mdea). According to Meier and Loss ²¹⁰ a strongly coupled multicenter fragment can be described as a single large spin center. Considering that model, both the wheels especially Mn₁₂(Adea) fits in the model for perfect antiferromagnetic wheel alternating spin up and spin down magnetic moments (Figure 4-3).

In order to investigate the details of electronic structure and estimate the ability of these molecules to act as spin-valves in molecular spintronics context, one may consider the Löwdin population analysis, shown on Table 4-4, and projected density of states (PDOS) for different

atoms high spin ground states ($S=7$) in both wheels, presented in Figure 4-4 and Figure 4-5 for Mdea and Adea wheels respectively. The results of Löwdin population analysis confirm spin polarization for different manganese atoms (spin up for octahedral Mn^{+3} , spin down for octahedral Mn^{+2} and pbp Mn^{+3}). From spin polarization of ligand atoms (N, μ -O, and acetate O) one may conclude that the nitrogen atoms connected with bipiramidal and octahedral coordinated Mn have different spin densities. The acetate oxygen and oxo bridged oxygen (μ -O) responsible for superexchange have similar spin polarization values, but PDOS diagram reveals the differences in their electronic structure.

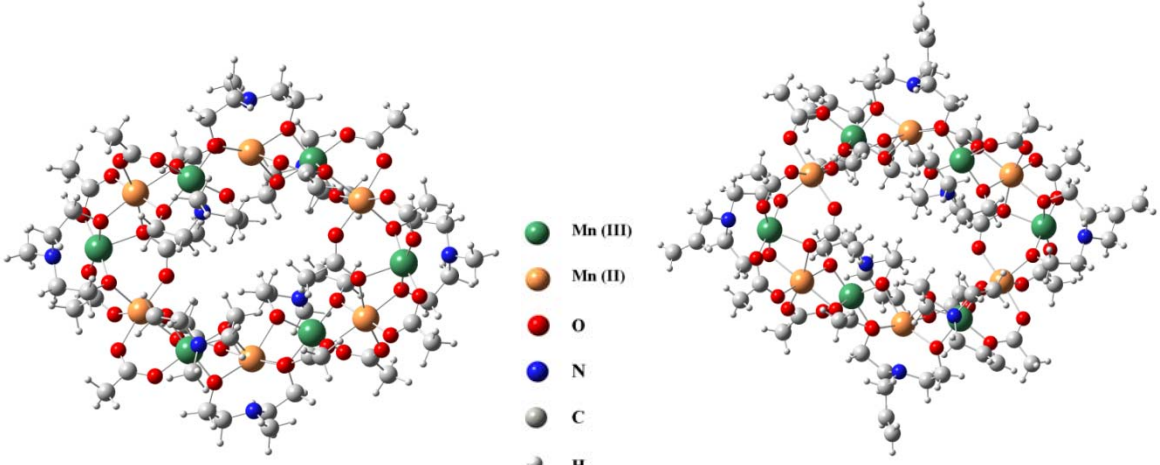
Figure 4-4 shows the PDOS for $\text{Mn}_{12}(\text{Mdea})$ and Figure 4-5 is for $\text{Mn}_{12}(\text{Adea})$ wheels. The first row in Figure 4-4 represented the total PDOS for the molecule. From the PDOS data one can see that for both N atoms contribute to HOMO, along with Mn^{3+} (Mn(3)), while acetate O and Mn^{+2} are contributing in LUMO. The $\text{Mn}^{+3}(d^4)$ Jahn-Teller distortion as a result shows a split e_g levels, where as the octahedral d^5 spin down shows degenerate e_g levels. In case of Adea wheel oxygen atom involved in superexchange is taking part as an acceptor, while in Mdea there is no such phenomenon. Another difference is evident from PDOS diagram in Mdea the Mn(3) (Figure 4-6) is involved in HOMO where in Adea wheel the HOMO level is nearly degenerate between Mn(3) and Mn(1). The spin densities in Table 4-4 shows nitrogen involved in octahedral coordination is acting as σ donor.

From Figure 4-4 and Figure 4-5, we can see the Mn^{+3} has smaller highest occupied molecular orbital (HOMO) and lowest unoccupied molecular orbital (LUMO) gap than Mn^{+2} (both octahedral and pentagonal bipyramidal co-ordination). If we compare DOS of Mn(1) and Mn(3), in Figure 4-6 both the cases Mn(3) shows little more HOMO-LUMO energy gap than

Mn(1). According to Hoffmann and Hay²¹¹ the antiferromagnetic coupling is more distinct when the HOMO-LUMO energy difference is higher. Based on this we can say the presence of Mn1 reduces the antiferromagnetic coupling. Similar observation can be made from Figure 4-6 for Mn⁺² octahedral and Mn⁺² pbp, the pbp manganese showed more HOMO-LUMO energy gap than octahedral bivalent manganese. This electronic structure analysis can justify why the Mn(3)-Mn(4)-Mn(5) shows stronger magnetic coupling than other Mn-Mn couplings. Though these energy differences are very small but we need to consider the exchange parameters in this wheel is c.a. 1 cm⁻¹.

To conclude, we calculated all nearest-neighbor Heisenberg exchange parameters for Mn₁₂(Mdea) and Mn₁₂(Adea) using DFT+U^{b+d}. Our calculations successfully reproduce the S=7 ground spin states. The expected weakest coupling parameter between Mn(1)-Mn(6') is confirmed for both magnetic wheels. The stronger ferromagnetic coupling between the Mn(3)-Mn(4) and Mn(4)-Mn(5) pairs is also predicted, in agreement with recent Inelastic Neutron Scattering observations.²⁰⁹ The Löwdin population and PDOS analysis helps to rationalize the stronger ferromagnetic coupling in Mn(3)-Mn(4)-Mn(5) zone by quantitative comparison between HOMO-LUMO energy gap in different magnetic centers.

Table 4-3 Calculated Heisenberg Exchange constants of $\text{Mn}_{12}(\text{Mdea})$ using DFT+U and previous first principle calculations. The first column is labeled according to Figure 4-2. Second and third columns are showing the Mn-Mn bond distance from X-ray data and optimized structure respectively. Fourth and fifth column is showing the DFT result reported by Cano *et al.*²⁰⁷ The sixth column is the BSDFT value obtained by fragmenting $\text{Mn}_{12}(\text{mdea})$ wheel²⁰⁵. The seventh and eighth columns are J values calculated by DFT+U^{p+d} for X ray and optimized geometry. The last column is representing the Heisenberg Exchange constants for $\text{Mn}_{12}(\text{Adea})$



| | Bond Length (Å) | | $J(\text{cm}^{-1})$ | | | | | | |
|----------|-----------------|------|-------------------------------|----------------------|------------------------------------|----------------|--------------|-------------------------------|----------------|
| | X-ray | Opt | $\text{Mn}_{12}(\text{Mdea})$ | | | | | $\text{Mn}_{12}(\text{Adea})$ | |
| | | | PBE ₂₀₇ | B3LYP ₂₀₇ | B3LYP ²⁰⁵ (Fragment) | DFT (X-ray) | DFT (Opt) | DFT+U (Opt) | DFT+U (Opt) |
| J_{16} | 3.46 | 3.44 | +1.2 | -3.5 | +0.04 | +4.6 | -7.4 | -0.8 | -2.4 |
| J_{12} | 3.21 | 3.21 | -6.0 | -5.6 | -2.8 | -20.8 | -8.6 | -3.7 | -23.9 |
| J_{23} | 3.15 | 3.18 | -14.9 | -2.5 | -9.2 | -26.8 | -31.3 | -23.5 | -31.0 |
| J_{34} | 3.17 | 3.17 | +10.9 | +6.3 | +7.0 | 50.5 | 8.1 | 44.0 | 57.6 |
| J_{45} | 3.18 | 3.15 | +9.2 | +5.4 | +8.0 | 56.9 | 5.3 | 54.1 | 45.9 |
| J_{56} | 3.20 | 3.21 | -5.4 | -5.9 | -5.0 | -13.6 | -5.4 | -14.2 | -35.5 |

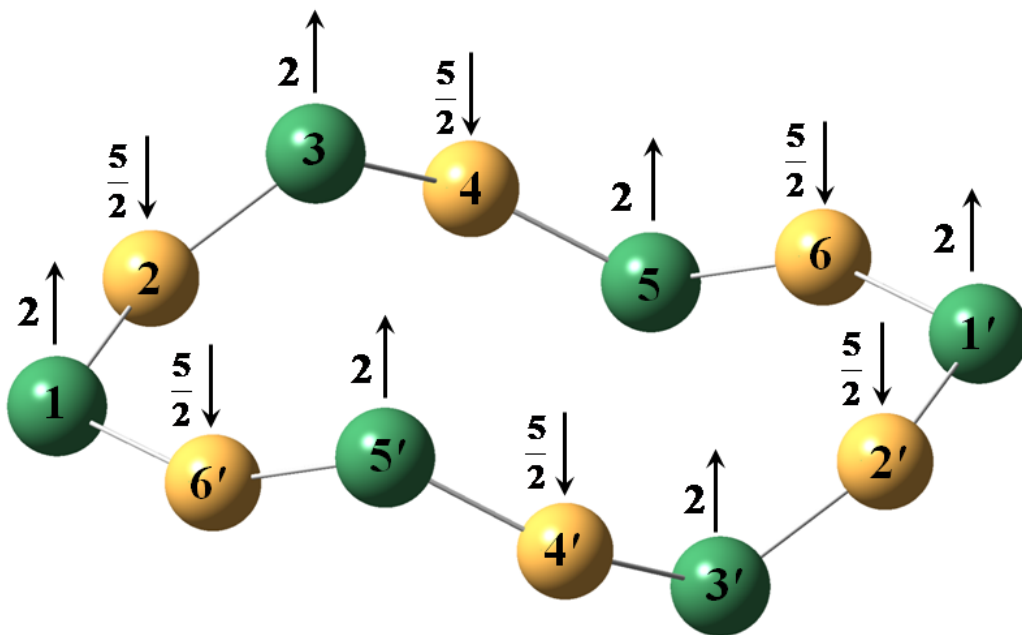


Figure 4-2: Schematic diagram of magnetic coupling in Mn12 wheels, number in italics (1-6 and 1'-6') and other numbers are for individual spin. $\text{Mn}^{+3}(S=2)$ green and $\text{Mn}^{+2}(S=5/2)$ orange-yellow

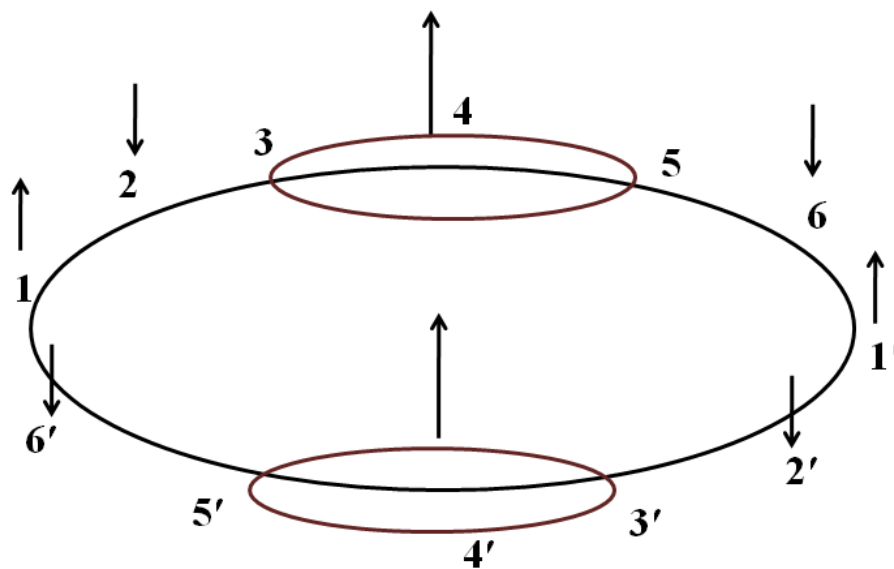


Figure 4-3: Schematic for antiferromagnetic Mn12 wheels

Table 4-4: Löwdin Population analysis for Mn₁₂(Mdea) and Mn₁₂(Adea)

| | Mdea | Adea |
|-------------------|-------|-------|
| Mn(1),Mn(3),Mn(5) | 3.89 | 3.92 |
| Mn(2), Mn(6) | -4.75 | -4.76 |
| Mn(4) | 4.77 | 4.77 |
| N _{Oh} | 0.06 | 0.05 |
| N _{PBP} | 0.02 | 0.02 |
| OAc | 0.02 | 0.02 |
| μ-O | 0.02 | 0.02 |

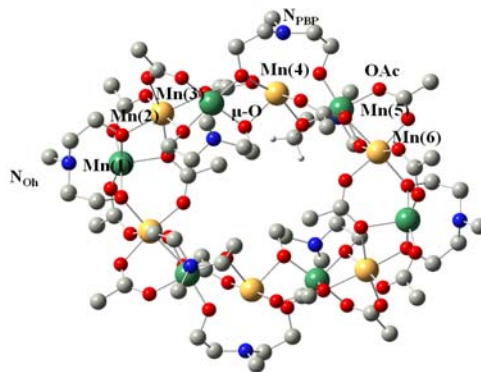


Figure 4-4: Density of states plotted for Mn₁₂(Mdea) in S=7 ground state. Positive values present spin up, and negative values present spin down densities.

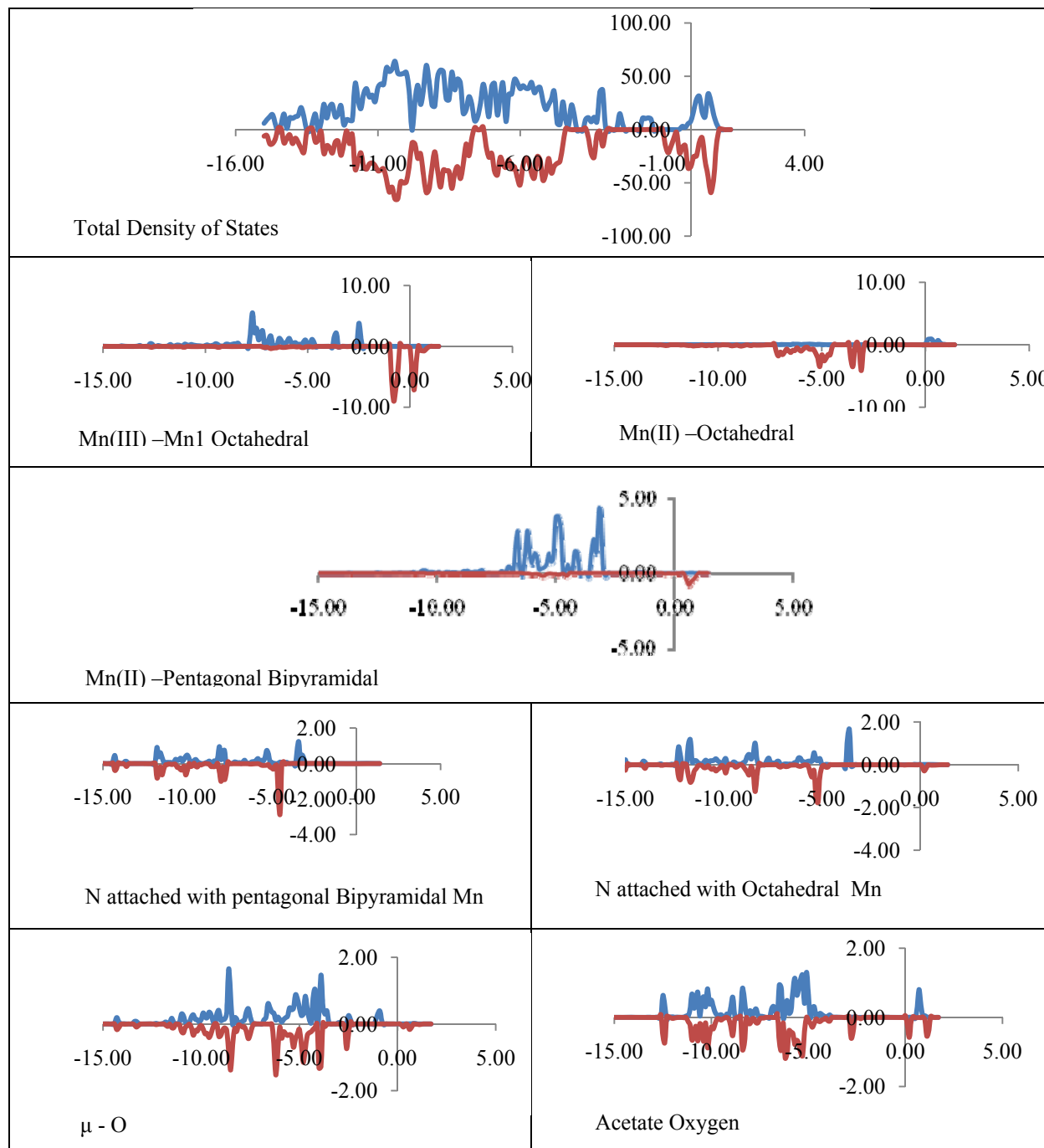


Figure 4-5: Density of states plotted for Mn₁₂(Adea) in S=7 ground state.

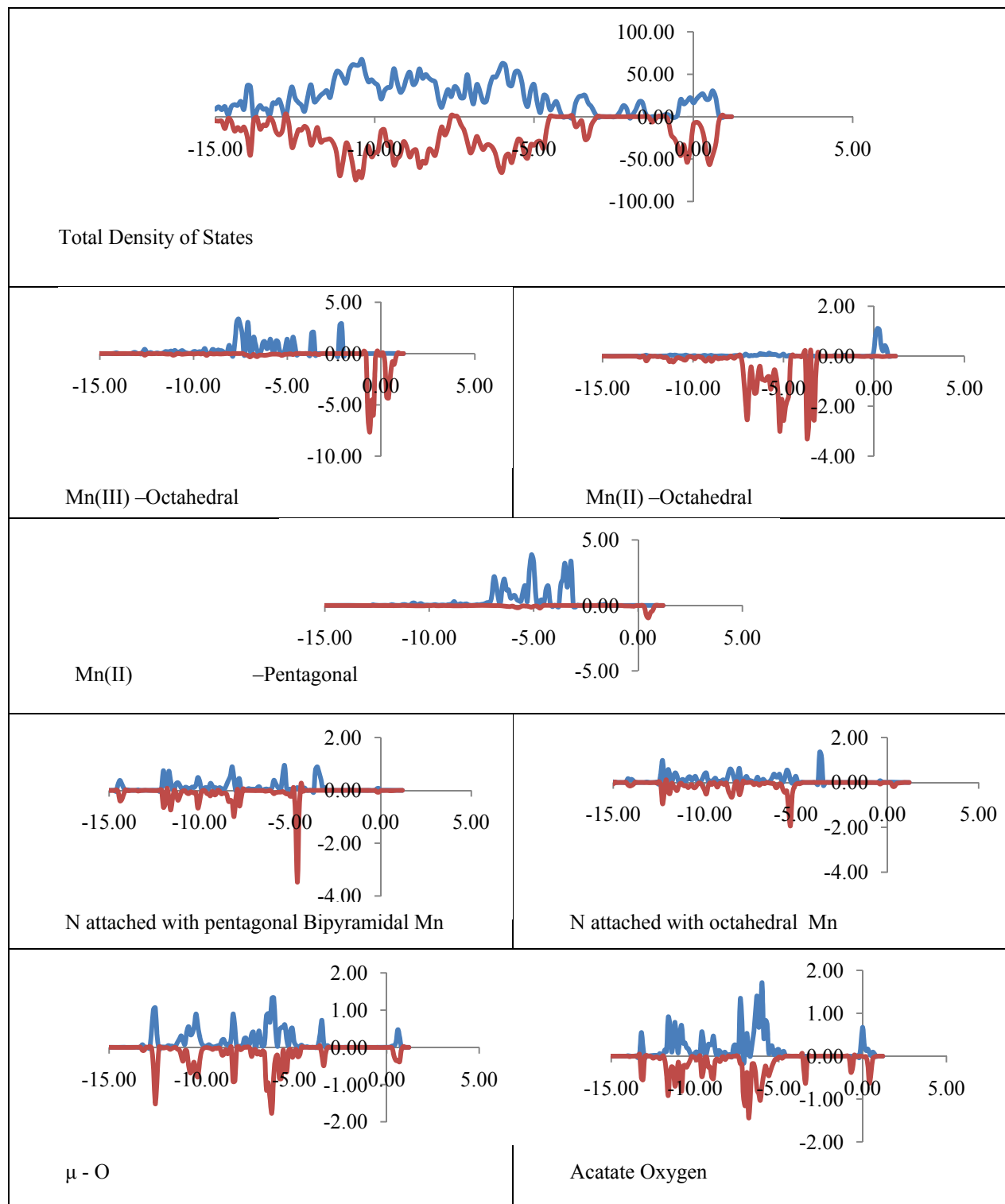


Figure 4-6: PDOS diagram for d orbitals localized Mn(1) and Mn(3) for Mn12 wheels, the upper row is showing PDOS result for Mn₁₂(Mdea) and down row showing Mn₁₂(Adea) wheel results

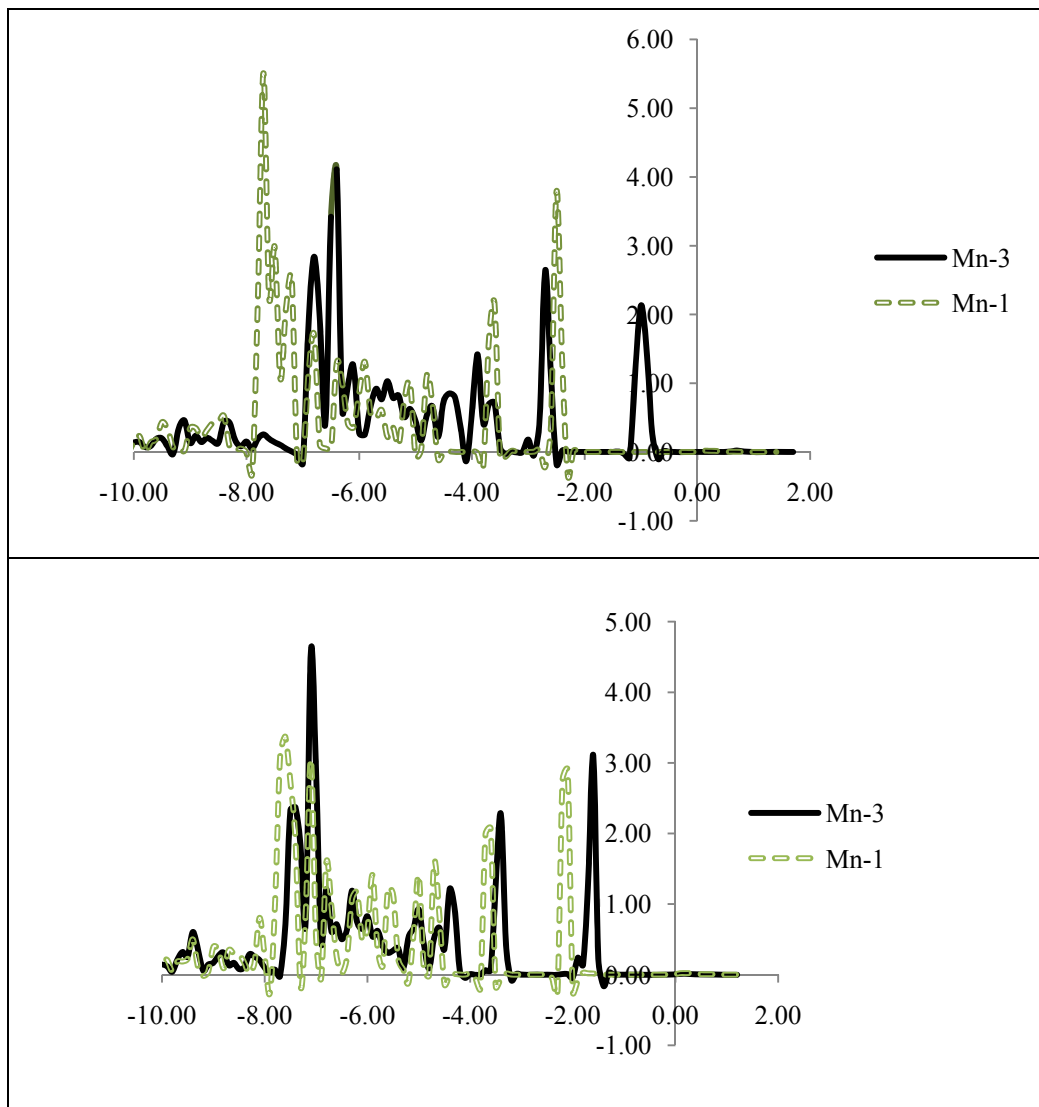
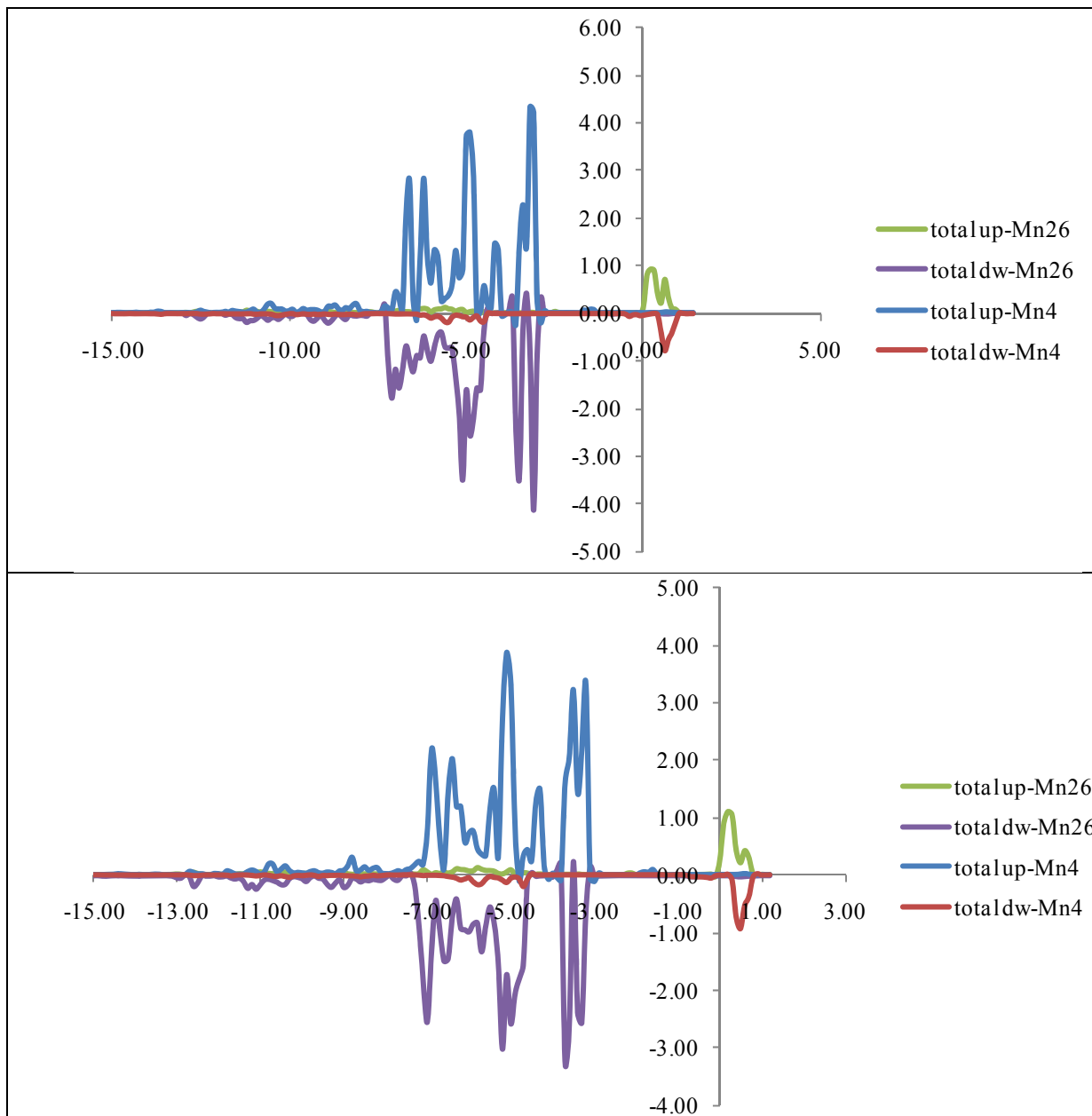


Figure 4-7: PDOS diagram for d orbitals localized on Mn(2,6) and Mn(4) for Mn₁₂ wheels, the up row is showing PDOS result for Mn₁₂(Mdea) and down row is showing Mn₁₂(Adea) wheel results.



Scheme 4-1 Computational calculation scheme for six Heisenberg exchange constants in Mn12 based wheels. (S=0)_{nm} is referring the spin alignment used for calculating corresponding J_{nm} . The symbol 1, 3, 5 and (1□, 3□, 5□) are Mn+3 and 2, 4, 6 and (2□, 4□, 6□) are presenting Mn+2 having four and five unpaired electrons respectively. Here i is presenting spin up and i is showing spin down orientation (i=1-6 and 1□-6□).

| | (S=0) _{nm} | Ground Spin state (S=7) |
|---------------------|--|--|
| (S=0) ₁₆ | $\left(\begin{array}{c} \underline{1} - \underline{2} - \underline{3} - \underline{4} - \underline{5} - \underline{6} \\ \underline{6}' - \underline{5}' - \underline{4}' - \underline{3}' - \underline{2}' - \underline{1}' \end{array} \right)$ | $\left(\begin{array}{c} \underline{1} - \underline{2} - \underline{3} - \underline{4} - \underline{5} - \underline{6} \\ \underline{6}' - \underline{5}' - \underline{4}' - \underline{3}' - \underline{2}' - \underline{1}' \end{array} \right)$ |
| (S=0) ₁₂ | $\left(\begin{array}{c} \underline{1} - \underline{2} - \underline{3} - \underline{4} - \underline{5} - \underline{6} \\ \underline{6}' - \underline{5}' - \underline{4}' - \underline{3}' - \underline{2}' - \underline{1}' \end{array} \right)$ | |
| (S=0) ₂₃ | $\left(\begin{array}{c} \underline{1} - \underline{2} - \underline{3} - \underline{4} - \underline{5} - \underline{6} \\ \underline{6}' - \underline{5}' - \underline{4}' - \underline{3}' - \underline{2}' - \underline{1}' \end{array} \right)$ | |
| (S=0) ₃₄ | $\left(\begin{array}{c} \underline{1} - \underline{2} - \underline{3} - \underline{4} - \underline{5} - \underline{6} \\ \underline{6}' - \underline{5}' - \underline{4}' - \underline{3}' - \underline{2}' - \underline{1}' \end{array} \right)$ | |
| (S=0) ₄₅ | $\left(\begin{array}{c} \underline{1} - \underline{2} - \underline{3} - \underline{4} - \underline{5} - \underline{6} \\ \underline{6}' - \underline{5}' - \underline{4}' - \underline{3}' - \underline{2}' - \underline{1}' \end{array} \right)$ | |
| (S=0) ₅₆ | $\left(\begin{array}{c} \underline{1} - \underline{2} - \underline{3} - \underline{4} - \underline{5} - \underline{6} \\ \underline{6}' - \underline{5}' - \underline{4}' - \underline{3}' - \underline{2}' - \underline{1}' \end{array} \right)$ | |

4.7 Density Functional Theory study of Mn9 based single molecule magnet

Next we calculated Heisenberg exchange constant for a new mixed-valent Mn9 single-molecule magnet. The fused triangle in this molecule induce a ligand engineered spin frustration. The compound [MnIII₈MnIIO₃(OMe) (O₂CCMe₃)₇(edte)(edteH)₂(N₃)₂] (Figure 4-4) uses a potentially hexadentated edteH₄ ligand, The reaction of edteH₄ with Mn(O₂CCMe₃)₂ in presence of NEt₃ and NaN₃ afforded this new Mn9 compound with an unprecedented structural core

Where [edteH₄=(HOCH₂CH₂)₂NCH₂CH₂N(CH₂CH₂OH)₂=N,N,N',N'-tetrakis-(2-hydroxyethyl) ethylenediamine]. It can be considered as a series of triangular units connected back to back to create such a molecular ladder.

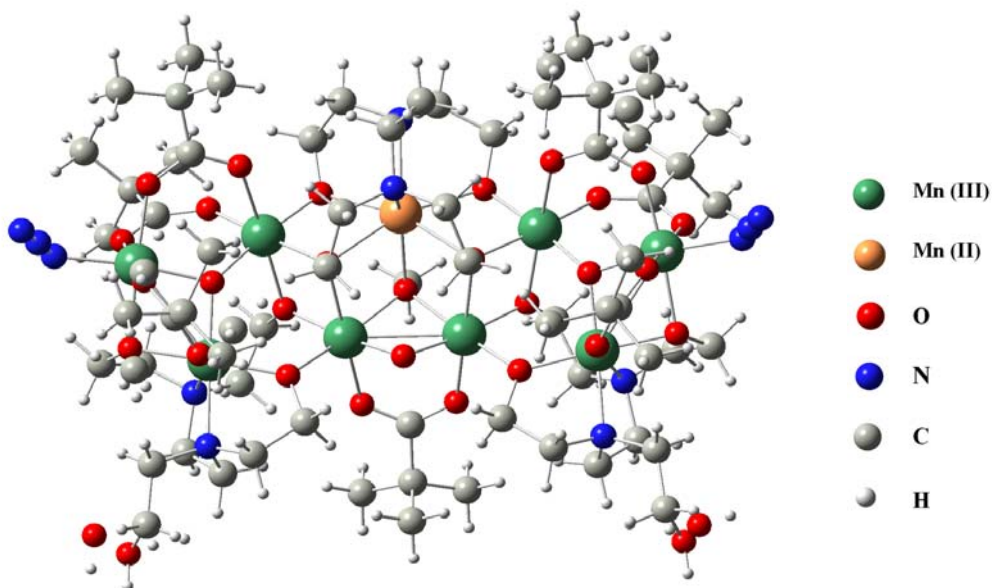


Figure 4-8: [Mn^{III}₈Mn^{II}O₃(OMe)(O₂CCMe₃)₇(edte)(edteH)₂(N₃)₂]

4.7.1 Determination of Ground Spin state of Mn9

The first step aim of DFT calculation was to predict correct ground spin arrangement in the molecule. From Inelastic Neutron Scattering (INS) data we can see the ground spin state has a multiplicity of 22. This value suggests that any two Mn⁺³ in this molecule are spin down and other seven are spin up. Starting from FM optimized geometry we found energy for 29 hypothetical spin states listed in Table 4-4 (atoms are labeled according to According to Figure 4-8). Since for Mn⁺³-Mn⁺³ and Mn⁺²-Mn⁺³ centers have relatively low magnetic exchange constants, we should expect small energy gaps between these hypothetical spin states. From the Table 4-5 one can see that the state with the lowest energy corresponds to the minority spin localized on Mn1 and Mn9 atoms, with total multiplicity consistent with the INS observation.

4.7.2 Heisenberg exchange constant in Mn9 system.

The Heisenberg Hamiltonian written assuming neglect of the second and higher neighbor magnetic interactions:

$$\hat{H} = -J_{13}S_1S_3 - J_{12}S_1S_2 - J_{24}S_2S_4 - J_{35}S_3S_5 - J_{34}S_3S_4 - J_{45}S_4S_5 - J_{23}S_2S_3 - J_{46}S_4S_6 \quad (4-6)$$

$$- J_{13}S_9S_7 - J_{12}S_9S_8 - J_{24}S_8S_6 - J_{35}S_7S_5 - J_{34}S_7S_6 - J_{45}S_6S_5 - J_{23}S_8S_7$$

Since the molecule is composed of two symmetry equivalent fragments, Mn1, Mn2, Mn3, Mn4 are equivalent to Mn9, Mn8, Mn7, and Mn6 respectively. This indicates the presence of eight inequivalent exchange interactions. The J values (apart from J_{46}) were calculated as direct energy differences between the spin states shown in columns 2 and 3 in Scheme 2:

$$J_{ij} = \frac{E_{SC_1} - E_{SC_2}}{S_i S_j}$$

(4-7)

here E_{SC_1} is the energy of $(S)_{ij}$ state from column 2, and E_{SC_2} from column 3. For example to calculate exchange constant between Mn1-Mn3 we take the energy difference between two hypothetical states, in one we have Mn1, Mn3 spin down, and in another Mn1 and Mn7 are spin down. To predict J_{46} we take the energy difference between two hypothetical spin states in one Mn2 and Mn4 are spin down, and in the other all Mn atoms are spin up. The energy difference is:

$$\Delta E = -8J_{12} - 8J_{34} - 10J_{45} - 8J_{23} - 8J_{46} \quad (4-8)$$

This equation was solved for J_{46} using J values obtained previously.

When only the first neighbor magnetic interactions are considered, Mn₉ topology consists of fused Mn₃ triangles, known to be susceptible to spin frustration, caused by competing exchange pathways. The ground spin state in Table 4-5 is characterized by the presence of two

AF couplings between Mn1/Mn3 and Mn1/Mn2, while the rest are FM. The calculated J_{12} (Mn1/Mn2) interactions in Table 4-6 are negative (AF) with spin couplings of c.a. -16.87 cm^{-1} , as expected for antiparallel alignments). The rest of the couplings (ranging from 1.14 cm^{-1} to 27.32 cm^{-1}) are FM.

Coupling for two multielectron spin centers was expressed by Clark and Davidson as:²¹²

$$J_{ij} = \frac{1}{2} [S_T(S_T + 1) - S_i(S_i + 1) - S_j(S_j + 1)] \quad (4-9)$$

where S_i and S_j coupled together to give a total spin S_T ($S_T = S_i + S_j$). One can compare J predicted by Eq.4-9 for two adjacent spins. For a $\text{Mn}^{+2}/\text{Mn}^{+3}$, and $\text{Mn}^{+3}/\text{Mn}^{+3}$ pairs aligned parallel, the spin couplings from Eq 4-9 are 5 and 4., respectively. The calculated J_{13} Mn1/Mn3 interactions in Table 4-6 are positive (ferromagnetic) with spin couplings of 7.48 cm^{-1} . However, the J_{13} (Mn1/Mn3) interactions of the Mn1Mn3, pair in Table 4-6 are ferromagnetic, and yet their J are very negative (-3.84 cm^{-1}). This means that these ferromagnetic interactions are completely frustrated, and the spins are aligned antiparallel. Here we can see the azide ligand induced spin frustration present in Mn1, Mn2, Mn3 containing triangle, showed in Figure 4-9.

Scheme 2: Computational calculation scheme for seven Heisenberg exchange constants in Mn₉ complex. The symbol 1, 2, 3, 4, 6,7,8,9 are Mn⁺³ and 5 is presenting Mn⁺² having four and five unpaired electrons respectively. Here \uparrow is presenting spin up and \downarrow is showing spin down orientation.

| | Spin configuration 1(SC ₁) | Spin configuration 2 (SC ₂) | $J_{ij} = \frac{E_{SC_1} - E_{SC_2}}{S_i S_j}$ (cm ⁻¹) |
|----------|--|---|---|
| J_{13} | | | 7.48 |
| J_{12} | | | -16.87 |
| J_{24} | | | 1.14 |
| J_{35} | | | 25.07 |
| J_{34} | | | 7.92 |
| J_{45} | | | 3.15 |
| J_{23} | | | 4.02 |

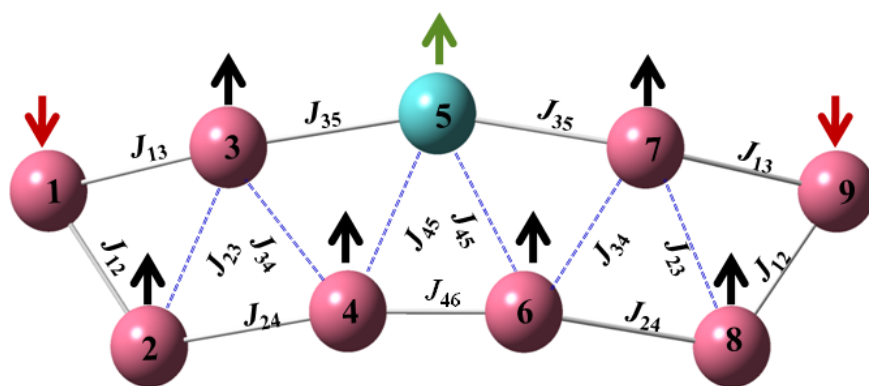
Table 4-5: Energy differences between different spin orientations in Mn9, first nine columns are presenting the spin of Mn atoms in different spin orientations labeled according to Figure 4-9, 10th column is multiplicity; the 11th column is energy difference in kcal/mol, from stable most spin state. The HS is designated where we have maximum possible multiplicity and all orientations are ferromagnetic, the multiplicity 28,22,20,12 are designated as IS, LS is describing the multiplicity 6, and suffix(s) are indicating the index of Mn according to Figure 4-9

| | S1 | S2 | S3 | S4 | S5 | S6 | S7 | S8 | S9 | M | ΔE |
|--------------------|----|----|----|----|------|----|----|----|----|----|------------|
| IS ₁₉ | -2 | 2 | 2 | 2 | 2.5 | 2 | 2 | 2 | -2 | 22 | 0.000 |
| IS ₂₉ | 2 | -2 | 2 | 2 | 2.5 | 2 | 2 | 2 | -2 | 22 | 0.069 |
| IS ₁₈ | -2 | 2 | 2 | 2 | 2.5 | 2 | 2 | -2 | 2 | 22 | 0.139 |
| HS | 2 | 2 | 2 | 2 | 2.5 | 2 | 2 | 2 | 2 | 38 | 0.188 |
| IS ₂₈ | 2 | -2 | 2 | 2 | 2.5 | 2 | 2 | -2 | 2 | 22 | 0.215 |
| LS ₂₄₆₈ | 2 | -2 | 2 | -2 | 2.5 | -2 | 2 | -2 | 2 | 6 | 0.696 |
| IS ₄₆ | 2 | 2 | 2 | -2 | 2.5 | -2 | 2 | 2 | 2 | 22 | 0.891 |
| IS ₁₂ | -2 | -2 | 2 | 2 | 2.5 | 2 | 2 | 2 | 2 | 22 | 0.912 |
| IS ₁₃ | -2 | 2 | -2 | 2 | 2.5 | 2 | 2 | 2 | 2 | 22 | 1.128 |
| IS ₂₃ | 2 | -2 | -2 | 2 | 2.5 | 2 | 2 | 2 | 2 | 22 | 1.373 |
| LS ₁₂₈₉ | -2 | -2 | 2 | 2 | 2.5 | 2 | 2 | -2 | -2 | 6 | 1.428 |
| IS ₃₉ | 2 | 2 | -2 | 2 | 2.5 | 2 | 2 | 2 | -2 | 22 | 1.448 |
| IS ₁₇ | -2 | 2 | 2 | 2 | 2.5 | 2 | -2 | 2 | 2 | 22 | 1.471 |
| IS ₂₄ | 2 | -2 | 2 | -2 | 2.5 | 2 | 2 | 2 | 2 | 22 | 1.544 |
| IS ₁₆ | -2 | 2 | 2 | 2 | 2.5 | -2 | 2 | 2 | 2 | 22 | 1.552 |
| LS ₂₃₄₆ | 2 | -2 | -2 | -2 | 2.5 | -2 | 2 | 2 | 2 | 6 | 1.554 |
| IS ₂₇ | 2 | -2 | 2 | 2 | 2.5 | 2 | -2 | 2 | 2 | 22 | 1.557 |
| IS ₂₆ | 2 | -2 | 2 | 2 | 2.5 | -2 | 2 | 2 | 2 | 22 | 1.596 |
| IS ₂₅ | 2 | -2 | 2 | 2 | -2.5 | 2 | 2 | -2 | 2 | 20 | 1.720 |
| IS ₁₅ | -2 | 2 | 2 | 2 | -2.5 | 2 | 2 | 2 | -2 | 20 | 1.762 |
| IS ₅ | 2 | 2 | 2 | 2 | -2.5 | 2 | 2 | 2 | 2 | 28 | 1.885 |
| IS ₃₅ | 2 | 2 | -2 | 2 | -2.5 | 2 | 2 | 2 | 2 | 20 | 1.941 |
| IS ₃₅₇ | 2 | 2 | -2 | 2 | -2.5 | 2 | -2 | 2 | 2 | 12 | 1.983 |
| IS ₄₅₆ | 2 | 2 | 2 | -2 | -2.5 | -2 | 2 | 2 | 2 | 12 | 2.020 |
| IS ₄₅₉ | 2 | 2 | 2 | -2 | -2.5 | 2 | 2 | 2 | -2 | 12 | 2.578 |
| IS ₃₄ | 2 | 2 | -2 | -2 | 2.5 | 2 | 2 | 2 | 2 | 22 | 2.658 |
| IS ₁₅₆ | -2 | 2 | 2 | 2 | -2.5 | -2 | 2 | 2 | 2 | 12 | 2.987 |
| IS ₃₇ | 2 | 2 | -2 | 2 | 2.5 | 2 | -2 | 2 | 2 | 22 | 3.019 |
| IS ₃₆ | 2 | 2 | -2 | 2 | 2.5 | -2 | 2 | 2 | 2 | 22 | 3.020 |

Table 4-6: Heisenberg exchange constant for two adjacent metal centers, first column is the Heisenberg exchange constant labeled according to Figure 4-9, next column is distance between Mn_i and Mn_j , the third one is Heisenberg exchange constant, and fourth and fifth column is calculated and ideal spin coupling according to eq (4-7)

| | Mn_i-Mn_j Å | J cm^{-1} | $\langle S_i S_j \rangle_{calc}$ | $\langle S_i S_j \rangle_{ideal}$ |
|----------|------------------|------------------|------------------------------------|-------------------------------------|
| J_{13} | 3.35 | 7.48 | -3.84 | -4 |
| J_{12} | 2.95 | -16.87 | -3.82 | -4 |
| J_{24} | 3.43 | 1.14 | 3.84 | 4 |
| J_{35} | 3.33 | 25.07 | 4.70 | 5 |
| J_{34} | 3.21 | 7.92 | 3.82 | 4 |
| J_{45} | 3.38 | 3.15 | 3.84 | 5 |
| J_{23} | 3.46 | 4.02 | 3.84 | 4 |
| J_{46} | 2.86 | 27.32 | 3.82 | 4 |

Figure 4-9: Schematic diagram of magnetic coupling in Mn_9 in ground state, the green ball is Mn^{+3} and pink is for Mn^{+2} . Atom 4, 5, 6 is forming an isosceles triangle.



CHAPTER 5 HYBRID DENSITY FUNCTIONAL THEORY STUDIES OF STRUCTURE AND PROPERTIES OF CERIA NANOPARTICLES.I. LATTICE PARAMETERS AND BULK MODULI

5.1 Cerium oxides and its property

Unique chemical and electronic properties of the mixed cerium oxide, generally known as ceria, make it an important material for number of applications. Ceria is used as a catalyst for various chemical processes, including production and purification of hydrogen,²¹³ and carbon monoxide removal from the automobile exhaust.²¹⁴ Mobility of oxygen vacancies and consequently high ionic conductivity makes ceria a promising electrolyte for solid oxide fuel cells.²¹⁵ Electronic structure of ceria leads to its use as UV absorber in cosmetic industry and manufacturing of glass windows.⁸¹ It is also used in light harvesting devices and optical displays.⁸¹ In most of the process the oxygen vacancies play essential role.

Bulk cerium oxide has at least two stable stoichiometries, the dioxide (CeO_2) and dicerium trioxide which is commonly referred as sesquioxide (Ce_2O_3). At ambient conditions dioxide forms CaF_2 (fluorite) type structure in face centered cubic space group $Fm-3m$ with the lattice parameter of 5.411\AA .²¹⁶ In that structure cerium ions occupy the vertices and faces of cubic unit cell. Each Ce(IV) is coordinated with eight oxygen ions arranged in a perfect cube, while each oxygen ion is surrounded by four cerium ions in tetrahedral arrangement. This structure is often described as cubic closed packing (*ccp*) of Cerium ions with oxygen ions occupying all tetrahedral holes. At the elevated pressure (31 GPa and room temperature) cerium dioxide undergoes phase transition from fluorite to $\alpha\text{-PbCl}_2$ structure type with orthorhombic space group $Pnam$.⁷² Another structural type ($\delta\text{-Ni}_2\text{Si}$) had also been suggested. Both $\alpha\text{-PbCl}_2$

and δ -Ni₂Si types have similar positions of Ce ions and only differ in the position of oxygen ions. Neither Raman spectroscopy, nor X-ray diffraction are sensitive enough to the the position of of light oxygen ions in the presence heavy ones, so the direct evidence is missing. However, based on axial ratios, high pressure polymorph of cerium dioxide was found more unlikely to belong to α -PbCl₂ structural type.²¹⁷ In α -PbCl₂ type structure seven anions at roughly the same separation and two at a slightly larger separation from the cation, which is denoted as [7+2] coordination. There are two anion coordinations, one of which is four coordinate and the other is five coordinate.²¹⁷

At 300⁰C cerium dioxide is stable in bulk at partial oxygen pressure down to 10⁻⁴⁰ atm. Cerium sesquioxide Ce₂O₃ had been reported to form at same temperature and in between 10⁻⁹⁸ atm to 10⁻⁴⁰ atm.⁷⁰ Similar to other trivalent lanthanide oxides, Ce(III) oxide was found to have two different crystal structures: one is A type with nearly hexagonal close packing to Ce ions (*hcp*), and the other is C type with body centered cubic (*bcc*) packing of Ce ions. Barnighausen and Schiller reported²¹⁸ structure determination for A type cerium sesquioxide from single-crystal X-ray diffraction study. Amber colored well-shaped plate-like crystals were obtained by heating a mixture of LiCeO₂, CeO₂, and anhydrous LiCl in a closed steel crucible temperatures between 700-800⁰C for several weeks. It has *P-32/m1* space group with the lattice parameters a=3.891Å and c=6.059Å.²¹⁸ In the type A structure every metal ion is coordinated with seven oxygen ions; four oxygen ions are closer than other three. The former are five-coordinated and the latter are four-coordinated.

C type Ce₂O₃ structure is formed at room temperature in a few hours on the surfaces of the Ce metal left in the air.²¹⁹ The C type has space group *Ia3* with the lattice parameter of 11.16

Å. Its unit cell contains 32 metal ions and 48 oxygen ions. The existence of type C cerium sesquioxide in bulk is controversial. However, X-ray diffraction study of nanopowder with particles below certain size indicates C type structure. An X-ray photo-electron spectroscopic study reports the lattice parameter of nanoscale sesquioxide to be 5.61 Å, just half of C type unit cell⁸¹. From this evidence one may conclude that type C cerium sesquioxide may only exist in the nanoparticle form. It is recognized that from A type sesquioxide to dioxide conversion is so exothermic spontaneous ignition was often observed, CeO₂ hardly dissolved in acids and alkali but reacts with water.²²⁰

Ceria NPs (nanoceria) had been extensively studied since early 1970s, but for inadequate characterization facility those cannot be properly characterized, in recent years with the development of experimental techniques as well as the help of theoretical studies this area is much widely explored. In a review article it is told that from June 1993 to end of 1998, there was 560 paper had been published.⁶⁷ Basically in theoretical field from mid 1990 simulated annealing and interionic potentials are used to investigate the structure and reductability of intermediate valance ceria nanoparticle.⁶⁸ The most applications of nanocrystalline ceria are based on its oxygen storage capacity and electronic properties. Although CeO₂ has a wide band gap of 6 eV⁶⁹ and acts as an insulator, in the higher temperature region (300⁰C-400⁰C) and in reduced oxidation state it demonstrates an enhancement of the electric conductivity,⁶⁰ which is a disadvantage for some applications. Adachi in his review referred that composite contained nano particle 4.1nm having band gap 3.42 eV and with 5.37nm nanoparticle it is 3.37eV.⁷⁰

Like bulk ceria nano cerium dioxide also exhibit phase transition from fluorite phase to orthorhombic phase , the lattice papmeter of the orthorhombic phase is a=5.641Å, b=6.647Å,

$c=3.481\text{\AA}$, but the difference is nano cerium dioxide shows bulk modulus 328 ± 12 GPa ⁷¹ in contrast with bulk cerium dioxide 230 GPa. The phase transition pressure (22.3 GPa) is also very low compared with bulk one (31 GPa), ⁷² this observation is quite anomalous with other nano oxide and sulfides , the author suggested that larger volume collapse and existence of unstable high pressure phase is responsible for the decrease of transition pressure of nano cerium dioxide compared with bulk. ⁷¹

Nanoceria used in design a three way catalyst for automobile exhaust, ⁷³ since ceria catalytically oxidizes hydrocarbons to water, carbon monoxide to dioxide and nitrogen oxides to nitrogen. Ceria NPs are also used for water gas shift, steam reforming reaction, and carbon monoxide removal. ⁷³ The oxygen vacancies play an important role for the catalytic activity of ceria. Zirconia doped ceria ($\text{CeO}_2/\text{ZrO}_2$ solid solution) can operate at relatively lower temperature around 600°C than pure ceria catalyst. ⁷⁴

5.2 Structural relations between cerium oxides.

To illustrate the relationship between fluorite and other structural types of ceria it is advantageous to consider it in hexagonal aspect. ²²¹ One can start with hexagonal close-packed layers of Cerium ions, then sandwich them between two hexagonal layers of O ions (one on each side) in ABC motif. In this construct (called thereafter "sandwich trilayer") Ce ions have octahedral coordination, compressed along 3-fold symmetry axis in the real structure (Figure 5-2). Three dimensional fluorite structure is then formed by stacking of these sandwich trilayers (Figure 5-3). If only Ce layers are considered, they form ABC packing (the cubic structure). If both Ce and O layers are considered, the stacking can be described as **CABABCBCA** (Ce layers are marked in bold). Upon this stacking distorted octahedral coordination of each Ce ion is

extended with two O ions from neighboring sandwich layers (one on each side) so that ideal cube is formed. Besides geometric, this description of cerium dioxide structure has a physical meaning. Stoichiometric (111) surface, formed by intact sandwich trilayer, is found to be thermodynamically the most stable one.²¹⁹ It represents the major fraction of the active surface in catalytic nanocrystallites.⁷⁴ Zero charge and dipole moment of sandwich trilayer may be an important factor, contributing to the stability of (111) surface.

The relation between the cubic and the orthorhombic phases of dioxide can be described as combination of shift and distortion of the sandwich trilayers. First, trilayers slide from **CABABCBCA** to **ABCABCABC** motif, so that the first coordination sphere of Ce loses one oxygen ion from each of two adjacent trilayers. Instead, the remaining coordination sphere of distorted octahedron is extended with six oxygen ions (three from each trilayer), at larger distances (secondary coordination sphere). Second, the Ce ions of the trilayer shift up and down in alternant pattern in order to include three of these new oxygen ions into the first coordination sphere, and oxygen layers are distorted to accommodate this shift.

Sesquioxide type A structure can be related to fluorite structure by removal of oxygen ions and shift. First, every other sandwich trilayer loses complete oxygen layer, and the structure is transformed from **CABABCBCA** to **CABABCvCA**, then layers of Ce shift from *bcc* to *hcp*, so that intact and defective trilayers merge into **ABCAB** sandwich pentalayer. Close packing of these pentalayers forms type A structure, and its most stable (001) surface. Just like trilayers of fluorite structure, five layers are electroneutral and nonpolar. These properties may contribute to the thermodynamic stability of (001) type A surface. Sandwich pentalayer can also be considered as a model for subsurface oxygen vacancy defects in dioxide surfaces.

Sesquioxide type C structure can also be described using sandwich trilayer model. If we take out one third oxygen from body diagonal of *ccp* structure of dioxide we can get a bcc sesquioxide, starting from *ccp* hexagonal sandwich structure if one of the 8th oxygen from up layer of oxygen and one from down layer is removed the type C sesquioxide can be brought about. In structural transition from fluorite type dioxide to hexagonal the oxygen substructure of fluorite framework preserve intact but the metal ions are moved into interstitial position such that slabs of dioxide two ion layers are preserved but shear occurs at this regular intervals, the seven coordinate A type formed. For the C type sesquioxide if the one fourth of oxygen have removed from dioxide along the nonintersecting strings in the four $\langle 111 \rangle$ directions such that every ions are six coordinate.²¹⁶ The structural conversion from face center cubic (tetravalent cerium body center cubic (trivalent cerium) does not require crystal structure change, basically by removal of 1/4th oxygen along body diagonal converted *fcc* structure to *bcc* one.²¹⁶

When two solid phases coexist, lattice mismatch is an important parameter to consider. In order to find the lattice mismatch, we need to find a similar description for both dioxide and sesquioxide. The cerium dioxide lattice parameter in hexagonal aspect (i.e. translation vector of the sandwich bilayer) is 3.826Å to be compared with 3.891Å lattice parameter of the sesquioxide (1.7% expansion). The double lattice parameter along the hexagonal axis for cerium dioxide is 6.248Å to be compared with triple lattice parameter for sesquioxide equal to 6.059Å (3.0% contraction upon removal of one out of four oxygen atoms). Thus, the volume of the hexagonal unit cell is increased by 0.3%, which corresponds to 0.017% of lattice parameter increase. Therefore, random formation of oxygen vacancies is insufficient to explain the observed 0.6% increase of the lattice parameter in small ceria nanoparticles.

Sesquioxide type C structure can also be described using sandwich trilayer model instead of completely removal one of four hexagonal closed packed oxygen layer as it happens in type A one out of four oxygen removed from each closed pack layer they are forming vacancies are aggregated in tetramers, comparing with vacancies described in ⁵⁶ we observed a different vacancy structure in the surface of bulk c type sesquioxide, In our model we observed four vacancies on the one surface, cluster together (Figure 5-6) where as the vacancies described by Esch and co worker ⁵⁶(Figure 5-7) said vacancies formed in trimer and dimer cluster, and the dimer vacancy generates by the combination of surface and subsurface vacancies the trimer uses one more sub surface layer in addition to two layer used in dimer vacancy. ⁵⁶ If we take out one third oxygen from body diagonal of *ccp* structure of dioxide we can get a bcc sesquioxide, starting from *ccp* hexagonal sandwich structure if one of the 8th oxygen from up layer of oxygen and one from down layer is removed the type C sesquioxide can be brought about. In structural transition from fluorite type dioxide to hexagonal the oxygen substructure of fluorite framework preserve intact but the metal ions are moved into interstitial position such that slabs of dioxide two ion layers are preserved but shear occurs at this regular intervals, the seven coordinate A type formed. For the C type sesquioxide if the one fourth of oxygen have removed from dioxide along the nonintersecting strings in the four <111> directions such that every ions are six coordinate. ²¹⁶

5.3 First Principles studies of Ceria published to date

Theoretical description of ceria presents a challenge because of *4f*-electron in Ce(+3) ion. Two different approaches have been developed in order to treat the ground state electronic structure. In the first cerium is seen as tetravalent with an unoccupied *4f* band and a completely

filled O 2p-band.⁶⁹ The second model considers the ground state of ceria to be a mixture of two Ce configurations, $4f^0$ and $4f^1$ with a filled oxygen 2p valence band in the latter.²²² In this model cerium is no longer tetravalent.

First principle studies on cerium oxide(s) can be categorized in three broad sections, first one is bulk crystalline cerium oxides, second one is nanocrystalline ceria cluster, and ceria surface. For later two sections mainly used plane wave DFT because of computational expense, where effects of strong electronic correlation of Ce 4f states are taken into account through the use of an effective on-site Coulomb repulsive interaction within DFT+U approach. Vacancy formation study on nanocrystalline CeO_{2-x} in comparison with corresponding results for bulk and (111) CeO₂ surface has been reported by Inebaev *et al.*,²²³⁻²²⁵ Loschen and coworkers²²⁶⁻²²⁸ and others.²²⁹⁻²³¹ Oxygen transport and oxygen-vacancy formation energy in ceria were explained on the basis of first-principles quantum mechanical simulations performed by Skorodumova *et al.*²³² First-principle²³³ molecular orbital calculation using discrete-variational (DV)-X alpha method on a model of CeO₂([CeO₈](12-)), and compare them with experimental data on X-ray absorption-near-edge structure. The adsorption properties Shapovalov *et al.* showed²³⁴ DFT calculations to examine CO oxidation by CeO₂(111) surface doped with Au and compare the activity of the doped oxide with that of the pure oxide surface. Song YQ *et al.*²³⁵ electronic structure and magnetic properties of Co-doped CeO₂ on Si(111) are theoretically investigated by first principles calculations based on the DFT + U methods, Pd on CeO₂ (111) reported by Zhan-Sheng *et al.*²³⁶ Au on the (110) surfaces of CeO₂ and Zr-doped CeO₂ published by Wei and co workers²³⁷ using (DFT+ U). There are other DFT study of absorption on ceria surface were also reported.²³⁸⁻²⁴⁶

A number of studies of ceria have been concerned with elucidating the role of Ce $4f$ -electrons. In early SCF band calculations of bulk ceria Koelling *et al.*²⁴⁷ concluded that some covalent bonding is present, so that ceria is not completely ionic. Fujimori also concluded that the partial occupancy of the Ce $4f$ -states is present²²², corresponding to the second model above. However, Wuilloud *et al.*⁶⁹ and Watchter *et al.*²⁴⁸ have concluded that the cerium $4f$ states in CeO₂ are fully unoccupied and localized, corresponding to the first model above.

In the study of the electronic property of the bulk ceria, with Hartree-Fock theory, Hill and Catlow (who used the minimal basis set for cerium and oxygen)²⁴⁹ and Gennard *et al.*²⁵⁰ (who used more extended basis set) have neglected completely the Ce $4f$ basis functions, under the assumption that doing so does not affect the bulk properties of ceria, since the Ce $4f$ orbitals are assumed to be unoccupied. These studies found that the bulk properties of ceria can be well described even without the $4f$ electrons, indicating the validity of the first model. Recent density functional theory calculations of bulk CeO₂ and Ce₂O₃ were presented by Skrodumova *et al.*,²⁵¹ in the full potential linear muffin tin orbital (FP-LMTO) method. The best agreement with experiment for CeO₂ was obtained by treating the cerium $4f$ -functions as a part of the valence region. However, in studying fully reduced ceria, Ce₂O₃, the same authors found that in order for the Cerium $4f$ electrons to be correctly localized, they had to be treated in the core states. Treating the $4f$ electrons as valence electrons, resulted in an incorrect partially filled f -band at the Fermi level. Choosing the f electrons to be core or valence depending on the problem at hand is clearly not a satisfactory way of understanding the electronic structure of ceria. Watson *et al.*²⁵² studied the surfaces using the DFT+U methodology to describe the failing of DFT for (100) plane and demonstrate the presence of unoccupied cerium $4f$ states above the Fermi level⁵⁶. Esch

and coworker showed that the vacancies on CeO₂ (111) are immobile at room temperature, but linear clusters of these vacancies form at higher temperature.⁵⁶ They also show that one subsurface oxygen vacancy is required to nucleate each vacancy cluster⁵⁶ have studied the surface energies and the structures of the (111), (110) and (100) surfaces using DFT.

Hay *et al.*²⁵³ criticized LDA and GGA density functional theory methods for having a tendency to overdelocalize electrons and incorrectly predicting metallic properties for many semiconducting metal oxides and found that meta-GGA methods suffer the same drawback. They also criticized Core-*4f* and DFT+U approaches for artificially constraining *4f*-electrons to be localized. Instead, Hay *et al.* applied a new HSE functional, combining GGA-type Perdew-Burke-Eisenhoff (PBE) functional for the regions far from the nuclei, and hybrid PBE1PBE functional, including fraction of Hartree-Fock exchange close to the nuclei. As a result, an accurate description of both Ce(+4) and Ce(+3) oxides had been achieved. Here we build upon their success and show how the numerical accuracy can be increased, while improving the computational efficiency.

5.4 Computational Details

We aim at accurate description of the catalytic processes on the nanoceria surface. Therefore, for this study we selected BMK (Boese-Martin for Kinetics), a hybrid exchange-correlation functional, designed²⁵⁴ to describe kinetics of the chemical reactions (more specifically, transition states energies) without compromising the energies of equilibrium structures. We also use standard PBE1PBE exchange-correlation functional for comparison purposes. This hybrid functional uses Perdew–Burke–Ernezerhof (PBE) correlation, while 25%

of exchange energy is replaced by Hartree-Fock exchange.²⁵⁵ Spin-polarized (unrestricted) DFT calculations were used throughout.

DFT calculations were performed with the periodic boundary condition (PBC) of Kudin and Scuseria²⁵⁶ implemented in the Gaussian 03 program.²⁵⁷ For exchange evaluation, 27 cells (3×3×3 supercell) were used, which was found sufficient to describe the 5*f* actinide oxides (uranium dioxide and plutonium di- and sesquioxide).^{258,259} Ce ion has been described with medium-size relativistic effective core potential and Gaussian 03²⁵⁷ basis set²⁶⁰⁻²⁶² where 12 electrons occupying 5*s*, 5*p*, 5*d*, 6*s*, and 4*f* orbitals are treated explicitly and 46 of the electrons are treated as core.²⁶⁰ The diffused primitive functions (with exponents less than 0.2) were removed from each s, p, and d basis functions) from the original basis set. For oxygen Pople's 6-31G basis was used and all the electrons were described explicitly.

Unit cell for Ce₂O₃ was doubled to contain two cerium ions in order to describe antiferromagnetic coupling between *f*-electrons localized on different Ce ions. The spin-parallel (ferromagnetically coupled) state of Ce₂O₃ was found to be less stable by Hay *et al.*²⁵³ The lattice parameter ratio *a/c* was fixed at the experimental value. Unit cell for CeO₂ was also doubled in order to use the same cutoffs. Lattice energy was obtained in a series of single-point calculations and the optimum values of the lattice parameter *a*₀ (related to unit cell volume *V*₀), bulk modulus *B*₀ and bulk module pressure derivative *B*₀' were obtained by least-square fit of the energies to Birch-Murnaghan equation^{263,264} in its integrated form.²⁶⁵

A special care had to be taken to generate the initial guess. While the default guess obtained by diagonalization of Harris functional was sufficient for CeO₂ with no *f*-electrons, for Ce₂O₃ it leads to SCF convergence problems due to near degeneracy of seven *f*-states. Instead of method

used by Hay *et al.*²⁵³ (patching density matrix of initial guess with density matrices of oriented isolated ions), we prepared the initial guess using ionic cluster. The cluster was built from the content of the unit cell with oxygen ions moved away by translations to eliminate covalent bonding. Two Ce ions were placed in a crystal field (surrounded by negative point charges simulating seven oxygen ions of the first coordination sphere). The initial solution was prepared using Stable=Opt to destroy spin symmetry. The resulting Kohn-Sham orbitals were examined using graphical package Molden,²⁶⁶ and were found to contain two sets of *f*-AOs (one occupied and six unoccupied): alpha set was localized on one Ce ion, and beta set on the other one. Next, six other solutions were prepared by replacing the occupied *f*-AO with unoccupied ones using Guess=Alter and the resulting Fock matrices were used to generate the initial guess for 3D-periodical system in experimental geometry. The guess which resulted in lowest total energy was used for all other geometries.

5.5 Results and Discussions

The lattice parameters and bulk moduli for CeO₂ are reported in Table 5-1 and for Ce₂O₃ in Table 5-2. The results of published theoretical and experimental studies are also shown for comparison. For di- and sesquioxide structures our BMK results overestimate the lattice parameter by 0.9% and 0.3% (compare to 0.05% and 2.2% by HSE), a more systematic deviation which allows us to compare the lattice parameter trend upon subsurface vacancies formation. Bulk modulus for CeO₂ is in a good agreement with higher of the four experimental values reported.

The calculated bandgap 6.30eV for CeO₂ with BMK functional and 4.43eV with PBE1PBE functional 5.5 eV,⁶⁵ The calculated lattice parameter for CeO₂ in hexagonal aspect

(3.789Å) characterizes sandwich trilayer and can be directly compared to Ce₂O₃ lattice parameter a (3.880Å), characterizing sandwich pentalayer. If we assume that (111) surface of CeO₂ nanocrystals is covered with single Ce₂O₃ pentalayer (100% occurrence of subsurface vacancy), the lattice mismatch and variable bulk to surface ratio will be the only reason for changes in lattice parameter for the nanoceria. For the cubic nanoparticle of size d we can estimate the total number of Ce ions as $4*d^3/(5.41)^3$, i.e. 5456 for 6 nm NP. Taking the surface of pentalayer to be equal to sesquioxide lattice parameter c we find number of bulk Ce atoms to be $4*(d-6.05)^3/(5.41)^3$, i.e. 2776. Thus, for nanoparticle of 6 nm in size, surface to volume ratio is about 50%. Assuming Raoul's law for CeO₂/Ce₂O₃ solution (or, alternatively, the additivity of the surface and bulk lattice energies), we can use the integrated Birch-Murnaghan equation to find the compromise lattice parameter which minimizes the total energy of the nanocrystal (including both surface and bulk), and convert it into the cubic aspect. The resulting value of 3.812Å represents 0.6% expansion of the lattice parameter in 6nm nanoparticles of ceria, compared to the bulk lattice parameter. This value is in reasonable agreement with experimental 0.45% expansion and confirms the assumptions made in its derivation.

Table 5-1: Lattice parameter and bulk modulus of CeO₂ using different methods

| Method | a (Å) | Bulk modulus B ₀ (GPa) | Reference |
|----------------|----------------------|--|--|
| Hartree Fock | 5.385 | 357 | Hill ^a |
| LSDA | 5.37 | 193.4 | Jiang ^b |
| LSDA (Val 4f) | 5.39 | 214.7 | Skorodumova ^c |
| GGA (Val 4f) | 5.48 | 187.7 | Skorodumova ^c |
| PW91 | 5.45 | 193.5 | Yang ^d |
| LSDA | 5.360 | 104.3 | Hay ⁱ |
| LSDA (Core 4f) | 5.56 | 144.9 | Skorodumova ^c |
| GGA (Core 4f) | 5.69 | 128.9 | Skorodumova ^c |
| PBE | 5.468 | 171.1 | Hay ⁱ |
| TPSS | 5.449 | 183.0 | Hay ⁱ |
| HSE | 5.408 | 206.1 | Hay ⁱ |
| Experiment | 5.411 ²¹⁶ | 204 ²⁶⁷ 236 ²⁶⁸ | Gerward, ^e Gerward ^f Duclos, ^g Nakajima ^h |
| PBE1PBE | 5.375 | 239 | Present work |
| BMK | 5.359 | 230 | Present work |

^aReference ²⁴⁹

^bReference ²⁶⁹

^cReference ²⁵¹

^dReference ²⁷⁰

^eReference ²⁶⁸

^fReference ²⁷¹

^gReference ²⁶⁷

^hReference ⁷²

ⁱReference ²⁵³

Table 5-2: Lattice parameter and bulk modulus of Ce₂O₃ obtained with different methods. Val and Core indicate 4f-electron treated explicitly or with the Effective Core Potential respectively. Antiferromagnetic (AF) ,Ferromagnetic (FM)

| Method | a (Å) | c (Å) | B (GPa) | Reference |
|------------------|-------|-------|---------|---------------------------|
| LSDA (Core 4f) | 3.888 | | 165.8 | Skrodumova ^a |
| LSDA (Core 4f) | 3.871 | | 124 | Mikami ^b |
| LSDA (Val 4f) | 3.720 | | 208.6 | Skrodumova ^a |
| LSDA (Val 4f) AF | 3.761 | 5.864 | | Hay ^c |
| LSDA (Val 4f) FM | 3.776 | 5.859 | | Hay ^c |
| LSDA+U (Val 4f) | 3.84 | | 150.9 | Fabris ^d |
| PW91 (Core 4f) | 3.967 | | 145.3 | Skrodumova ^a |
| PW91 (Val 4f) | 3.805 | | 131.8 | Skrodumova ^a |
| PBE (Val 4f)AF | 3.878 | 6.094 | | Hay ^c |
| PBE (Val 4f) FM | 3.877 | 5.978 | | Hay ^c |
| GGA+U (Val 4f) | 3.94 | | 131.3 | Fabris ^d |
| TPSS (Val 4f) AF | 3.878 | 6.007 | | Hay ^c |
| TPSS (Val 4f) FM | 3.879 | 6.007 | | Hay ^c |
| HSE | 3.864 | | | Hay ^c |
| Experiment | 3.891 | 6.059 | | Barnighousen ^e |
| PBE1PBE | 3.845 | | 199.65 | This work |
| BMK | 3.880 | | 200.0 | This work |

^aReference ²⁵¹

^bReference ²⁷²

^cReference ²⁵³

^dReference ⁵⁶

^eReference ²¹⁸

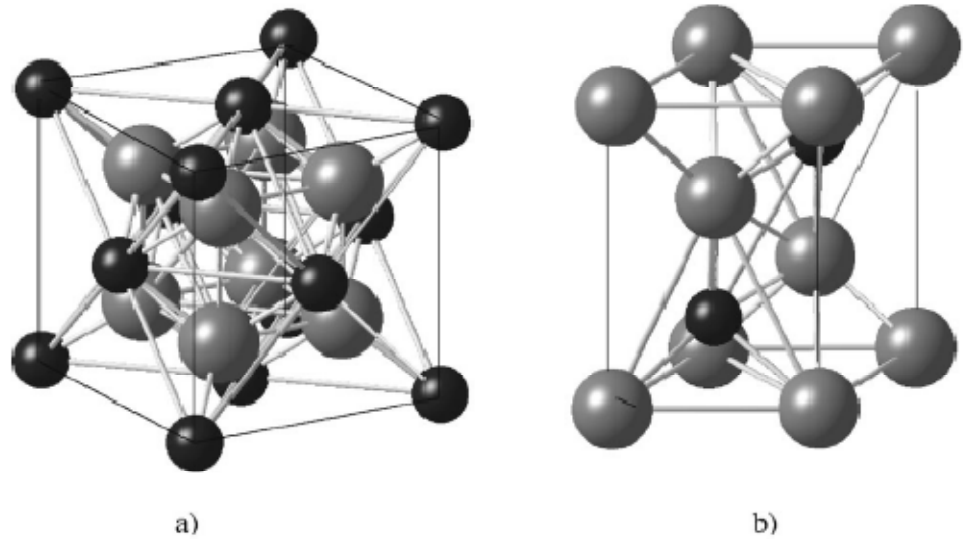


Figure 5-1: a) crystal structure of CeO_2 fluorite-type cubic structure; b) crystal structure of hexagonal Ce_2O_3 (A type). Ce and O atoms are shown here in black and grey circles respectively ²⁴⁵.

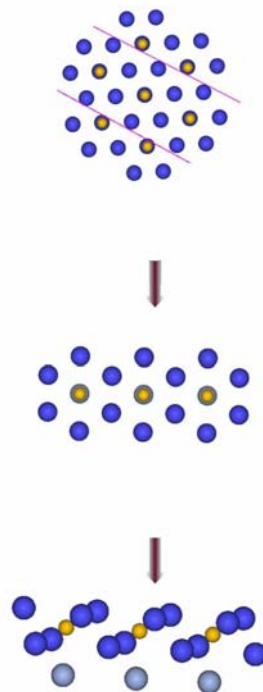


Figure 5-2: Side view of MX_2 sandwich bilayer

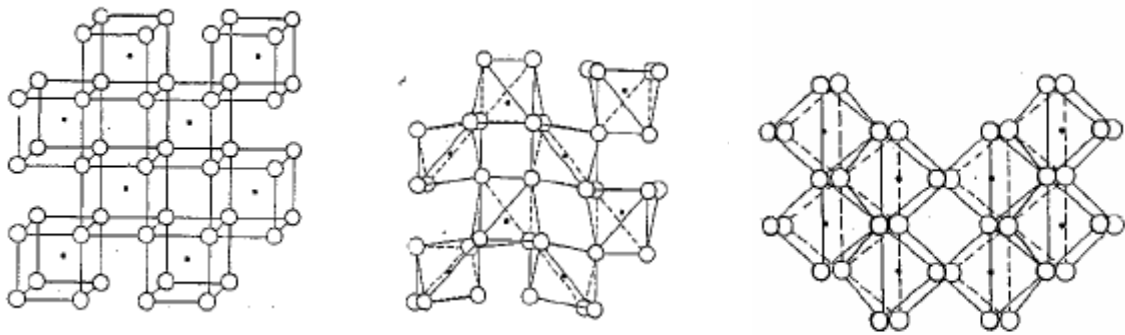


Figure 5-3: Schematic representation of a) Fluorite type CeO_2 ; b) C type body centered cubic; (c) A type hexagonal sesquioxide. Here solid dots represent metal ions and circles are oxygen ions²¹⁶.

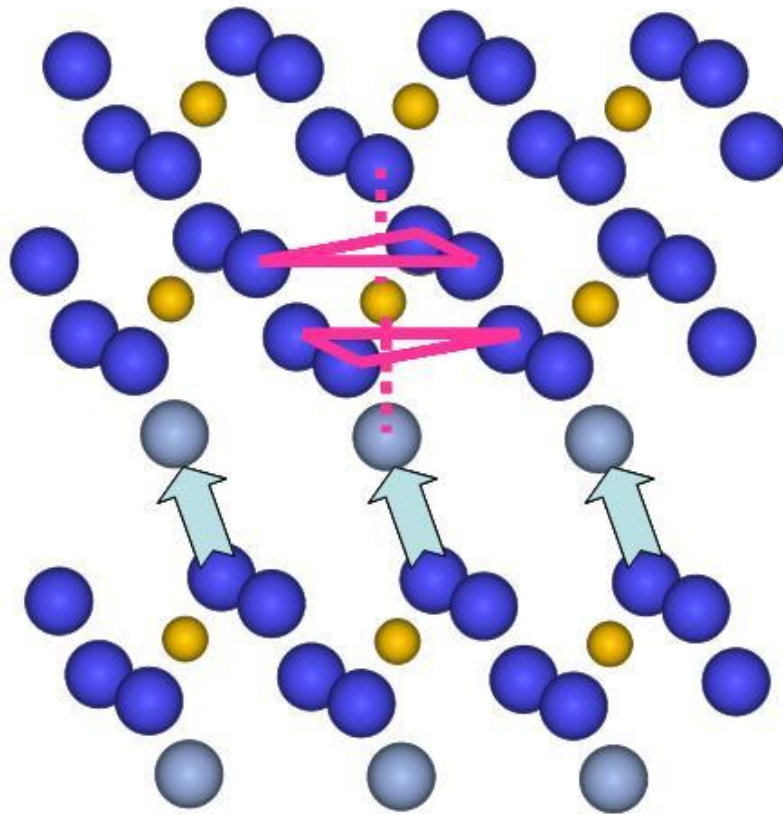


Figure 5-4: Formation of CaF_2 -type structure as ABC stacking of MX_2 sandwich bilayers.

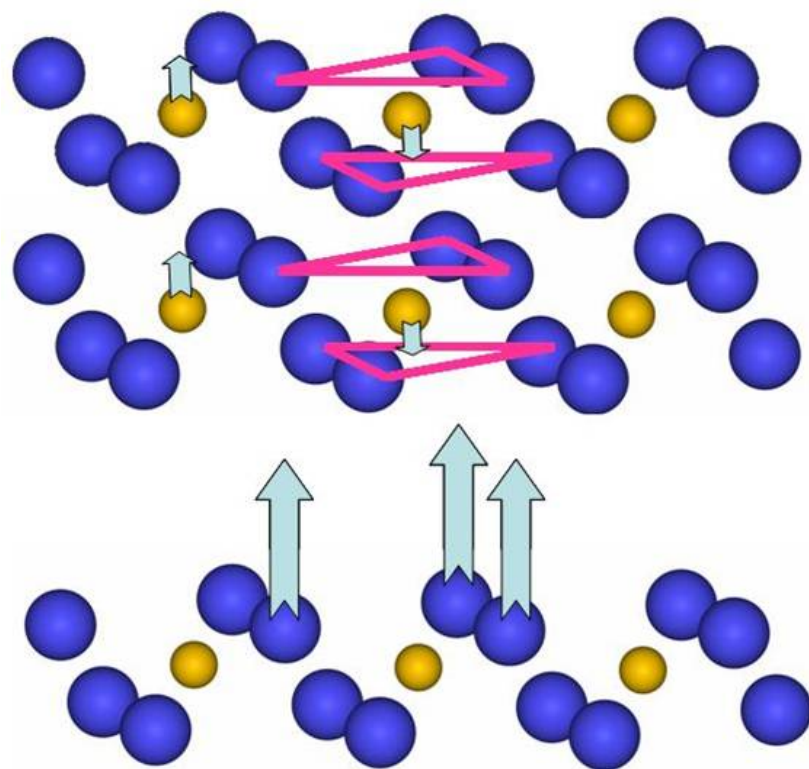


Figure 5-5: Formation of PbCl_2 type structure as stacking and distortion of MX_2 sandwich bilayers.

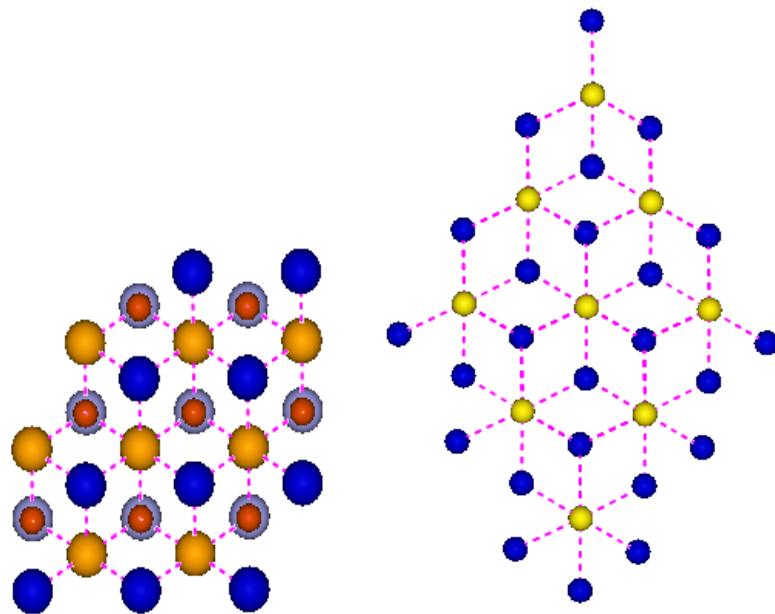


Figure 5-6: Layer structure for Type A

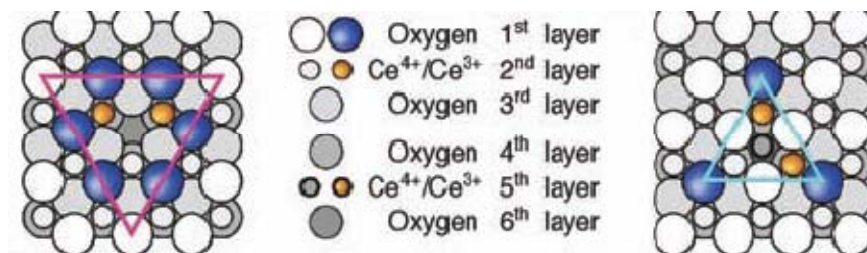


Figure 5-7: Surface oxygen vacancy by Esch *et. al*⁵⁶

5.6 Conclusions

We report the results of geometry optimization for bulk ceria CeO_2 and Ce_2O_3 at the hybrid DFT levels (BMK and PBE1PBE) with medium-size effective core potential and Gaussian basis set. The calculated values of lattice parameters and bulk moduli for both compounds are in excellent agreement with experiment. The results validate hybrid DFT as a promising method for future study the structure of oxygen vacancies and catalytic properties of ceria nanoparticles. The dependence of lattice parameter on the concentration of oxygen vacancies for ideal $\text{CeO}_2/\text{Ce}_2\text{O}_3$ solutions is predicted. Electro neutral and nonpolar pentalayers are identified as building blocks of type A sesquioxide structure, which explains the exceptional stability of subsurface vacancies in nanoceria.

BIBLIOGRAPHY

1. Gangopadhyay, S., Masunov, A. E. Kilina, S. "Hubbard U on the Ligand Atoms is Necessary for Quantitative Prediction of Heisenberg Exchange Constants " (*to be submitted to Physical Review Letters*)
2. Saha, A., Gangopadhyay, S., Nehrkorn, J., Milazzo, R. Waldmann, O., Hannu, M., Abboud, K. A., Wernsdorfer, W., Masunov, A., Christou, G.* "Synthesis and Characterization of a New High Spin, Half Integer Spin Mn₉ SMM by Electrochemistry, Magneto-chemistry, INS and DFT Studies" (*to be submitted to Journal of the American Chemical Society*)
3. Gangopadhyay, S., Kudin, K., Seal, S., Masunov, A., "Structure, Stability, and Composition of Ceria in Bulk and Nanoparticles from Density Functional Theory Simulations" (*to be submitted to Structural Chemistry*)
4. Gangopadhyay, S., Inerbaev, T., Masunov,* A. E., Mesit, J., Guha, R., Sleiti, A., Kapat, J. "Toward Rational Design of Ceramic Materials for Intermediate Temperature Solid Oxide Fuel Cell Cathodes: Understanding of Oxygen Vacancy Migration and Clustering in Barium/Strontium Ferrate/Cobaltate " *Solid State Ionics* 181 1067-1073 **2010**
5. Gangopadhyay, S., Masunov,* A. E., Poalelungi, E., Leuenberger,* M. Weak magnetic coupling in Mn₁₂ molecular magnet is predicted correctly at DFT+U theory level. *J. Chem. Phys* **132**, 244104 **2010**
6. Gangopadhyay, S., Masunov, A.E., Poalelungi, E., Leuenberger, M.N. "Prediction of exchange coupling constant for Mn₁₂ molecular magnet using DFT+U, *Proceedings of the 9th International Conference on Computational Science (ICCS), LNCS 5545, pp. 151, Springer: 2009.*
7. Gangopadhyay, S., Inerbaev, T., Masunov,* A.E., Orlovskaya, N.S. Structural characterization combined with the first principles simulations of barium/strontium ferrate/cobaltate as a promising material for SOFC. *ACS Applied Materials & Interfaces*.1 (7), 1512-1519, **2009**.
8. Gangopadhyay, S., Inerbaev, T., Masunov, *A. E., Mesit, J., Guha, R., Sleiti, A., Kapat, J. "Density Functional Theory and Multiscale Simulations Combined With Spectroscopic Study of Barium/Strontium Ferrate/Cobaltate (BSCF) as a Promising Material For Solid Oxide Fuel Cell (SOFC) " *pp 150-154, 2008, 17th Conference on Current Trends in Computational Chemistry (CCTCC).*
9. Gangopadhyay, S., Inerbaev, T., Masunov, *A. E., Mesit, J., Guha, R., Sleiti, A., Kapat, J. "Multiscale Simulations Combined With Experimental Study of Barium/Strontium Ferrate/Cobaltate (BSCF) as a Promising Material For Solid Oxide Fuel Cell (SOFC) " *MMM, pp.120-124, 2008, International Conference on MultiScale Material Modeling*

REFERENCES

- (1) Hohenberg, P.; Kohn, W. *Physical Review* **1964**, *136*, B864 - B871.
- (2) Kohn, W.; Sham, L. J. *Physical Review* **1965**, *140*, 1133-&.
- (3) Dirac, P. A. M. *Mathematical Proceedings of the Cambridge Philosophical Society* **1930**, *26*.
- (4) Slater, J. C. *Physical Review* **1951**, *81*, 385.
- (5) Hartree, D. R.; Hartree, W.; Swirles, B. *Phil. Trans. R. Soc. Lond. A* **1939**, *238*, 229-247.
- (6) Oktay, S.; Debbie Fu-tai, T. *The Journal of Chemical Physics* **1963**, *38*, 1740-1748.
- (7) Truhlar, D. G. *J. Comput. Chem.* **2007**, *28*, 73-86.
- (8) Anisimov, V. I.; Solovyev, I. V.; Korotin, M. A.; Czyzyk, M. T.; Sawatzky, G. A. *Physical Review B* **1993**, *48*, 16929-16934.
- (9) Anisimov, V. I.; Zaanen, J.; Andersen, O. K. *Phys. Rev. B: Condens. Matter* **1991**, *44*, 943-54.
- (10) Liechtenstein, A. I.; Anisimov, V. I.; Zaanen, J. *Physical Review B* **1995**, *52*, R5467.
- (11) Pickett, W. E.; Erwin, S. C.; Ethridge, E. C. *Physical Review B* **1998**, *58*, 1201-1209.
- (12) Hubbard, J. *Proceedings of the Royal Society of London. Series A. Mathematical and Physical Sciences* **1963**, *276*, 238-257.
- (13) Dudarev, S. L.; Botton, G. A.; Savrasov, S. Y.; Humphreys, C. J.; Sutton, A. P. *Physical Review B* **1998**, *57*, 1505-1509.
- (14) Hsu, H.; Umemoto, K.; Cococcioni, M.; Wentzcovitch, R. *Physical Review B* **2009**, *79*.
- (15) Svane, A.; Gunnarsson, O. *Physical Review Letters* **1990**, *65*, 1148-1151.
- (16) Szotek, Z.; Temmerman, W. M.; Winter, H. *Physical Review B* **1993**, *47*, 4029-4032.
- (17) Rohrbach, A.; Hafner, J.; Kresse, G. *Physical Review B* **2004**, *70*, 17.
- (18) Tran, F.; Blaha, P.; Schwarz, K.; Novak, P. *Physical Review B* **2006**, *74*.
- (19) Rignanese, G. M.; Pasquarello, A. *Journal of Physics-Condensed Matter* **2005**, *17*, S2089-S2098.
- (20) Burkert, T.; Nordstr; ouml; m, L.; Eriksson, O.; Heinonen, O. *Physical Review Letters* **2004**, *93*, 027203.
- (21) Raty, J. Y.; Gygi, F.; Galli, G. *Physical Review Letters* **2005**, *95*.
- (22) Hafner, J.; Wolverson, C.; Ceder, G. *MRS Bulletin* **2006**, *31*, 659-668.
- (23) Islam, M. S. 2002, p 75-85.
- (24) Shimojo, F.; Okazaki, H. *J. Phys. Soc. Jpn.* **1992**, *61*, 4106-18.
- (25) Meyer, M.; Nicoloso, N.; Jaenisch, V. *Phys. Rev. B: Condens. Matter* **1997**, *56*, 5961-5966.

- (26) Ramanarayanan, P.; Srinivasan, B.; Cho, K.; Clemens, B. M. *J. Appl. Phys.* **2004**, *96*, 7095-7107.
- (27) Eichler, A. *Physical Review B* **2001**, *64*.
- (28) Cherry, M.; Islam, M. S.; Catlow, C. R. A. *J. Solid State Chem.* **1995**, *118*, 125-32.
- (29) Khan, M. S.; Islam, M. S.; Bates, D. R. *J. Phys. Chem. B* **1998**, *102*, 3099-3104.
- (30) Lerch, M.; Boysen, H.; Hansen, T. *J. Phys. Chem. Solids* **2001**, *62*, 445-455.
- (31) Karki, B. B.; Khanduja, G. *Earth and Planetary Science Letters* **2007**, *260*, 201-211.
- (32) Ammann, M. W.; Brodholt, J. P.; Dobson, D. P. *Phys. Chem. Miner.* **2009**, *36*, 151-158.
- (33) Norge Cruz, H.; Javier Fernandez, S.; Luis Javier, A. *Journal of Physics: Condensed Matter* **2009**, 305502.
- (34) Sessoli, R.; Gatteschi, D.; Caneschi, A.; Novak, M. A. *Nature (London)* **1993**, *365*, 141-3.
- (35) Sessoli, R.; Tsai, H. L.; Schake, A. R.; Wang, S.; Vincent, J. B.; Folting, K.; Gatteschi, D.; Christou, G.; Hendrickson, D. N. *J. Am. Chem. Soc.* **1993**, *115*, 1804-16.
- (36) Lehmann, J.; Gaita-Arino, A.; Coronado, E.; Loss, D. *Nat Nano* **2007**, *2*, 312-317.
- (37) Leuenberger, M. N.; Loss, D. *Nature (London, U. K.)* **2001**, *410*, 789-793.
- (38) Ardavan, A.; Rival, O.; Morton, J. J. L.; Blundell, S. J.; Tyryshkin, A. M.; Timco, G. A.; Winpenny, R. E. P. *Phys Rev Lett* **2007**, *98*, 057201-4.
- (39) Postnikov, A. V.; Kortus, J.; Pederson, M. R. *Physica Status Solidi B-Basic Solid State Physics* **2006**, *243*, 2533-2572.
- (40) Dobisz, E. A.; Bandic, Z. Z.; Wu, T. W.; Albrecht, T. *Proceedings of the Ieee* **2008**, *96*, 1836-1846.
- (41) Meier, F.; Loss, D. *Phys. Rev. Lett.* **2001**, *86*, 5373-5376.
- (42) Affronte, M.; Troiani, F.; Ghirri, A.; Candini, A.; Evangelisti, M.; Corradini, V.; Carretta, S.; Santini, P.; Amoretti, G.; Tuna, F.; Timco, G.; Winpenny, R. E. P. *J. Phys. D: Appl. Phys.* **2007**, *40*, 2999-3004.
- (43) Friedman, J. r.; Sarachik, M. P.; Tejada, J.; Ziolo, R. *Phys. Rev. Lett.* **1996**, *76*, 3830-3833.
- (44) Gatteschi, D.; Caneschi, A.; Pardi, L.; Sessoli, R. *Science (Washington, D. C.)* **1994**, *265*, 1054-1058.
- (45) Canada-Vilalta, C.; O'Brien, T. A.; Pink, M.; Davidson, E. R.; Christou, G. *Inorg. Chem.* **2003**, *42*, 7819-7829.
- (46) Canada-Vilalta, C.; Pink, M.; Christou, G. *Chem. Commun. (Cambridge, U. K.)* **2003**, 1240-1241.
- (47) Waldmann, O.; Guidi, T.; Carretta, S.; Mondelli, C.; Dearden, A. L. *Phys Rev Lett* **2003**, *91*, 237202.
- (48) Van Slageren, J.; Sessoli, R.; Gatteschi, D.; Smith, A. A.; Helliwell, M.; Winpenny, R. E. P.; Cornia, A.; Barra, A.-L.; Jansen, A. G. M.; Rentschler, E.; Timco, G. A. *Chem.--Eur. J.* **2002**, *8*, 277-285.
- (49) Rumberger, E. M.; Zakharov, L. N.; Rheingold, A. L.; Hendrickson, D. N. *Inorg. Chem.* **2004**, *43*, 6531-6533.

- (50) Beedle, C. C.; Heroux, K. J.; Nakano, M.; DiPasquale, A. G.; Rheingold, A. L.; Hendrickson, D. N. *Polyhedron* **2007**, *26*, 2200-2206.
- (51) Scott, R. T. W.; Milios, C. J.; Vinslava, A.; Lifford, D.; Parsons, S.; Wernsdorfer, W.; Christou, G.; Brechin, E. K. *Dalton Trans.* **2006**, 3161-3163.
- (52) Murugesu, M.; Raftery, J.; Wernsdorfer, W.; Christou, G.; Brechin, E. K. *Inorg. Chem.* **2004**, *43*, 4203-4209.
- (53) Anastasios, J. T.; Alina, V.; Wolfgang, W.; Khalil, A. A.; George, C. *Angewandte Chemie International Edition* **2004**, *43*, 2117-2121.
- (54) Manoli, M.; Prescimone, A.; Mishra, A.; Parsons, S.; Christou, G.; Brechin, E. K. *Dalton Trans.* **2007**, 532-534.
- (55) Campbell, C. T.; Peden, C. H. F. *Science* **2005**, *309*, 713-714.
- (56) Esch, F.; Fabris, S.; Zhou, L.; Montini, T.; Africh, C.; Fornasiero, P.; Comelli, G.; Rosei, R. *Science* **2005**, *309*, 752-755.
- (57) Ozer, N. *Solar Energy Materials and Solar Cells* **2001**, *68*, 391-400.
- (58) Atanassov, G.; Thielsch, R.; Popov, D. *Thin Solid Films* **1993**, *223*, 288-292.
- (59) Krishna, M. G.; Hartridge, A.; Bhattacharya, A. K. *Materials Science and Engineering B-Solid State Materials for Advanced Technology* **1998**, *55*, 14-20.
- (60) Tye, L.; Elmasry, N. A.; Chikyow, T.; Mclarty, P.; Bedair, S. M. *Applied Physics Letters* **1994**, *65*, 3081-3083.
- (61) Steele, B. C. R. *Acad. Sci., Ser. IIc: Chim.* **1998**, *1*, 533-543.
- (62) Patsalas, P.; Logothetidis, S.; Metaxa, C. *Applied Physics Letters* **2002**, *81*, 466-468.
- (63) Norton, D. P.; Budai, J. D.; Chisholm, M. F. *Applied Physics Letters* **2000**, *76*, 1677-1679.
- (64) Huang, D. D.; Qin, F. G.; Yao, Z. Y.; Ren, Z. Z.; Lin, L. Y.; Gao, W. B.; Ren, Q. Y. *Applied Physics Letters* **1995**, *67*, 3724-3725.
- (65) Morshed, A. H.; Moussa, M. E.; Bedair, S. M.; Leonard, R.; Liu, S. X.; ElMasry, N. *Applied Physics Letters* **1997**, *70*, 1647-1649.
- (66) Frayret, C.; Villesuzanne, A.; Pouchard, M.; Matar, S. *International Journal of Quantum Chemistry* **2005**, *101*, 826-839.
- (67) Lybye, D.; Poulsen, F. W.; Mogensen, M. *Solid State Ionics* **2000**, *128*, 91-103.
- (68) Fernandez-Garcia, M.; Martinez-Arias, A.; Hanson, J. C.; Rodriguez, J. A. *Chemical Reviews* **2004**, *104*, 4063-4104.
- (69) Wuilloud, E.; Delley, B.; Schneider, W. D.; Baer, Y. *Physical Review Letters* **1984**, *53*, 202-205.
- (70) Adachi, G.; Imanaka, N. *Chemical Reviews* **1998**, *98*, 1479-1514.
- (71) Wang, Z. W.; Saxena, S. K.; Pishedda, V.; Liermann, H. P.; Zha, C. S. *Physical Review B* **2001**, *6401*.
- (72) Duclos, S. J.; Vohra, Y. K.; Ruoff, A. L.; Jayaraman, A.; Espinosa, G. P. *Physical Review B* **1988**, *38*, 7755-7758.
- (73) Kaspar, J.; Fornasiero, P.; Graziani, M. *Catalysis Today* **1999**, *50*, 285-298.
- (74) Wu, L.; Wiesmann, H. J.; Moodenbaugh, A. R.; Klie, R. F.; Zhu, Y.; Welch, D. O.; Suenaga, M. *Physical Review B (Condensed Matter and Materials Physics)* **2004**, *69*, 125415-9.

- (75) Matijevic, E.; Hsu, W. P. *Journal of Colloid and Interface Science* **1987**, *118*, 506-523.
- (76) Mani, T. V.; Varma, H. K.; Damodaran, A. D.; Warriar, K. G. K. *Ceramics International* **1993**, *19*, 125-128.
- (77) Chu, X.; Chung, W. I.; Schmidt, L. D. *Journal of the American Ceramic Society* **1993**, *76*, 2115-2118.
- (78) Varma, H. K.; Mukundan, P.; Warriar, K. G. K.; Damodaran, A. D. *Journal of Materials Science Letters* **1990**, *9*, 377-379.
- (79) Nabavi, M.; Spalla, O.; Cabane, B. *Journal of Colloid and Interface Science* **1993**, *160*, 459-471.
- (80) Baranchikov, A. E.; Polezhaeva, O. S.; Ivanov, V. K.; Tretyakov, Y. D. *Crystengcomm* **2010**, *12*, 3531-3533.
- (81) Tsunekawa, S.; Sivamohan, R.; Ohsuna, T.; Kasuya, A.; Takahashi, H.; Tohji, K. In *Rare Earths '98* 1999; Vol. 315-3, p 439-445.
- (82) Zhang, J.; Ju, X.; Wu, Z. Y.; Liu, T.; Hu, T. D.; Xie, Y. N.; Zhang, Z. L. *Chemistry of Materials* **2001**, *13*, 4192-4197.
- (83) Patil, S.; Kuiry, S. C.; Seal, S.; Vanfleet, R. *Journal of Nanoparticle Research* **2002**, *4*, 433-438.
- (84) Deshpande, S.; Patil, S.; Kuchibhatla, S.; Seal, S. *Applied Physics Letters* **2005**, *87*.
- (85) Tsunekawa, S.; Ito, S.; Kawazoe, Y. *Applied Physics Letters* **2004**, *85*, 3845-3847.
- (86) Kohn, W.; Becke, A. D.; Parr, R. G. *Journal of Physical Chemistry* **1996**, *100*, 12974-12980.
- (87) Geerlings, P.; De Proft, F.; Langenaeker, W. *Chemical Reviews* **2003**, *103*, 1793-1873.
- (88) Bredow, T.; Geudtner, G.; Jug, K. *Journal of Computational Chemistry* **2001**, *22*, 861-887.
- (89) Porezag, D.; Frauenheim, T.; Kohler, T.; Seifert, G.; Kaschner, R. *Physical Review B* **1995**, *51*, 12947-12957.
- (90) Pettersson, L. G. M.; Bauschlicher, C. W.; Langhoff, S. R.; Partridge, H. *Journal of Chemical Physics* **1987**, *87*, 481-492.
- (91) Becke, A. D. *Physical Review A* **1988**, *38*, 3098-3100.
- (92) Becke, A. D. *Journal of Chemical Physics* **1996**, *104*, 1040-1046.
- (93) Tao, J. M.; Perdew, J. P.; Staroverov, V. N.; Scuseria, G. E. *Physical Review Letters* **2003**, *91*, 4.
- (94) Furche, F.; Perdew, J. P. *Journal of Chemical Physics* **2006**, *124*, 27.
- (95) Solovyev, I. V.; Dederichs, P. H.; Anisimov, V. I. *Physical Review B* **1994**, *50*, 16861-16871.
- (96) Tablero, C. *Journal of Physics-Condensed Matter* **2008**, *20*.
- (97) Kulik, H. J.; Cococcioni, M.; Scherlis, D. A.; Marzari, N. *Physical Review Letters* **2006**, *97*, 4.
- (98) Inerbaev, T. M.; Seal, S.; Masunov, A. E. *Journal of Molecular Modeling* **2010**, *N/A*, 1-7.

- (99) Vincent, A.; Babu, S.; Heckert, E.; Dowding, J.; Hirst, S. M.; Inerbaev, T. M.; Self, W. T.; Reilly, C. M.; Masunov, A. E.; Rahman, T. S.; Seal, S. *ACS Nano* **2009**, *3*, 1203-1211.
- (100) Babu, S.; Thanneeru, R.; Inerbaev, T.; Day, R.; Masunov, A. E.; Schulte, A.; Seal, S. *Nanotechnology* **2009**, *20*.
- (101) Becke, A. D. *Journal of Chemical Physics* **1993**, *98*, 5648-5652.
- (102) Sousa, S. F.; Fernandes, P. A.; Ramos, M. J. *Journal of Physical Chemistry A* **2007**, *111*, 10439-10452.
- (103) Zhao, Y.; Truhlar, D. G. *Journal of Chemical Theory and Computation* **2008**, *4*, 1849-1868.
- (104) Jacquemin, D.; Wathelet, V.; Perpète, E. A.; Adamo, C. *Journal of Chemical Theory and Computation* **2009**, *5*, 2420-2435.
- (105) Adler, S. B. *Chemical Reviews* **2004**, *104*, 4791-4843.
- (106) Pena, M. A.; Fierro, J. L. G. *Chem. Rev.* **2001**, *101*, 1981-2018.
- (107) Möbius, H.-H. *Journal of Solid State Electrochemistry* **1997**, *1*, 2-16.
- (108) Shao, Z. P.; Haile, S. M. *Nature* **2004**, *431*, 170-173.
- (109) Kruidhof, H.; Bouwmeester, H. J. M.; Vondoorn, R. H. E.; Burggraaf, A. J. *Solid State Ionics* **1993**, *63-5*, 816-822.
- (110) Kharton, V. V.; Li, S. B.; Kovalevsky, A. V.; Naumovich, E. N. *Solid State Ionics* **1997**, *96*, 141-151.
- (111) Kharton, V. V.; Naumovich, E. N.; Nikolaev, A. V. *Journal of Membrane Science* **1996**, *111*, 149-157.
- (112) Teraoka, Y.; Nobunaga, T.; Okamoto, K.; Miura, N.; Yamazoe, N. *Solid State Ionics* **1991**, *48*, 207-212.
- (113) Teraoka, Y.; Zhang, H. M.; Furukawa, S.; Yamazoe, N. *Chemistry Letters* **1985**, 1743-1746.
- (114) Shao, Z. P.; Dong, H.; Xiong, G. X.; Gong, Y.; Yang, W. S. *Journal of Membrane Science* **2001**, *183*, 181-192.
- (115) Shao, Z.; Yang, W.; Cong, Y.; Dong, H.; Tong, J.; Xiong, G. *Journal of Membrane Science* **2000**, *172*, 177-188.
- (116) McIntosh, S.; Vente, J. F.; Haije, W. G.; Blank, D. H. A.; Bouwmeester, H. J. M. *Solid State Ionics* **2006**, *177*, 1737-1742.
- (117) Sammells, A. F.; Cook, R. L.; White, J. H.; Osborne, J. J.; Macduff, R. C.; Elsevier Science Bv: 1992, p 111-123.
- (118) Mogensen, M.; Lybye, D.; Bonanos, N.; Hendriksen, R.; Poulsen, F. W. *Solid State Ionics* **2004**, *174*, 279-286.
- (119) Ishihara, T.; Matsuda, H.; Takita, Y. *J. Am. Chem. Soc.* **1994**, *116*, 3801-3.
- (120) McIntosh, S.; Vente, J. F.; Haije, W. G.; Blank, D. H. A.; Bouwmeester, H. J. M. *Chemistry of Materials* **2006**, *18*, 2187-2193.
- (121) Vanderbilt, D. *Physical Review B* **1990**, *41*, 7892-7895.
- (122) Baroni, S.; Dal Corso, A.; de Gironcoli, S.; Giannozzi, P.; Cavazzoni, C.; Ballabio, G.; Scandolo, S.; Chiarotti, G.; Focher, P.; Pasquarello, A. Code available from <http://www.quantum-espresso.org>.

- (123) Marzari, N.; Vanderbilt, D.; De Vita, A.; Payne, M. C. *Physical Review Letters* **1999**, *82*, 3296-3299.
- (124) Gangopadhyay, S.; Inerbaev, T.; Masunov, A. E.; Altilio, D.; Orlovskaya, N. *Acs Applied Materials & Interfaces* **2009**, *1*, 1512-1519.
- (125) Graeme, H.; Hannes, J. *The Journal of Chemical Physics* **2000**, *113*, 9978-9985.
- (126) Birch, F. *Journal of Geophysical Research* **1978**, *83*, 1257-1268.
- (127) Svarcova, S.; Wiik, K.; Tolchard, J.; Bouwmeester, H. J. M.; Grande, T. *Solid State Ionics* **2008**, *178*, 1787-1791.
- (128) Yang, Z.; Harvey, A. S.; Infortuna, A.; Gauckler, L. J. *Journal of Applied Crystallography* **2009**, *42*, 153-160.
- (129) Glazer, A. M. *Acta Crystallographica Section B-Structural Science* **1972**, *B 28*, 3384-&.
- (130) Runka, T.; Berkowski, M.; Lapinski, A.; Drozdowski, M. *Journal of Physics and Chemistry of Solids* **2008**, *69*, 1646-1651.
- (131) Orlovskaya, N.; Steinmetz, D.; Yarmolenko, S.; Pai, D.; Sankar, J.; Goodenough, J. *Physical Review B* **2005**, *72*, 014122.
- (132) Kozlenko, D. P.; Golosova, N. O.; Jirak, Z.; Dubrovinsky, L. S.; Savenko, B. N.; Tucker, M. G.; Le Godec, Y.; Glazkov, V. P. *Physical Review B* **2007**, *75*, 10.
- (133) Potze, R. H.; Sawatzky, G. A.; Abbate, M. *Physical Review B* **1995**, *51*, 11501-11506.
- (134) Pruzan, P.; Gourdain, D.; Chervin, J. C.; Canny, B.; Couzinet, B.; Hanfland, M. *Solid State Communications* **2002**, *123*, 21-26.
- (135) Abbate, M.; Zampieri, G.; Okamoto, J.; Fujimori, A.; Kawasaki, S.; Takano, M. *Physical Review B* **2002**, *65*.
- (136) Bahadur, D.; Kollali, S.; Rao, C. N. R.; Patni, M. J.; Srivastava, C. M. *Journal of Physics and Chemistry of Solids* **1979**, *40*, 981-985.
- (137) Bezdicka, P.; Wattiaux, A.; Grenier, J. C.; Pouchard, M.; Hagenmuller, P. *Zeitschrift Fur Anorganische Und Allgemeine Chemie* **1993**, *619*, 7-12.
- (138) Watanabe *Journal of the Physical Society of Japan* **1957**, *12*, 515.
- (139) Lee, K. W.; Pickett, W. E. *Physical Review B (Condensed Matter and Materials Physics)* **2006**, *73*, 174428-8.
- (140) Shein, I. R.; Shein, K. I.; Kozhevnikov, V. L.; Ivanovskii, A. L. *Physics of the Solid State* **2005**, *47*, 2082-2088.
- (141) Lheureux, D.; Fischer, M.; Polian, A.; Itie, J. P.; Gauthier, M.; Syfosse, G. *Proceedings - IEEE Ultrasonics Symposium* **1999**, 533-536.
- (142) Takeda, T. *Journal of The Physical Society of Japan* **1972**, *33*, 967.
- (143) Collaboration: Authors and editors of the volumes, I. H. I. E. In *Ternary Compounds, Organic Semiconductors 2000*, p 1-6.
- (144) Abramov, Y. A.; Tsirelson, V. G.; Zavodnik, V. E.; Ivanov, S. A.; Brown, I. D. *Acta Crystallographica Section B-Structural Science* **1995**, *51*, 942-951.
- (145) Kilner, J. A. *Solid State Ionics* **1983**, *8*, 201-207.
- (146) Arom, G.; Brechin, E. *Struct. Bonding* **2006**, *122*, 1.
- (147) Noodleman, L. *Journal of Chemical Physics* **1981**, *74*, 5737-5743.
- (148) Noodleman, L.; Case, D. A. *Advances in Inorganic Chemistry* **1992**, *38*, 423-+.

- (149) Noodleman, L.; Davidson, E. R. *Chemical Physics* **1986**, *109*, 131-143.
- (150) Noodleman, L.; Han, W. G. *Journal of Biological Inorganic Chemistry* **2006**, *11*, 674-694.
- (151) Rudberg, E.; Salek, P.; Rinkevicius, Z.; Aagren, H. *J. Chem. Theory Comput.* **2006**, *2*, 981-989.
- (152) Neese, F. *J. Phys. Chem. Solids* **2004**, *65*, 781-785.
- (153) Soda, T.; Kitagawa, Y.; Onishi, T.; Takano, Y.; Shigeta, Y.; Nagao, H.; Yoshioka, Y.; Yamaguchi, K. *Chem. Phys. Lett.* **2000**, *319*, 223-230.
- (154) Ruiz, E.; Cano, J.; Alvarez, S.; Alemany, P. *J. Comput. Chem.* **1999**, *20*, 1391-1400.
- (155) Nishino, M.; Yamanaka, S.; Yoshioka, Y.; Yamaguchi, K. *J. Phys. Chem. A* **1997**, *101*, 705-712.
- (156) Goel, S.; Masunov, A. E. In *Lecture Notes in Computer Science* 2009; Vol. 5545 LNCS, p 141-150.
- (157) Goel, S.; Masunov, A. E. *Journal of Chemical Physics* **2008**, *129*.
- (158) Zhao, X. G.; Richardson, W. H.; Chen, J. L.; Li, J.; Noodleman, L.; Tsai, H. L.; Hendrickson, D. N. *Inorg Chem* **1997**, *36*, 1198-1217.
- (159) Cococcioni, M.; de Gironcoli, S. *Physical Review B* **2005**, *71*, 035105.
- (160) Cao, C.; Hill, S.; Cheng, H.-P. *Phys. Rev. Lett.* **2008**, *100*, 167206/1-167206/4.
- (161) McMahan, A. K.; Martin, R. M.; Satpathy, S. *Phys. Rev. B: Condens. Matter* **1988**, *38*, 6650-66.
- (162) Yoo, J.; Brechin, E. K.; Yamaguchi, A.; Nakano, M.; Huffman, J. C.; Maniero, A. L.; Brunel, L. C.; Awaga, K.; Ishimoto, H.; Christou, G.; Hendrickson, D. N. *Inorg Chem* **2000**, *39*, 3615-23.
- (163) Dismukes, G. C. *Chem. Rev. (Washington, D. C.)* **1996**, *96*, 2909-2926.
- (164) Whittaker, M. M.; Barynin, V. V.; Antonyuk, S. V.; Whittaker, J. W. *Biochemistry* **1999**, *38*, 9126-9136.
- (165) Willing, A.; Follmann, H.; Auling, G. *Eur. J. Biochem.* **1988**, *175*, 167-73.
- (166) Willing, A.; Follmann, H.; Auling, G. *Eur. J. Biochem.* **1988**, *170*, 603-11.
- (167) Willing, A.; Follmann, H.; Auling, G. *Eur J Biochem* **1988**, *175*, 167-73.
- (168) Yachandra, V. K.; Sauer, K.; Klein, M. P. *Chem. Rev. (Washington, D. C.)* **1996**, *96*, 2927-2950.
- (169) Manchanda, R.; Brudvig, G. W.; Crabtree, R. H. *Coord. Chem. Rev.* **1995**, *144*, 1-38.
- (170) Pecoraro, V. L.; Baldwin, M. J.; Gelasco, A. *Chem. Rev. (Washington, D. C.)* **1994**, *94*, 807-26.
- (171) Foguet-Albiol, D.; O'Brien, T. A.; Wernsdorfer, W.; Moulton, B.; Zaworotko, M. J.; Abboud, K. A.; Christou, G. *Angew. Chem., Int. Ed.* **2005**, *44*, 897-901.
- (172) Pal, S.; Olmstead, M. M.; Armstrong, W. H. *Inorg. Chem.* **1995**, *34*, 4708-15.
- (173) Schafer, K. O.; Bittl, R.; Zweggart, W.; Lendzian, F.; Haselhorst, G.; Weyhermuller, T.; Wieghardt, K.; Lubitz, W. *Journal of the American Chemical Society* **1998**, *120*, 13104-13120.
- (174) Bossek, U.; Wieghardt, K.; Nuber, B.; Weiss, J. *Inorg. Chim. Acta* **1989**, *165*, 123-9.

- (175) Romero, I.; Dubois, L.; Collomb, M. N.; Deronzier, A.; Latour, J. M.; Pecaut, J. *Inorg Chem* **2002**, *41*, 1795-1806.
- (176) Wieghardt, K.; Bossek, U.; Zsolnai, L.; Huttner, G.; Blondin, G.; Girerd, J. J.; Babonneau, F. *J. Chem. Soc., Chem. Commun.* **1987**, 651-3.
- (177) Gultneh, Y.; Tesema, Y. T.; Yisgedu, T. B.; Butcher, R. J.; Wang, G. B.; Yee, G. T. *Inorganic Chemistry* **2006**, *45*, 3023-3033.
- (178) Andrei, V. P.; Jens, K.; Mark, R. P. *Physica Status Solidi (b)* **2006**, *243*, 2533-2572.
- (179) Kortus, J.; Pederson, M. R.; Hellberg, C. S.; Khanna, S. N. *European Physical Journal D* **2001**, *16*, 177-180.
- (180) Michalak, L.; Canali, C. M.; Pederson, M. R.; Paulsson, M.; Benza, V. G. *Physical Review Letters* **2010**, *104*.
- (181) Park, K.; Baruah, T.; Pederson, M. R. *Abstracts of Papers of the American Chemical Society* **2004**, *228*, 436-PHYS.
- (182) Ribas-Arino, J.; Baruah, T.; Pederson, M. R. *Journal of the American Chemical Society* **2006**, *128*, 9497-9505.
- (183) Zhang, J. R.; He, L. H.; Cao, H. B.; Wang, F. W.; Zhang, P. L. *Journal of Chemical Physics* **2008**, *128*.
- (184) Postnikov, A. V.; Bihimayer, G.; Blugel, S. *Computational Materials Science* **2006**, *36*, 91-95.
- (185) Noodleman, L.; Case, D. A. *Adv. Inorg. Chem.* **1992**, *38*, 423-70.
- (186) Noodleman, L.; Lovell, T.; Han, W. G.; Li, J.; Himo, F. *Chem. Rev.* **2004**, *104*, 459-508.
- (187) Shoji, M.; Hamamoto, T.; Koizumi, K.; Isobe, H.; Kitagawa, Y.; Takano, Y.; Yamanaka, S.; Okumura, M.; Yamaguchi, K. *Polyhedron* **2005**, *24*, 2701-2707.
- (188) Shoji, M.; Isobe, H.; Saito, T.; Yabushita, H.; Koizumi, K.; Kitagawa, Y.; Yamanaka, S.; Kawakami, T.; Okumura, M.; Hagiwara, M.; Yamaguchi, K. *International Journal of Quantum Chemistry* **2008**, *108*, 631-650.
- (189) Shoji, M.; Koizumi, K.; Kitagawa, Y.; Yamanaka, S.; Kawakami, T.; Okumura, M.; Yamaguchi, K. *International Journal of Quantum Chemistry* **2005**, *105*, 628.
- (190) Shoji, M.; Koizumi, K.; Kitagawa, Y.; Yamanaka, S.; Okumura, M.; Yamaguchi, K. *International Journal of Quantum Chemistry* **2007**, *107*, 609-627.
- (191) Shoji, M.; Koizumi, K.; Kitagawa, Y.; Yamanaka, S.; Okumura, M.; Yamaguchi, K. *International Journal of Quantum Chemistry* **2007**, *107*, 609-627.
- (192) Shoji, M.; Koizumi, K.; Taniguchi, T.; Kitagawa, Y.; Yamanaka, S.; Okumura, M.; Yamaguchi, K. *International Journal of Quantum Chemistry* **2007**, *107*, 116-133.
- (193) Shoji, M.; Nishiyama, Y.; Maruno, Y.; Koizumi, K.; Kitagawa, Y.; Yamanaka, S.; Kawakami, T.; Okumura, M.; Yamaguchi, K. *International Journal of Quantum Chemistry* **2004**, *100*, 887-906.
- (194) Boukhvalov, D. W.; Al-Saqer, M.; Kurmaev, E. Z.; Moewes, A.; Galakhov, V. R.; Finkelstein, L. D.; Chiuzbaian, S.; Neumann, M.; Dobrovitski, V. V.; Katsnelson, M. I.; Lichtenstein, A. I.; Harmon, B. N.; Endo, K.; North, J. M.; Dalal, N. S. *Physical Review B* **2007**, *75*.

- (195) Boukhvalov, D. W.; Dobrovitski, V. V.; Katsnelson, M. I.; Lichtenstein, A. I.; Harmon, B. N.; Kogerler, P. *Journal of Applied Physics* **2003**, *93*, 7080-7082.
- (196) Boukhvalov, D. W.; Dobrovitski, V. V.; Katsnelson, M. I.; Lichtenstein, A. I.; Harmon, B. N.; Kogerler, P. *Physical Review B* **2004**, *70*.
- (197) Boukhvalov, D. W.; Kurmaev, E. Z.; Moewes, A.; Zatsopin, D. A.; Cherkashenko, V. M.; Nemnonov, S. N.; Finkelstein, L. D.; Yarmoshenko, Y. M.; Neumann, M.; Dobrovitski, V. V.; Katsnelson, M. I.; Lichtenstein, A. I.; Harmon, B. N.; Kogerler, P. *Physical Review B* **2003**, *67*.
- (198) Pablo, R.; Christoph, L.; Ibério De, P. R. M.; Francesc, I. *Journal of Computational Chemistry* **2009**, *30*, 2316-2326.
- (199) Nair, N. N.; Ribas-Arino, J.; Staemmler, V.; Marx, D. *Journal of Chemical Theory and Computation* **2010**, *6*, 569-575.
- (200) Nair, N. N.; Schreiner, E.; Pollet, R.; Staemmler, V.; Marx, D. *Journal of Chemical Theory and Computation* **2008**, *4*, 1174-1188.
- (201) Schreiner, E.; Nair, N. N.; Pollet, R.; Staemmler, V.; Marx, D. *Proceedings of the National Academy of Sciences of the United States of America* **2007**, *104*, 20725-20730.
- (202) Kulik, H. J.; Cococcioni, M.; Scherlis, D. A.; Marzari, N. *Physical Review Letters* **2006**, *97*, 103001.
- (203) Cao, C.; Hill, S.; Cheng, H.-P. *Phys Rev Lett* **2008**, *100*, 167206.
- (204) Gangopadhyay, S.; Masunov, A. E.; Poalelungi, E.; Leuenberger, M. N. *The Journal of Chemical Physics* **2010**, *132*, 244104-7.
- (205) Foguet-Albiol, D.; O'Brien, T. A.; Wernsdorfer, W.; Moulton, B.; Zaworotko, M. J.; Abboud, K. A.; Christou, G. *Angewandte Chemie-International Edition* **2005**, *44*, 897-901.
- (206) Ramsey, C. M.; Del Barco, E.; Hill, S.; Shah, S. J.; Beedle, C. C.; Hendrickson, D. N. *Nature Physics* **2008**, *4*, 277-281.
- (207) Cano, J.; Costa, R.; Alvarez, S.; Ruiz, E. *Journal of Chemical Theory and Computation* **2007**, *3*, 782-788.
- (208) Rumberger, E. M.; Shah, S. J.; Beedle, C. C.; Zakharov, L. N.; Rheingold, A. L.; Hendrickson, D. N. *Inorg. Chem.* **2005**, *44*, 2742-2752.
- (209) Waldmann, O. *Private Communication*.
- (210) Meier, F.; Loss, D. *Physical Review B* **2001**, *64*.
- (211) Hay, P. J.; Thibeault, J. C.; Hoffmann, R. *Journal of the American Chemical Society* **1975**, *97*, 4884-4899.
- (212) Clark, A. E.; Davidson, E. R. *The Journal of Chemical Physics* **2001**, *115*, 7382-7392.
- (213) Deluga, G. A.; Salge, J. R.; Schmidt, L. D.; Verykios, X. E. *Science* **2004**, *303*, 993-997.
- (214) Otsuka, K.; Ushiyama, T.; Yamanaka, I. *Chemistry Letters* **1993**, 1517-1520.
- (215) Park, S. D.; Vohs, J. M.; Gorte, R. J. *Nature* **2000**, *404*, 265-267.
- (216) Gschneidner, K. A.; Eyring, L. *Handbook on the physics and chemistry of rare earths*; North-Holland Pub. Co. ; sole distributors for the U.S.A. and Canada Elsevier North Holland: Amsterdam ; New York New York, 1979.

- (217) Kourouklis, G. A.; Jayaraman, A.; Espinosa, G. P. *Physical Review B* **1988**, *37*, 4250-4253.
- (218) Barnighausen, H.; Schiller, G. *Journal of the Less-Common Metals* **1985**, *110*, 385-390.
- (219) Trovarelli, A. *Catalysis by ceria and related materials*; Imperial College Press: London, 2002.
- (220) Yoshimura, S. a. *Journal of Ceramic association of Japan* **1968**, *76*.
- (221) Masunov, A. E. *Koordinatsionnaya Khimiya* **1993**, *19*, 261-268.
- (222) Fujimori, A. *Physical Review Letters* **1984**, *53*, 2518-2518.
- (223) Inerbaev, T. M.; Seal, S.; Masunov, A. E. *Journal of Molecular Modeling*, *16*, 1617-1623.
- (224) Vincent, A.; Inerbaev, T. M.; Babu, S.; Karakoti, A. S.; Self, W. T.; Masunov, A. E.; Seal, S. *Langmuir*, *26*, 7188-7198.
- (225) Vincent, A.; Babu, S.; Heckert, E.; Dowding, J.; Hirst, S. M.; Inerbaev, T. M.; Self, W. T.; Reilly, C. M.; Masunov, A. E.; Rahman, T. S.; Seal, S. *Acs Nano* **2009**, *3*, 1203-1211.
- (226) Loschen, C.; Bromley, S. T.; Neyman, K. M.; Illas, F. *Journal of Physical Chemistry C* **2007**, *111*, 10142-10145.
- (227) Loschen, C.; Carrasco, J.; Neyman, K. M.; Illas, F. *Physical Review B* **2007**, *75*.
- (228) Loschen, C.; Migani, A.; Bromley, S. T.; Illas, F.; Neyman, K. M. *Physical Chemistry Chemical Physics* **2008**, *10*, 5730-5738.
- (229) Yang, Z. X.; Wang, Q. G.; Wei, S. Y.; Ma, D. W.; Sun, Q. A. *Journal of Physical Chemistry C* **2010**, *114*, 14891-14899.
- (230) Chen, C.; Chen, H. L.; Weng, M. H.; Ju, S. P.; Chang, J. G.; Chang, C. S. *Chinese Journal of Catalysis* **2008**, *29*, 1117-1121.
- (231) Choi, Y. M.; Abernathy, H.; Chen, H. T.; Lin, M. C.; Liu, M. L. *Chemphyschem* **2006**, *7*, 1957-1963.
- (232) Skorodumova, N. V.; Simak, S. I.; Lundqvist, B. I.; Abrikosov, I. A.; Johansson, B. *Physical Review Letters* **2002**, *89*, 4.
- (233) Suzuki, C.; Tochio, T. *Chemical Physics* **2007**, *340*, 203-210.
- (234) Shapovalov, V.; Metiu, H. *Journal of Catalysis* **2007**, *245*, 205-214.
- (235) Song, Y. Q.; Zhang, H. W.; Yang, Q. H.; Liu, Y. L.; Li, Y. X.; Shah, L. R.; Zhu, H.; Xiao, J. Q. *Journal of Physics-Condensed Matter* **2009**, *21*, 5.
- (236) Zhan-Sheng, L.; Gai-Xia, L.; Zong-Xian, Y. *Acta Physica Sinica* **2007**, *56*, 5382-5388.
- (237) Wei, Y. W.; Yang, Z. X. *Acta Physica Sinica* **2008**, *57*, 7139-7144.
- (238) Baudin, M.; Wojcik, M.; Hermansson, K. *Surface Science* **2000**, *468*, 51-61.
- (239) Castleton, C. W. M.; Kullgren, J.; Hermansson, K. *Journal of Chemical Physics* **2007**, *127*.
- (240) Herschend, B.; Baudin, M.; Hermansson, K. *Surface Science* **2005**, *599*, 173-186.
- (241) Herschend, B.; Baudin, M.; Hermansson, K. *Chemical Physics* **2006**, *328*, 345-353.
- (242) Muller, C.; Freysoldt, C.; Baudin, M.; Hermansson, K. *Chemical Physics* **2005**, *318*, 180-190.

- (243) Muller, C.; Herschend, B.; Hermansson, K.; Paulus, B. *Journal of Chemical Physics* **2008**, *128*.
- (244) Muller, C.; Paulus, B.; Hermansson, K. *Surface Science* **2009**, *603*, 2619-2623.
- (245) Skorodumova, N. V.; Baudin, M.; Hermansson, K. *Physical Review B* **2004**, *69*.
- (246) Yang, Z. X.; Woo, T. K.; Hermansson, K. *Surface Science* **2006**, *600*, 4953-4960.
- (247) Koelling, D. D.; Boring, A. M.; Wood, J. H. *Solid State Communications* **1983**, *47*, 227-232.
- (248) Marabelli, F.; Wachter, P. *Physical Review B* **1987**, *36*, 1238-1243.
- (249) Hill, S. E.; Catlow, C. R. A. *Journal of Physics and Chemistry of Solids* **1993**, *54*, 411-419.
- (250) Gennard, S.; Cora, F.; Catlow, C. R. A. *Journal of Physical Chemistry B* **1999**, *103*, 10158-10170.
- (251) Skorodumova, N. V.; Ahuja, R.; Simak, S. I.; Abrikosov, I. A.; Johansson, B.; Lundqvist, B. I. *Physical Review B* **2001**, *6411*.
- (252) Nolan, M.; Grigoleit, S.; Sayle, D. C.; Parker, S. C.; Watson, G. W. *Surface Science* **2005**, *576*, 217-229.
- (253) Hay, P. J.; Martin, R. L.; Uddin, J.; Scuseria, G. E. *Journal of Chemical Physics* **2006**, *125*, -.
- (254) Boese, A. D.; Martin, J. M. L. *Journal of Chemical Physics* **2004**, *121*, 3405-3416.
- (255) Becke, A. D. *Journal of Chemical Physics* **1993**, *98*, 1372-1377.
- (256) Kudin, K. N.; Scuseria, G. E. *Physical Review B* **2000**, *61*, 16440-16453.
- (257) Frisch, M. J.; C.02 ed.; Gaussian Inc Wallingford CT, 2004.
- (258) Kudin, K. N.; Scuseria, G. E.; Martin, R. L. *Physical Review Letters* **2002**, *89*, -.
- (259) Prodan, I. D.; Scuseria, G. E.; Sordo, J. A.; Kudin, K. N.; Martin, R. L. *Journal of Chemical Physics* **2005**, *123*.
- (260) Cundari, T. R.; Stevens, W. J.; Sommerer, S. O. *Chemical Physics* **1993**, *178*, 235-243.
- (261) Stevens, W. J.; Basch, H.; Krauss, M. *Journal of Chemical Physics* **1984**, *81*, 6026-6033.
- (262) Stevens, W. J.; Krauss, M.; Basch, H.; Jasien, P. G. *Canadian Journal of Chemistry-Revue Canadienne De Chimie* **1992**, *70*, 612-630.
- (263) Birch, F. *Physical Review* **1947**, *71*, 809.
- (264) Birch, F. *Journal of Applied Physics* **1938**, *9*, 279-288.
- (265) Ziambaras, E.; Schroder, E. *Physical Review B (Condensed Matter and Materials Physics)* **2003**, *68*, 064112-7.
- (266) Schaftenaar, G.; Noordik, J. H. *J. Comput.-Aided Mol. Design* **2000**, *14*, 123-134.
- (267) Nakajima, A.; Yoshihara, A.; Ishigame, M. *Physical Review B* **1994**, *50*, 13297-13307.
- (268) Gerward, L.; Olsen, J. S. *Powder Diffraction* **1993**, *8*, 127-129.
- (269) Jiang, Y.; Adams, J. B.; van Schilfgaarde, M. *Journal of Chemical Physics* **2005**, *123*, -.
- (270) Yang, Z. X.; Woo, T. K.; Baudin, M.; Hermansson, K. *Journal of Chemical Physics* **2004**, *120*, 7741-7749.

(271) Gerward, L.; Staun Olsen, J.; Petit, L.; Vaitheeswaran, G.; Kanchana, V.; Svane, A. *Journal of Alloys and Compounds* **2005**, *400*, 56-61.

(272) Mikami, M.; Nakamura, S. *Journal of Alloys and Compounds* **2006**, *408*, 687-692.